LUND UNIVERSITY

Crystal Structures in GaAs Nanowires: Growth and Characterization

Jacobsson, Daniel

2015

[Link to publication](#)

Crystal Structures in GaAs Nanowires

Growth and Characterization

Daniel Jacobsson

LUND
UNIVERSITY

DOCTORAL DISSERTATION
by due permission of the Faculty of Engineering, Lund University, Sweden.

To be defended Friday May 29, 2015 at 09.30

in the Rydberg Lecture Hall at the Department of Physics, Lund.

Faculty opponent

Prof. Lincoln J. Lauhon

Northwestern University

Author(s) Daniel Jacobsson	Sponsoring organization

Title and subtitle	
Crystal Structures in GaAs Nanowires - Growth and Characterization	

Abstract

With their nanometer size cross-section and high aspect ratio, semiconducting nanowires have properties that make them promising as building blocks in future electronic and optoelectronic devices. Because of their small size, their optical and electrical properties can differ from their bulk counterparts, and their geometry allows for material combinations not accessible in thin films. Moreover, nanowires are possible to grow with crystal structures which are different from their stable phase in the bulk. The focus of this thesis is on tuning the crystal structure of Au-seeded GaAs nanowires between the zincblende (ZB) structure, which is stable in the bulk, and the metastable wurtzite (WZ) structure.

Metal-organic vapor phase epitaxy (MOVPE) has been used to demonstrate a single temperature approach to achieving high quality WZ-ZB heterostructures. To increase the complexity of the nanowires, heterostructures with controlled ZB inclusions in WZ nanowires were also grown. Detailed post-growth analysis of the seed particle composition suggested a Ga-rich growth environment for WZ, whereas it is possible to grow defect-free ZB in As-rich conditions. To achieve a sharp interface between ZB grown with As-rich conditions and a following WZ segment, the local growth environment has to be returned to Ga-rich before growth is continued. To gain further control of the growth of polytypic GaAs nanowires, the possibility of using HCl as an additive during growth has been explored.

Using *in situ* transmission electron microscopy, real time growth studies of GaAs WZ-ZB nanowires revealed distinct differences between the two polytypes for the growth dynamics at the seed particle-nanowire interface. By increasing or decreasing the Ga content within the Au-Ga alloy seed particle, crystal structure tuning was achieved, with the wetting angle of the seed particle as the trigger changing between growth of ZB and WZ.

The different atomic arrangements in WZ and ZB GaAs mean that the two polytypes have different electronic, optical and surface properties, even though they have the same composition. This thesis work has determined the nature of the faceting of WZ-ZB heterostructures and the lattice parameters of WZ and the higher order polytype 4H, as well as the band gap of WZ and its and band alignment with ZB.

Key words		
Nanowires, III-V semiconductor material, metal-organic vapor phase epitaxy, *in situ* TEM		

Classification system and/or index terms (if any)		

Supplementary bibliographical information	Language English

ISSN and key title	ISBN

Recipient's notes	Number of pages	Price
	Security classification	

Crystal Structures in GaAs Nanowires

Growth and Characterization

Daniel Jacobsson

Doctoral Thesis
2015

Division of Solid State Physics
Department of Physics
Lund University

Abstract

With their nanometer size cross-section and high aspect ratio, semiconducting nanowires have properties that make them promising as building blocks in future electronic and optoelectronic devices. Because of their small size, their optical and electrical properties can differ from their bulk counterparts, and their geometry allows for material combinations not accessible in thin films. Moreover, nanowires are possible to grow with crystal structures which are different from their stable phase in the bulk. The focus of this thesis is on tuning the crystal structure of Au-seeded GaAs nanowires between the zincblende (ZB) structure, which is stable in the bulk, and the metastable wurtzite (WZ) structure.

Metal-organic vapor phase epitaxy (MOVPE) has been used to demonstrate a single temperature approach to achieving high quality WZ-ZB heterostructures. To increase the complexity of the nanowires, heterostructures with controlled ZB inclusions in WZ nanowires were also grown. Detailed post-growth analysis of the seed particle composition suggested a Ga-rich growth environment for WZ, whereas it is possible to grow defect-free ZB in As-rich conditions. To achieve a sharp interface between ZB grown with As-rich conditions and a following WZ segment, the local growth environment has to be returned to Ga-rich before growth is continued. To gain further control of the growth of polytypic GaAs nanowires, the possibility of using HCl as an additive during growth has been explored.

Using *in situ* transmission electron microscopy, real time growth studies of GaAs WZ-ZB nanowires revealed distinct differences between the two polytypes for the growth dynamics at the seed particle-nanowire interface. By increasing or decreasing the Ga content within the Au-Ga alloy seed particle, crystal structure tuning was achieved, with the wetting angle of the seed particle as the trigger changing between growth of ZB and WZ.

The different atomic arrangements in WZ and ZB GaAs mean that the two polytypes have different electronic, optical and surface properties, even though they have the same composition. This thesis work has determined the nature of the faceting in WZ-ZB heterostructures and the lattice parameters of WZ and the higher order polytype 4H, as well as the band gap of WZ and its and band alignment with ZB.

Populärvetenskaplig sammanfattning

En liknelse som ibland används till nanoteknik är atomslöjd. Liknelsen är i vissa avseende ganska bra, vilket kan ses om vi tar en titt i tillverkningen av modern elektronik. Tar vi den mest grundläggande komponenten i en dators processor, en transistor, är den ledande kanalen inte mer än cirka 8 nanometer som bredast – vilket inte är mer än cirka 14 atomer – och lite drygt 40 nanometer hög, lite drygt 70 atomer[1]. Detaljerna i dessa transistorer är skapade ur en kiselskiva med diameter på 300mm, eller 300000000 nanometer. För att skapa den ledande kanalen, tas lite material bort runt omkring, i likhet med att snida detaljer i slöjd, fast på atomär nivå. Slöjden måste utföras väldigt exakt, då komponenter med storlek på nanometernivå är beroende på ett fåtal atomers typ och position i komponenten.

Den kiselskiva som används i tillverkning av transistorer är gjord av en enda stor kristall, där atomerna sitter i ett regelbundet mönster. För att skapa komponenter på skivan, tas en del av kristallen bort för att skapa rätt geometri, eller förändras genom tillskott av atomer av annan typ (dopning). Detta görs för att kristallen ska få önskade egenskaper innan kontakter och andra perifera detaljer läggs till. Istället för att snida ut detaljer ur en större kristall, ett uppifrån-och-ner-tillvägagångssätt ("top-down"), kan man tillverka komponenten på kristallen genom att växa den atomlager för atomlager och ändra atomlagernas sammansättning eller position för att få de önskade egenskaperna i kristallen. Med ett sådant nedifrån-och-upp tillvägagångssätt ("bottom-up"), kan väldigt specifika strukturer skapas. En del av forskningen på Fasta Tillståndets Fysik i Lund handlar om hur man kan växa tunna och långa trådar av kristallint halvledarmaterial, så kallade nanotrådar, med ett "bottom-up"-tillvägagångssätt. Den här avhandlingen fokuserar på hur man genom att ändra parametrar för växten kan styra hur atomerna i nanotråden är positionerade i förhållande till varandra; det vill säga nanotrådens kristallstruktur. Genom att använda avancerad elektronmikroskopi tittar vi, bokstavligen, närmare på hur tråden beter sig under tiden den växer, atomlager för atomlager.

Varför är egentligen nanotrådar så intressanta? En nanotråds dimensioner är vanligtvis några mikrometer lång och några tiotals nanometer i diameter, vilket kan jämföras med ett hårstrås tjocklek på några tiotals (upp till 100) mikrometer. En nanometer är en tusendels mikrometer, och en nanotråd är cirka tusen gånger tunnare än ett hårstrå.

---

[1] Baserat på Intels Broadwell arkitektur med 14nm-teknik.

Görs nanotråden av halvledarmaterial, vilket elektroniska komponenter vanligtvis görs av, påverkas elektronerna av de små dimensionerna. Detta gör att kvantmekaniska fenomen går att studera i nanotrådarna. De små dimensionerna hos nanotrådar gör också att de interagerar med ljus på intressanta sätt. Nanotrådar i täta matriser kan fungera som små antenner och absorbera ljus bättre än en homogen film med samma materialvolym, vilket gör att mindre material behövs i till exempel solceller.

Tack vare att nanotrådarna är så tunna, kan material med större valfrihet kombineras i en nanotråd jämfört med tunna filmer. Kristaller bestående av olika material kan ha olika långt mellan atomerna i kristallen, olika gitterkonstant, och om man försöker kombinera material med olika gitterkonstant måste kristallerna antingen tryckas ihop eller dras isär vid gränsytan mellan de olika materialen. I nanotrådar är detta lättare att göra än i kristaller med makroskopiska dimensioner. Ytterligare en intressant egenskap hos nanotrådar är deras förmåga att bilda kristallstrukturer som normalt inte finns i deras makroskopiska motsvarighet.

Nanotrådarna i den här avhandlingen är växta med hjälp av små guldpartiklar, mellan 30 och 80 nanometer i diameter. Tillverkningen av nanotrådarna går till som sådan, att först sprids guldpartiklar ut på ett substrat, vanligtvis en kristall med en orientering av kristallstrukturen så att nanotrådarna kommer att växa rakt upp från ytan. Substratet med guldpartiklarna hettas upp i en reaktorkammare, i vilken även gaser med de atomer som önskas i nanotrådarna introduceras, bundna till större molekyler. De större molekylerna bryts sönder av värmen i reaktorkammern, antingen i gasfasen eller i kontakt med substratets yta, och atomerna som ska bygga upp nanotråden frigörs. Dessa atomer, växtmaterialet, legerar med guldpartiklarna, och efterhand stiger koncentration av växtmaterialet vilket gör guldpartikeln övermättad. Vid tillräckligt hög övermättnad sker utfällning av material från guldpartikeln, vilket preferentiellt sker vid gränsytan mellan partikel och substrat. På så sätt växes det första lagret av atomer i den blivande nanotråden. Nästa gång utfällning sker, bildas återigen ett lager i gränsytan mellan partikel och kristallen under, nu den nya nanotråden. På sätt växer nanotråden lager för lager, och för varje nytt lager lyfts guldpartikeln upp från substratet, se illustration i figur 1.

Nu kommer vi till kärnan av arbetet i den här avhandlingen. För varje nytt lager som bildas i nanotråden, finns det två alternativ för hur atomerna arrangeras. Vilket alternativ som det blir, bestämmer vilken kristallstruktur som nanotråden lokalt kommer att få. Genom att styra flödena av de inkommande gaserna, kan man även styra vilken position som nästa lager får, och därmed kristallstrukturen. Det material som studierna här är gjorda på är galliumarsenid (GaAs), men principen är den samma för många andra III-V halvledare. Vi visar här att genom att ha överflöd av den ena eller andra typen av atom (Ga eller As) när man växer GaAs kan man, inom ett viss temperaturintervall, skifta mellan en struktur som kallas zinkblände (ZB) och en som kallas wurtzit (WZ). Eftersom de olika kristallstrukturerna har olika optiska och elektroniska egenskaper, kan man genom att kontrollerat ändra kristallstruktur, ändra egenskaperna hos nanotråden.
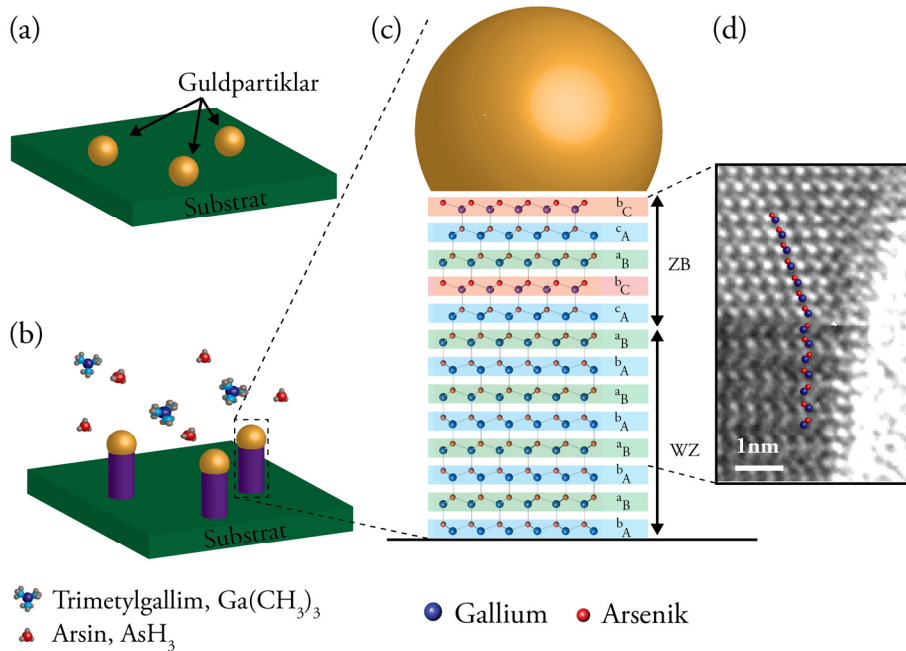
Figur 1. (a) För att initiera växt av III-V nanotrådar, kan små partiklar av guld användas. Dessa sprids ut över ett substrat, vanligen en kristall av III-V material eller kisel. Substratet hettas upp, och de atomer som nanotråden ska bestå av, i det här fallet gallium och arsenik, förs in i reaktorkammaren i gasfas bundna i större molekyler, till exempel trimetylgallium och arsin (b). Beroende på hur varje atomplan är orienterat i nanotrådens växtriktning, fås olika kristallstrukturer, vilket kan ses i (c). Genom att använda ett transmissionselektronmikroskop för att avbilda nanotråden kan man få en bild över hur kristallstrukturen ser ut, och skillnader mellan wurtzite och zinkblände, vilket kan ses i bilden i (d).

För att kunna se nanotrådens kristallstruktur kan man avbilda nanotråden med hjälp av högupplöst transmissionselektronmikroskopi. I ett sådant mikroskop används elektroner istället för ljus för att belysa provet. Som namnet antyder, använder man sig av elektroner som passerar *genom* provet. För att elektroner ska kunna göra det krävs väldigt tunna prov, normalt under 100 nanometer (vilket gör nanotrådar tillräckligt tunna för transmissionselektronmikroskopi) och hög energi på elektronerna. De elektroner som passerar genom provet kan användas för att skapa en projektion av de atomära kolumnerna i provet, och om kristallen är roterad rätt, kan man urskilja vilken kristallstruktur som provet har. I figur 1d visas bild på en nanotråd med wurtzit struktur, som ger ett sicksack-liknande mönster i ordningen av atomerna, med ett segment zinkblände, som ger ett mer diagonalt mönster. Skalstrecket i figur 1d motsvarar 1nm, vilket i tryck blir ca 1cm och förstoringen av nanotråden är alltså cirka 10 miljoner gånger.

I de allra flesta studier av hur nanotrådar växer, tillverkas nanotråden för att först efter avslutad växt analyseras och utifrån dessa resultat dra slutsatser om själva växtprocessen.

Tänk om man istället hade kunnat se vad som faktiskt händer vid gränsytan mellan partikel och nanotråd, *när* det faktiskt händer? Med speciella transmissionselektronmikroskop, som blivit modifierade så att gaser kan släppas in i mikroskopet, kan man studera hur kristaller växer. Hos våra samarbetspartners på IBM i New York finns det i dagsläget det enda sådana mikroskopet för studier på GaAs nanotrådar. En del av den här avhandlingen handlar om de första resultaten på just GaAs nanotrådar växta i det mikroskopet, där vi medvetet ändrar kristallstruktur för att se hur gränsytan mellan partikel och nanotråd förändras då de olika strukturerna växer. Ju mer detaljer vi känner till om hur nanotrådar växer, desto bättre kan vi designa hur de ska se ut. Kan vi designa nanotrådarnas egenskaper, kan de mycket väl bli komponenter i morgondagens elektroniska kretsar, till exempel i transistorer, solceller och lysdioder. Våra resultat visar att det går att styra nanotrådarnas kristallstruktur ner till enstaka atomlager, och vi kan nog kalla växt av sådana nanotrådar för just atomslöjd.

List of papers

This thesis is based on the following papers. In the text, they will be referred to with upper case Roman numerals.

I.   **High crystal quality wurtzite-zinc blende heterostructures in metal-organic vapor phase epitaxy-grown GaAs nanowires**
S. Lehmann, <u>D. Jacobsson</u>, K. Deppert and K. A. Dick.
Nano Research, 2012, **5**, 470-476.

I developed the growth procedure together with S.L., performed some of the TEM analysis, and took part in discussions within the project.

In this study we managed for the first time to prepare very high crystal quality wurtzite-zincblende heterostructures by only changing the V/III ratio. Using TEM, we determined the terminating facets of the two polytypes formed.

II. **Zincblende-to-wurtzite interface improvement by group III loading in Au-seeded GaAs nanowires**
<u>D. Jacobsson</u>, S. Lehmann and K. A. Dick.
Physica Status Solidi-Rapid Research Letters, 2013, **7**, 855-859.

I initiated and led the project, performed all the experimental work (growth, TEM and SEM), and wrote the paper.

In Paper I, we noted an increase in stacking defects in wurtzite sections following a zincblende inclusion, which could be an indication that the switch in the effective V/III ratio at the growth interface was not fast enough. Based on more detailed analysis of Au-Ga seed particles after growth, we propose a procedure to tune growth conditions to reduce stacking defects in wurtzite after zincblende inclusions.

III. **Crystal structure tuning in GaAs nanowires using HCl**
<u>D. Jacobsson</u>, S. Lehmann and K. A. Dick.
Nanoscale, 2014, **6**, 8257-8264.

I initiated and led the project, performed all the experimental work (growth, TEM and SEM), and wrote the paper.

In papers I and II, we noted anisotropic radial growth occurred preferentially at zincblende facets. HCl has been used for controlling the morphology of other III-V nanowires, and we explored the possibility of using HCl as an additive to gain further control of our wurtzite-zincblende heterostructures. Interestingly, HCl primarily reacts with Ga precursors, and can be used to increase the effective V/III ratio at the growth front, resulting in zincblende becoming the preferred crystal structure.

IV. **In Situ TEM studies of polytypic GaAs nanowire growth**
<u>D. Jacobsson</u>, F. Panciera, M. C. Reuter, S. Lehmann, J. Tersoff, K. A. Dick and F. M. Ross.
In Manuscript

I did the experimental work together with F.P., I performed all the analysis, took part in discussions, and wrote the paper.

In this study, we used *in situ* TEM to study the growth kinetics of wurtzite and zincblende. A dramatic difference at the growth interface was found for the two polytypes: for wurtzite, the growth proceeded as a ledge moving slowly across the nanowire-seed particle interface, whereas zincblende grew with an oscillating tri-junction. We also found that it was the droplet geometry that triggered the switch between wurtzite and zincblende, independently of precursor flows.

V. **Observation of type-II recombination in single wurtzite/zinc-blende GaAs heterojunction nanowires**
N. Vainorius, <u>D. Jacobsson</u>, S. Lehmann, A. Gustafsson, K. A. Dick, L. Samuelson and M. E. Pistol.
Physical Review B, 2014, **89**,165423.

I took part in initiating the project, grew some of the structures, performed parts of the TEM, and took part in discussions within the project and the writing of the paper.

The different atomic arrangement in wurtzite compared to zincblende results in differences in their bandstructures. Using power-dependent photoluminescence, we show that wurtzite and zincblende GaAs has a type-II band alignment, and extract the band offsets. To verify that is was indeed the polytype interface that was measured, we correlated photoluminescence with TEM, as well as using cathodoluminescence.

VI. **Phase transformation in radially merged wurtzite GaAs nanowires**
D. Jacobsson*, F. Yang*, K. Hillerich, F. Lenrick, S. Lehmann, D. Kriegner, J. Stangl, L. R. Wallenberg, K. A. Dick and J. Johansson.
Submitted to Crystal Growth & Design

I supervised the growth and grew some of the structures, I performed part of the TEM, I performed the XRD measurements and analysis together with D.K., took part in project discussions, and co-authored the paper together with F.Y..

By growing radially on pure wurtzite GaAs nanowires, we explored the possibility of forming continuous wurtzite films using the nanowires as growth templates. However, as different wurtzite nanowires do not necessarily have the same stacking order, defects at the interfaces between the nanowires introduce stacking defects in the wurtzite. Using XRD, we follow a phase transformation from pure wurtzite to a mixed structure of wurtzite and zincblende as the proportion of radially merged nanowires increases. We also determine accurate lattice parameters for wurtzite and 4H GaAs.

The following papers are not included in the thesis because they overlap in content or have a scope beyond that of the thesis. In the text, they are referred to using lower case Roman numerals.

vii.   **Particle-assisted GaxIn1-xP nanowire growth for designed bandgap structures**
D. Jacobsson, J. M. Persson, D. Kriegner, T. Etzelstorfer, J. Wallentin, J. B. Wagner, J. Stangl, L. Samuelson, K. Deppert and M. T. Borgström.
Nanotechnology, 2012, **23**, 245601.

viii. **Single GaInP nanowire p-i-n junctions near the direct to indirect bandgap crossover point**
J. Wallentin, L. B. Poncela, A. M. Jansson, K. Mergenthaler, M. Ek, D. Jacobsson, L. R. Wallenberg, K. Deppert, L. Samuelson, D. Hessman and M. T. Borgström.
Applied Physics Letter, 2012, **100**, 251103.

ix.   **Direct Imaging of Atomic Scale Structure and Electronic Properties of GaAs Wurtzite and Zinc Blende Nanowire Surfaces**
M. Hjort, S. Lehmann, J. Knutsson, R. Timm, D. Jacobsson, E. Lundgren, K. A. Dick and A. Mikkelsen.
Nano Letters, 2013, **13**, 4492-4498.

x.   **Structural investigation of GaInP nanowires using X-ray diffraction**
D. Kriegner, J. M. Persson, T. Etzelstorfer, D. Jacobsson, J. Wallentin, J. B. Wagner, K. Deppert, M. T. Borgström and J. Stangl.
Thin Solid Films, 2013, **543**, 100-105.

xi.   **Magnetic Polarons and Large Negative Magnetoresistance in GaAs Nanowires Implanted with Mn Ions**
S. Kumar, W. Paschoal, A. Johannes, D. Jacobsson, C. Borschel, A. Pertsova, C. H. Wang, M. K. Wu, C. M. Canali, C. Ronning, L. Samuelson and H. Pettersson.
Nano Letters, 2013, **13**, 5079-5084.

xii.   **A General Approach for Sharp Crystal Phase Switching in InAs, GaAs, InP, and GaP Nanowires. Using Only Group V Flow**
S. Lehmann, J. Wallentin, D. Jacobsson, K. Deppert and K. A. Dick.
Nano Letters, 2013, **13**, 4099-4105.

xiii. **Control of composition and morphology in InGaAs nanowires grown by metalorganic vapor phase epitaxy**
J. Wu, B. M. Borg, D. Jacobsson, K. A. Dick and L. E. Wernersson.
Journal of Crystal Growth, 2013, **383**, 158-165.

xiv. **GaAs/AlGaAs heterostructure nanowires studied by cathodoluminescence**
J. Bolinsson, M. Ek, J. Tragardh, K. Mergenthaler, <u>D. Jacobsson</u>, M. E. Pistol, L. Samuelson and A. Gustafsson.
Nano Research, 2014, **7**, 473-490.

xv. **Enhanced sputtering and incorporation of Mn in implanted GaAs and ZnO nanowires**
A. Johannes, S. Noack, W. Paschoal, S. Kumar, <u>D. Jacobsson</u>, H. Pettersson, L. Samuelson, K. A. Dick, G. Martinez-Criado, M. Burghammer and C. Ronning.
Journal of Physics D-Applied Physics, 2014, **47**, 394003.

xvi. **FIB Plan and Side View Cross-Sectional TEM Sample Preparation of Nanostructures**
F. Lenrick, M. Ek, <u>D. Jacobsson</u>, M. T. Borgström and L. R. Wallenberg.
Microscopy and Microanalysis, 2014, **20**, 133-140.

xvii. **Magnetoresistance in Mn ion-implanted GaAs:Zn nanowires**
W. Paschoal, S. Kumar, <u>D. Jacobsson</u>, A. Johannes, V. Jain, C. M. Canali, A. Pertsova, C. Ronning, K. A. Dick, L. Samuelson and H. Pettersson.
Applied Physics Letters, 2014, **104**, 153112.

xviii. **Confinement in thickness-controlled GaAs polytype nanodots**
N. Vainorius, S. Lehmann, <u>D. Jacobsson</u>, L. Samuelson, K.A. Dick and M.-E. Pistol.
Nano Letters, 2015, **15**, 2652-2656

Acknowledgements

During my time as a PhD student, I've spent more time in the lab, at conferences or at various meetings with other PhD students, researchers, supervisors and friends than in my office, trying to write manuscripts or analyze data. Trying to thank each one of you separately would probably end up with an acknowledgement section half the length of this thesis. I would nevertheless specifically thank some of you who have been extra important.

First of all, my four supervisors: Kimberly, Sebastian, Jonas, and Knut.

Kimberly, I'm constantly impressed that you always find time for your PhD students, even with your busy schedule. Thank you for all your invaluable comments on my work, and the inspiring dicsussions, and for sharing your immense knowledge of nanowires. It is not without reasons that Suneel Kodambaka calls you "the Queen of III-V Nanowires". And of course, thank you for all the cakes and the summer barbeques!

Sebastian, I've lost count of how many tries we made to get those polytypic nanowires grown for the PL projects with the old Aixtron. But, finally we got the structures! Your hands-on support with growth and TEM in the labs has been very much appreciated, and I hope we are able to continue working together. And not only working, we definitely should try to find more time for fishing – maybe in Öresund, if we trust the boats…

Jonas, having an office next to yours has been a great asset. Anytime I've had questions regarding thermodynamics, I knew I had a living book of references just a few meters away. You are the one who first taught me the basics of epitaxy, and the one who finally convinced me to apply for this PhD position.

Knut, for always being there in the background, pushing me back on track when I need it the most. You are the one among my supervisors who has been there as support for the longest time – from the time when I started on the Engineering Nanoscience program as a first year undergrad. You have always been a source of inspiration regarding nanoscience.

All past and present members in the research group led by Kimberly: Sebastian, Sepideh, Robert, Rong, Luna, Markus, Erik, Dario, Elias, Reza and Louise. I've learnt a lot during our weekly meetings, thanks for sharing all your results and current

problems, for all the feedback on presentations, and for all the cakes! Maybe it's my turn soon to bring a cheesecake?

Sepideh, can't think of a better office mate. Always positive, always well organized – just compare our office desks – and always with time to chat on any topic: music, coffee, work, travels… And thanks for telling me not to work too much – it has helped me to finish things.

I started to grow nanowires already as an undergraduate, and have met plenty of other growers during my years in the lab. My first nanowires were grown at Sol Voltaics and GLO, with the guidance of Stefan, Martin M, Jonas O, Bi and Rafal – at that time MOVPE was mainly a magic box, but you gave me the first insights on the processes within it. Thanks Magnus B and Jesper W for supervising the first growth projects that were my own. And thank you, Kenichi, Magnus H, Peter, Jessica, Karla, Mattias, Phil, Sofia FS, Johannes, Jun, Cezar, Elvedin, Fangfang, Gaute, Alexander and David G, you have all helped in making the magic box more understandable.

Saying no to new projects has always been hard for me, maybe to my supervisors discontentment, but it gave me the opportunity to collaborate with many different people and groups. Mats-Erik and Neimantas, finally we are getting the measurements done we have been talking about for several years. With this pace, it won't take long before you're done with your PhD, Neimantas, but I'm not sure if Mats-Erik will let you go – there is still so much to do, and you are needed to keep the equipment running! Waldomiro, Håkan, Andreas and Carsten, the Mn-implanted nanowires have been really interesting, thanks for letting me be a part of the projects, and not just the nanowire supplier. Rong, thanks for realizing the Sn-seeded nanowire projects. If you wouldn't have started your PhD, I think I would still have had the initial experiments designed – but only on paper and never carried out. Fangfang, your Master thesis grew to become a large project, with many supervisors, but it turned out pretty well (even if the structure we aimed at was not possible to achieve). Filip, you soon have to teach me your secrets on the FIB. Johannes and Jun – helping you with TEM analysis and discussing nanowire growth has been a joy. Some of your structures have been perfect for pushing my knowledge of the TEM and how to combine different methods to get a more complete picture of heterostructures.

I have never been alone as a PhD student at Solid State Physics, plenty of other students - some already graduated, some very new - have shared the excitement at new results, stress over no results, and agonies of endless undergrad project reports to correct – Kalle, Laura, Ali, Mahtab, Yang, I-Ju, Vilgaile, Bahram, Masoomeh, Atefeh, Bao, Stefan H, Henrik, Olof, Laiq, Vishal, Reza J, Maryam, Zhen, Frida, Linus, Malin, Cassie, Kushagr, Regina, Artis, Trung, Damiano, Florinda, Chunlin, Ricardo, Sofia, Xulu. Without you, this time would have been rather dull. With you, there has always been someone to chat with over a coffee, someone who feels the same stress or excitement of being a PhD student.

Håkan, George and the rest of LNL staff – thanks for keeping everything running inside and outside of the lab. Without you, no research would have been possible.

Reine, Crispin, Gunnel, Martin and Filip – thanks for keeping the TEM running and teaching me how to use it. Martin, the switch is still on "more magic" and the images are crisp and clear. Thanks for the advice before you left for Denmark.

Dominik and Julian in Linz, Austria, thanks for teaching me the secrets of XRD, and thank you Peter for keeping the XRD running in Lund. Dominik, you were a great host and I highly appreciated the day on the slopes for some skiing and snowboarding.

Frances, a big thank you for the time spent at IBM T.J. Watson in NY – it was amazing to see the first nanowires grow in the *in situ* TEM. The beautiful movies we obtained and your and Brians' hospitality made the stay in US one of the best periods of my PhD. I hope I'm able to visit you soon again, but then I'll bring the whole family!

Federico, thank you for all the time spent with me at the *in situ* TEM, and thank you for all trips to the Gunks. I'll keep on climbing, and when you visit Sweden, we have to try out the problems in Kjugekull. And of course, have a barbeque!

The innebandy team(s) – David L, Kristian, Kilian, Anil, Andreas, Johan, Kalle, Nicklas, Neimantas, Adam, … the list is now too long to put all your names down. Too bad I haven't been able to play for a long time, I should take better care of my toes.

Jason and Bengt for organizing the "lunch climbing". Should we organize climbing sessions outdoors as well, at the new boulder in Stadsparken? Or maybe another trip to Kjugekull, Johan and Anna? Or do you prefer top ropes, Line, now as you know how to belay?

The skiers who joined the trips to Val Thorens and Argentiére: Gustav, Mercy, Mingtang, Erik, Jesper M, Odd, Jarle, Robert, Matilda, Johan and Anna. The toboggan in Val Thorens was a blast, I dare you all on a rerun whenever we get back there! And Odd, thanks for riding snowboard, for once I was not the only one. Next time we go offpist, let's hope for snow and not just pine-needles the last parts down to the valley.

Erik, Martin H and Filip – thanks for sharing. I hope we will continue this tradition even as you move to Stanford, Martin.

All friends not working with nanoscience – thanks for all the brunches, lunches, dinners, game evenings, parties, wedding parties and barbeques - well needed breaks from my studies! And thanks for the questions on what I'm *actually* doing at work, they put some perspective to what I've done during the past 4.5 years.

Since 2008, I've had two families, both encouraging me, pushing me and in so many ways helping me through my PhD. Thank you, Paul and Carina for welcoming me with open arms, even if I came with your daughter on a motorbike the first time I visited you. I still have a lot to learn from you Paul, regarding cooking and renovations,

Contents

1 Introduction

"What I want to talk about is the problem of manipulating and controlling things on a small scale"

Richard Feynman
December 29, 1959

The quotation above has been taken from an after-dinner speech at a conference, but it fits well with the essential themes of this thesis. The quote comes from a speech by Richard Feynman, *"There is plenty of room at the bottom"*, a speech which more than 50 years ago challenged researchers to explore the world of miniaturization to a much greater extent than had been done at the time. Instead of just carving out smaller and smaller building blocks, a top-down approach, would it instead be possible to use a bottom-up approach and arrange atoms the way we want? *"What could we do with layered structures with just the right layers? What would the properties of materials be if we would really arrange the atoms the way we want?"* Using modern techniques to grow semiconductor crystals epitaxially, we are not yet able to achieve single atom control, but we are close to control of single atomic layers. The focus of this thesis is on the growth and characterization of GaAs nanowires, where the position of each atomic bilayer (one layer of Ga and one layer of As) determines the properties of the semiconductor crystal. By changing parameters during fabrication of the nanowires, the layered structure is altered, with control down to single bilayers. Together with characterization of such structures, we are today able to answer some of the questions posed by Feynman, questions still relevant today within nanotechnology research.

Why is there such an interest in making things smaller? On a macroscopic scale, the smaller something becomes, the less material is required to fabricate it, which has economic benefits. For integrated circuits, such scaling has doubled the transistor density on a chip every two years for the last forty years, with a decreased cost per transistor. However, simply scaling indefinitely will have its challenges as components will behave differently at smaller sizes. As an object becomes smaller, its surface-to-volume ratio increases, and surface properties eventually come to dominate over the bulk. For catalyst particles and sensors, where the reactions of interest are happening at the surface, the increased surface-to-volume ratio increases efficiency and sensitivity. For electronics scaled down to nanometer dimensions, quantum mechanics become important, as the electrons may, for example, tunnel through thin electron barriers,

limiting the performance of scaled-down transistors. To fully take advantage of, and study, physical phenomena related to nanoscale objects, we need to be able to fabricate them accurately.

One way of fabricating nanostructures is to use a bottom-up approach, where molecules and particles self-assemble into specific structures. For semiconductor crystals, such structures may be grown using epitaxy techniques, where the crystal is grown atom by atom. By using a seed particle to promote growth in a single direction, thin nanowires with diameter of a few nanometers [1] and virtually any length can be grown. With their high aspect ratio, nanowires can be treated as one-dimensional objects. If their diameter is made small enough, they will confine electrons in the radial direction, and zero-dimensional and one-dimensional electron transport along the nanowire axis can occur [2-4]. The small diameter of the nanowire also allows for radial strain relaxation in axial growth of lattice-mismatched materials. The ability to accommodate for strain makes the nanowire geometry ideal for heterostructures which are impossible to grow without defects in planar structures, such as InAs/InSb with its 7% lattice mismatch [5]. With a larger freedom in terms of material combinations, it is possible to design structures with regard to optimum performance, not material compatibility. Several nanowire-based component devices have been demonstrated, both in opto-electronics [6-9] and electronics [10-12].

For nanowires, it is not only the possibility to combine materials in ways not possible in bulk systems that enables new types of heterostuctures, but also the possibility to grow the nanowires with a crystal structure different from the stable bulk phase. Even though most III-V materials have a zincblende (ZB) crystal structure in the bulk, nanowires of the same material very often show a mixture of the ZB and wurtzite (WZ) structures [13]. An uncontrolled polytypism would be detrimental to device properties [14], but being able to control the crystal structure could open up new possibilities for designing device properties – without even changing material [15, 16]. A change in crystal structure is also predicted to change the band structure of the material; in many cases the WZ structure is predicted to have a larger band gap [17]. Controlling the crystal phases makes it possible to create, for example, a ZB quantum dot in a WZ nanowire [16, 18].

The work in this thesis has been to further develop the growth of WZ and ZB GaAs nanowires and heterostructures, using metal-organic vapor phase epitaxy (MOVPE). Growth of both WZ and pure ZB GaAs was achieved shortly before this thesis work began, which gave a good starting point [19]. At the same time, extensive work was carried out to map the growth parameters for structure tuning in InAs nanowires [20]. Other groups have also been working on crystal phase tuning, and even though we were early in being able to grow high quality WZ GaAs nanowires on (Paper I), we were, for example, not the first to measure the band gap of pure WZ GaAs nanowires [21]. Even before this, several groups had tried to measure the band gap of WZ GaAs, but with a large spread in results due to insufficient control over the crystal structure [22-24]. However, because we were able to achieve high quality WZ-ZB heterostructures, we

were the first to perform photoluminescence studies on such heterostructures, shedding light on the band alignment of WZ and ZB (Paper V). Understanding the processes controlling the formation of WZ and ZB would allow for controlled growth of different phases with specific lengths within the same nanowire, which would enable detailed studies of crystal phase quantum dots (Paper xviii). Using either additives to the growth (such as HCl, Paper III), or using more complex precursor gas switching (Paper II), further studies on creating WZ-ZB and ZB-WZ heterostructures were carried out, revealing more details of the formation of the different crystal structures.

For the MOVPE-grown nanowires in this thesis, the ZB is grown with a high flow of the Group V precursor (the As precursor) compared to the Group III precursor (the Ga precursor): a high V/III ratio. WZ is grown with a low V/III ratio. However, there are published reports of Au-assisted GaAs nanowire growth using a different growth technique, molecular beam epitaxy (MBE), which produces ZB at a low V/III ratio and WZ at a high V/III ratio [25-27]. Interestingly, models used to explain polytypism in both MOVPE and MBE-grown nanowires are most often based on the same conceptual idea, that the interface energies related to the formation of the new nucleus determine if it is a ZB or a WZ nucleus, and many are based on a model outlined by Glas et al. [28]. Based on our experimental findings, this thesis discusses how the two apparently different behaviors of MOVPE and MBE-grown nanowires are related to each other.

Because nanowires are typically characterized after they have been grown and removed from the epitaxy equipment, the actual state of the nanowire and its seed particle during growth can only be estimated, with varying accuracy. To truly determine what governs the growth of the different crystal structures, observations down to the atomic scale while the nanowire is growing would be greatly beneficial. During the last five years, reports of using *in situ* transmission electron microscopy (TEM) to monitor growth of nanowires have been published, which have revealed remarkable dynamics at the growth interface between the seed particle and the nanowire [29-31]. Together with collaborators at the IBM T.J. Watson Research Center, studies on GaAs nanowire growth in both the WZ and ZB crystal structures were carried out (Paper IV). The studies present the first *in situ* TEM on growing GaAs nanowires, and more importantly, the first observation of both WZ and ZB growth within the same nanowire. Earlier studies on sapphire, Si, Ge and GaP, showed that the nanowires grow with a oscillating tri-junction at the vapor-liquid-solid interface, and the GaAs ZB also did this in our study. However, WZ showed a striking difference: growth proceeded without an oscillating tri-junction, but instead with a slow step flow across the top facet. Once again, the use of *in situ* TEM reveals dynamics at the growth interface impossible to deduce from *ex situ* analysis of structures after growth has been terminated.

The outline of this thesis is as following: in Chapter 2, basic concepts concerning crystals and their growth using vapor phase epitaxy are discussed. Chapter 3 discusses the characterization tools used in this work: X-ray diffraction, electron microscopy and

photoluminescence. Chapter 4 is dedicated to nanowire growth, where some of my own contributions are put into perspective with other results. With high quality crystal structures, some differences between WZ and ZB crystals, and the interfaces between the two, are discussed in Chapter 5, based on the studies in this thesis. Finally, some concluding remarks and an outlook are found in Chapter 6.

2 Crystal growth and epitaxy

The fabrication of complex semiconductor crystals is usually performed with a bottom-up technique, where the crystal is grown atom by atom on a template, typically another crystal. Growing material in an ordered manner on a template is referred to as "epitaxy", from the Greek words "epi" ("above") and "taxis" ("in an ordered manner"). The growth of the crystal is controlled by thermodynamics, describing the driving forces of the processes involved, and kinetics, describing the rates at which they occur. Several growth techniques can be used for growing nanowires, but metal-organic vapor phase epitaxy (MOVPE) is one of the most common. Before going into details regarding the processes involved in the growth, some basic concepts regarding crystal structures, crystal shapes, and defect types are discussed.

2.1 Crystal Structure

2.1.1 Crystal symmetry

A crystalline structure is defined by a repeating, three dimensional pattern of atoms (or ions, or molecules) with a fixed distance between the constituent parts. A change in the repeating pattern will thus change the crystal structure. For III-V semiconductors[2], the two most common crystal structures are the cubic zincblende (ZB) phase and the hexagonal wurtzite (WZ) phase. In bulk material, ZB is the stable phase for most III-V materials, except for the Group III nitrides (III-N) where WZ is the stable phase. In nanowires, however, it is possible to grow pure WZ, pure ZB or a mixture of the two phases, independently of the stable structure of the bulk compound. It is also possible to grow more complicated crystal structures, such as the 4H phase, but these are much less often observed.

For ZB, the smallest repetitive unit, called the unit cell, consists of a cube with Group III atoms in the corners and at the centers of each face, an arrangement also referred to as face-centered cubic. Within the unit cell, four Group V atoms are positioned so that

---

[2] The III-V semiconductors are formed by atoms from Groups III and V of the periodic table, for example binary GaAs or ternary GaInAs.
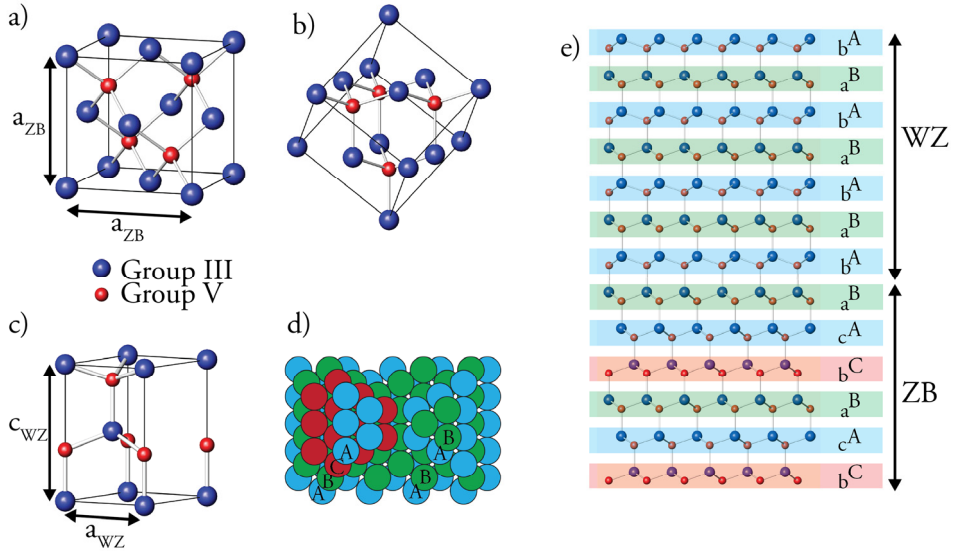
Figure 2.1. (a,b) The unit cell of ZB in different orientations. (c) Unit cell of WZ. (d) close-packed layers, cubic close packing to the left and hexagonal close packing to the right. (e) ZB and WZ in the same structure, showing the close-packed stacking sequences.

each binds with four Group III atoms in a symmetric tetrahedral coordination, see Figure 2.1a. The crystal lattice is built up by repeating the unit cell in all three directions. Any position in the lattice has its surroundings repeated identically a distance of one unit cell away. For a cubic unit cell, all sides are of equal length, and only one lattice constant is used, usually labeled a. The crystal structure, together with the lattice constant, are enough to describe uniquely where in the lattice the atoms are placed and their distances from each other. As the III-V semiconductors are compound materials, it is possible to identify sublattices within the structure, where only one of the constituent atoms is considered. In ZB, both the Group III and Group V atoms are positioned in face-centered cubic cells, translated ¼ of a unit cell with respect to each other. The positions of the atoms within the lattice are referred to as lattice positions.

For WZ, the unit cell is hexagonal, with a rhombus as a base (having angles of 60° and 120° at its corners). Similarly to ZB, Group III atoms are positioned in the corners of the unit cell, and have a tetrahedral coordination with four Group V atoms. A drawing of the WZ unit cell is shown in Figure 2.1c. As the hexagonal unit cell is not symmetric in all three directions, one lattice constant is not enough to define the unit cell size. In addition to the lattice constant a, describing the size of the base rhombus, the lattice constant c is used to describe the height of the unit cell.

Both ZB and WZ are close-packed structures and differ only in the position of the next-nearest atom within the Group III or Group V sublattice. Comparing the lattice positions along the diagonal of the ZB unit cell and the lattice positions along the c axis

of the WZ, one sees that the stacking sequence in ZB is …ABCABCABC… where every third bilayer is repeated (a bilayer is one layer each of the Group III and Group V atoms). For WZ, the stacking sequence is …ABABAB… and every second bilayer is repeated. Figure 2.1b and c illustrate the difference between the two structures. To further visualize the different stacking orders, consider the stacked spheres in Figure 2.1d. To arrange the spheres in a single layer as closely as possible, they should be placed in a hexagonal pattern. When putting another hexagonal layer on top of the first, there are two possible positions, but they are equivalent. Crucially, when adding a third layer of spheres, it may either be placed directly above a sphere of the first layer, or above a void between the spheres of the first layer. If the third layer is placed above a sphere of the first layer, the …ABABAB… packing sequence of the WZ is achieved. If the third layer is above a void, the …ABCABCABC… of ZB appears. As each letter denotes the position of a III-V bilayer, it is also possible to write the stacking order as …AaBbCcAaBbCc… or …AaBbAaBb… to take both the Group III (upper case) and Group V (lower case) atoms into account, see Figure 2.1e. The WZ structure is a hexagonal close packing, and ZB a cubic close packing. In the direction of the close-packed bilayers, WZ repeats every 2 bilayers, and ZB repeats every 3 bilayers. In Ramsdell notation, these two are called 2H (two bilayers with hexagonal stacking) and 3C (three bilayers with cubic stacking), respectively. Similarly, structures with longer repetitive segments are denoted with the number of close-packed bilayers in the structure and a letter based on the overall symmetry (H for hexagonal, C for cubic, or R for rhombohedral). Another crystal structure that will be briefly discussed in this thesis is 4H, which has the stacking order …ABACABAC…

To describe directions and planes in crystals, indices based on the unit cell geometry are used. For the cubic case, three digit Miller indices are usually used [32]. Let three orthogonal vectors of equal length, $\mathbf{a_1}$, $\mathbf{a_2}$ and $\mathbf{a_3}$, define the unit cell. A crystal plane (hkl) cutting through the crystal will intersect the three axes at $\mathbf{a_1}/h$, $\mathbf{a_2}/k$ and $\mathbf{a_3}/l$, where the integers hkl are written with a common greatest divisor of 1. That is, a plane orthogonal to $\mathbf{a_1}$ has the Miller index of (001). The set of all planes made equivalent to (hkl) by the symmetry of the lattice is written as $\{hkl\}$. To describe directions, $[hkl]$ is used to denote the direction $h\mathbf{a_1}+k\mathbf{a_2}+l\mathbf{a_3}$. For directions equivalent to $[hkl]$ due to symmetry, $\langle hkl \rangle$ is used. For negative indices, a bar above the index is used. For examples of planes in a ZB crystal, see the top row in Figure 2.2.

In this thesis, four digit Miller-Bravais indices will used to describe directions and planes in hexagonal crystals [33]. For the rhombus base plane of the unit cell, three lattice vectors are defined, all of equal length, with angles of 120° between them. The fourth axis is set along the height of the unit cell (c-axis). The four indices used are denoted $hki.l$, where $i=-(h+k)$. The three first indices are related to the base plane, and l to the c-axis, so that the $\{000.1\}$ are planes parallel to the base plane. The dot between i and l is used to differentiate between Miller and Miller-Bravais indices. For examples of planes in a hexagonal structure, see the bottom row in Figure 2.2.
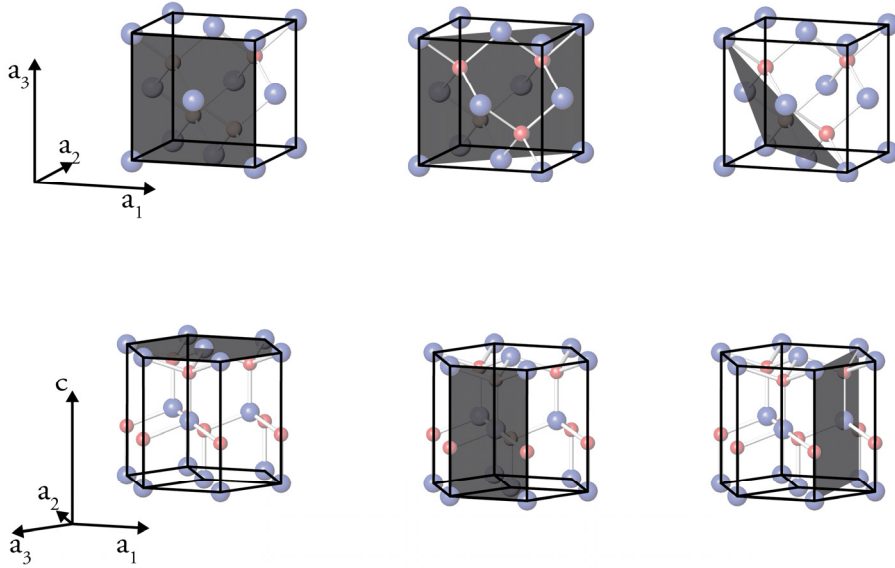
Figure 2.2. The top row shows a ZB unit cell with (010), $(\bar{1}10)$ and (111) planes highlighted. The bottom row shows WZ with (000.1), $(0\bar{1}1.0)$ and $(\bar{1}\bar{1}2.0)$ planes highlighted.

For III-V semiconductor crystals, some planes will have a polarity due to the two different types of atoms in the crystal. Take, for example, the $\{111\}$ planes of ZB. The two sides of the planes have either a Group III or a Group V atom outermost. With a III-V wafer with $\{111\}$ surfaces, one side of the wafer will be Group III terminated and the other Group V terminated, which will lead to their having different properties. To differentiate the two, it is common to write an A after the indices for Group III terminated surfaces and B for Group V terminated surfaces. It is also possible to write specific planes, so that the (111) and $(\bar{1}\bar{1}\bar{1})$ denote the Group III and Group V terminated side of $\{111\}$-type faces, respectively.

Another useful concept which may be introduced based on the Miller and Miller-Bravais indices is the reciprocal lattice. In real space, any lattice vector can be written as (using Miller indices as an example):

$$\boldsymbol{r}_n = n_1 \boldsymbol{a_1} + n_2 \boldsymbol{a_2} + n_3 \boldsymbol{a_3} \qquad (2.1)$$

with n_1, n_2 and n_3 as integers. A reciprocal lattice vector $\boldsymbol{r}_m^*$ can similarly be defined as:

$$\boldsymbol{r}_m^* = m_1\boldsymbol{a_1^*} + m_2\boldsymbol{a_2^*} + m_3\boldsymbol{a_3^*} \qquad (2.2)$$

where $\boldsymbol{a_1^*}$ is normal to both $\boldsymbol{a_2}$ and $\boldsymbol{a_3}$. We also have that $\boldsymbol{a^*} \cdot \boldsymbol{a} = 1$, which gives the reciprocal lattice vector units of 1/length. The reciprocal lattice is useful when considering diffraction, as will be further be discussed in Chapter 3. The left hand side of Figure 2.3 shows the ZB and WZ unit cells viewed in the $[00\bar{1}]$ and $[000.\bar{1}]$ directions, respectively, each with two types of lattice plane marked. To the right, the equivalent reciprocal lattice points are drawn.
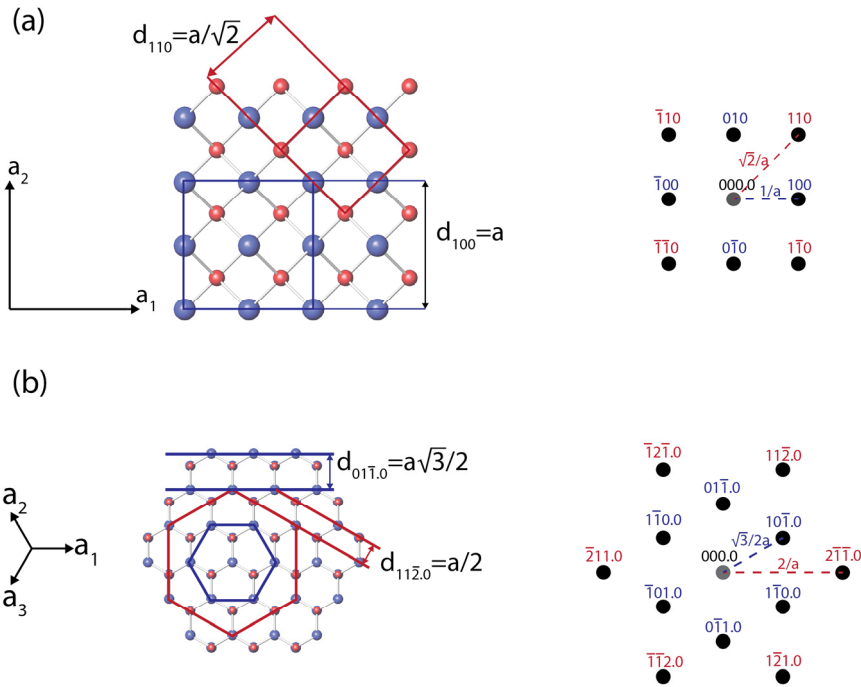
Figure 2.3. (a) The ZB structure viewed along $[00\bar{1}]$ in real space (left) and its reciprocal lattice points (right). The blue square has sides parallel to $\{001\}$, the red has sides parallel to $\{011\}$. (b) WZ viewed along $[000.\bar{1}]$ in real space (left) and its reciprocal lattice points (right). The blue hexagon has sides parallel to $\{10\bar{1}.0\}$, the red has sides parallel to $\{11\bar{2}.0\}$.

2.1.2 Crystal shapes and faceting

No crystal is infinitively large, and all crystals have surfaces. At the surface, the periodic structure of the crystal is broken, and the surface atoms will not have the same bond configuration as the bulk counterpart. For a solid crystal, having surface atoms has to be less energetically favorable for the crystal to be stable, otherwise it would undergo sublimation to reduce the volume of bulk atoms. The excess energy of a surface compared to the bulk is called the surface energy, which is of paramount importance when it comes to crystal shapes and crystal growth.

The surface energy of a crystal is as a first approximation proportional with the density of dangling bonds. Cleaving a crystal along a specific crystal plane, a number of bonds has to be broken and the more bonds per unit area that are broken, the higher the surface energy of the specific crystal plane. This way, it is possible to compare crystal planes of different crystal structures, by just geometrical considerations [34]. However, the surface energy can be altered due to surface reconstructions, where the bond configuration of the surface atoms are changed compared to their bulk counterpart. For compound material such as GaAs, the surface coverage of Ga and/or As atoms will also have an effect on the surface energy [35].

For a growing crystal, differences in the surface energies for different facets will determine its shape. To minimize the crystal's surface energy, facets with the highest surface energy will have the highest growth rate, causing surfaces with lower surface
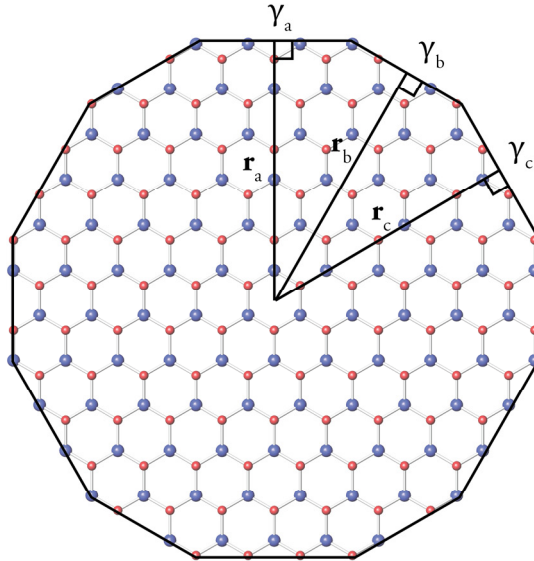
Figure 2.4. A two-dimensional crystal with its equilibrium crystal shape, which can be described with the Wulff theorem. Here, the facets have similar surface energies, and hence are similar in size.

energies to be larger. During growth using MOVPE, as in this work, the growth system is not at equilibrium, and kinetics will strongly influence the crystal shape, but the concept of the equilibrium crystal shape is still of interest. At equilibrium, a simple relation can be found between the resulting facets and their surface energies, given by the Wulff theorem [36, 37]:

$$\frac{r_j}{\gamma_j} = constant \tag{2.3}$$

Here, $\mathbf{r}_j$ is a vector drawn normal to the crystal facet j from the center of the crystal, γ_j is the surface energy of the facet. Figure 2.4 shows a two-dimensional crystal with three different facets formed. If γ_b is increased, $\mathbf{r}_b$ also has to increase its length. Facet a and c will then increase in length, and if the surface energy of facet b is high enough, only a and c will be left. Allowing the crystal to reach equilibrium, the differences in surface energies will be reflected in the equilibrium shape of the crystal. In most cases, a growing crystal will not be able to fully reach its equilibrium shape, as the system is quenched at the end of the growth process. Still, kinetics which are fast enough will allow for growth to proceed on high energy facets, promoting formation of low energy facets, similar to the formation of the equilibrium shape.

2.1.3 Defects

A real crystal deviates from a perfect, periodic structure. By definition, the crystal surfaces are enough to break the symmetry, but in addition, defects within the bulk of the crystal will always occur at room temperature. The defects may either be localized point defects or extended dislocations or grain boundaries. Point defects can be separated into intrinsic defects, where the stoichiometry of the crystal is not changed, or extrinsic, where foreign atoms are introduced into the lattice. Defects in a crystal play a crucial role in its electronic properties, where the density of extrinsic defects, called dopants, is used to alter the concentration of carriers available for conduction. Intrinsic defects in semiconductors can also alter their electronic properties. Dislocations and grain boundaries are involved in permanent deformation of a solid under stress, where movement of dislocations or along grain boundaries relieves some of the stress applied to the solid.

If we consider intrinsic defects first, they may be separated into three different types: Schottky defects, Frenkel defects, and anti-site defects. If one Group III and one Group V atom are removed from a III-V semiconductor, as shown in Figure 2.5a, a pair of vacant sites is generated, which is called a Schottky defect. If a Group III or a Group V is moved out from its lattice site to an interstitial site, as shown in Figure 2.5b, a Frenkel defect is created. In compounds where the constituent atoms are only weakly ionized, as in the III-V semiconductors, a Group III and a Group V atom may exchange sites, and anti-site defects are formed, as is shown in Figure 2.5c. For all three types of defects,
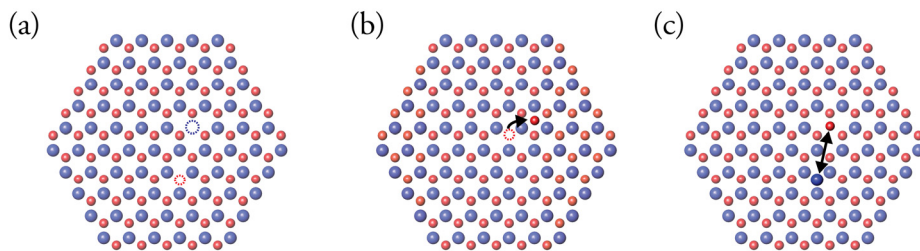
Figure 2.5. Intrinsic point defects in a III-V 2D crystal. In (a), a pair of III-V atoms are missing, resulting in a Schottky defect. (b) If one atom is moved from its lattice position to an interstitial site, a Frenkel defect is created. In (c), an anti-site defect is shown, where a III-V pair has exchanged positions.

the overall stoichiometry and charge of the crystal has not been changed. They also all require energy in order to be formed. However, thermal energy at room temperature is sufficient to create these intrinsic point defects [32].

If a defect changes the stoichiometry of the crystal, extrinsic defects are formed. If the extrinsic defects are created intentionally, they are often called solutes or dopants, but they are often created unintentionally, and are then referred to as impurities. The solutes or impurities may be found on both interstitial sites and lattice sites, where in the latter case they substitute for an atom in the host crystal. Taking Si in GaAs as an example, Si could substitute for either Ga or As, with different effects on the electronic properties of the semiconductor. Substituting Ga, which has three valence electrons, the four valence electrons of Si will result in a net increase of one electron to the carrier concentration and so Si acts as a n-type dopant. If the Si takes an As site, one extra hole is created instead, and the Si atom acts as a p-type dopant.

If atoms in a crystal are out of place along a line through the crystal, the defect is called a dislocation. The easiest type of dislocation to visualize is the edge dislocation shown in Figure 2.6a. Imagine cleaving the crystal partly and apply pressure on the upper part so that it slides a vector **b** on top of the lower part. The vector **b** is called the Burgers vector of the dislocation. If the bonds between the upper and lower part are reformed, excess material is gathered where the cut has stopped, the dark line. This line is called the dislocation line and continues through the crystal perpendicular to the plane of glide. The defect can propagate through the crystal, by breaking the bond marked by "1" (grey, solid) in Figure 2.6b and creating the bond marked "2" (grey, dashed). The dislocation moves along a particular plane, called the glide plane, containing both the Burgers vector and the dislocation line. As the propagation of a line defect throughout a crystal involves breaking bonds, an energy barrier for the process exists, called the Peierls barrier or the intrinsic lattice resistance. The height of the barrier depends on the bonds in the crystal and in covalently bonded materials it is highly dependent on the direction of movement [38].

(a)   (b)
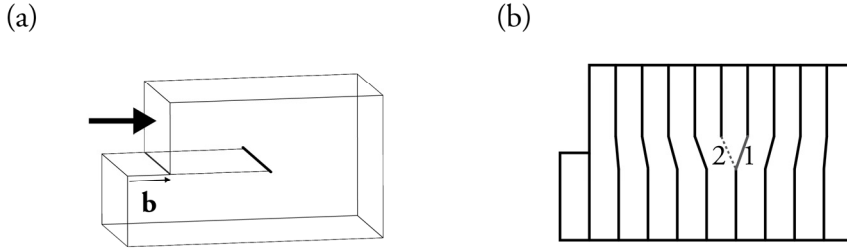
Figure 2.6. (a) Illustration on creation of a line dislocation by partially cutting a crystal. Translating the upper part of the crystal by a vector, b, places excess material at the end of the cut. By breaking the bond marked "1" in (b), and forming bond "2", the dislocation propagates further into the crystal.

As with point defects, the creation of linear defects is an endothermic process. In the core of the dislocation, the bonds between atoms are not in their equilibrium configuration: they are not at minimum enthalpy, and the dislocation has to contain energy and entropy per unit length. The total energy associated with the linear defect increases with the length of the dislocation. However, creation of linear defects can minimize the total free energy of a system. When two layers with different lattice constants are bonded together at an interface, if the layers are large enough, dislocations will be created at the interface. The increase in total energy caused by creating the dislocations is balanced by the relieved stress.

The total energy associated with a dislocation consists of the distorted bonds in its core and the elastic field from elastically strain bonds further away, such that:

$$E_{total} = E_{core} + E_{elastic\ strain} \tag{2.4}$$

To calculate the elastic strain contribution, integration over the strain energy around the dislocation has to be performed, which can be somewhat difficult, depending on the symmetry of the dislocation. However, for an edge dislocation, the result is rather simple:

$$E_{elastic\ strain} = \frac{G * b^2}{4 * \pi * (1 - \nu)} * ln\left(\frac{R}{r_0}\right) \tag{2.5}$$

where G is the shear modulus and ν is the Poisson ratio. r_0 is the radius of the dislocation core and R is the radius of a cylinder containing the dislocation. In an infinite crystal with only one dislocation, R should be infinite, but in real crystals, the finite grain size and interaction with other dislocations limits R. r_0 is also hard to determine accurately, but a reasonable approximation is for r_0 to have the same

magnitude as the Burgers vector **b** (the magnitude of the Burgers vector is here denoted as b).

There is, to date, no easy way of accurately calculating the other energy contribution, the core energy. However, the core energy should depend upon the shear modulus of the crystal and if we take the core radius to be of the same magnitude as the Burgers vector, we can approximate the core energy as

$$E_{core} = \frac{G * b^2}{2 * \pi}$$

(2.6)

The total energy per length unit of the edge dislocation can then be written, with $r_0 = b$, as:

$$E_{total} = \frac{G * b^2}{4 * \pi (1 - \nu)} * \left(ln \frac{R}{b} + B \right)$$

(2.7)

Where B is a constant best approximating the core energy to the particular case, typically $B=1$. Equation 2.7 now only weakly depends on R, and may be simplified to

$$E_{total} = \alpha * G * b^2$$

(2.8)

Where α is typically found from measurements to be 0.5–1.5 and depends on crystal properties such as the grain size and the type of dislocation. Typical values for the line energy of a dislocation are a few electronvolts per nanometer. As can be seen, to minimize the dislocation energy, the dislocation attempts to minimize its own line length, and the length of its Burgers vector [39].

2.2 Vapor phase epitaxy

One way to fabricate crystalline structures is to use a bottom-up approach, where molecules and particles self-assemble into specific structures. For semiconductor crystals, such structures may be grown using epitaxy techniques, where the crystal is grown atom by atom. In this work, metal-organic vapor phase epitaxy (MOVPE) has been used, and some of the technique's basic concepts are introduced below.

The manufacturing of crystals by MOVPE is a complex process with several interdependent steps. Because volatile precursors are used, gas phase reactions occur even before the precursors reach the substrate where growth is intended to take place. The gas phase reaction rates are determined by the gas concentrations and the process temperature, which are directly controlled by the growth equipment. The volatile precursor molecules may react with each other at the substrate surface, but may also

decompose to leave adatoms adsorbed on the surface. Once adatoms are present on the surface, they diffuse until they either meet other adatoms and form a nucleation site, or they become incorporated into pre-existing steps on the surface, or they desorb without contributing to the growing crystal. As with the gas reactions, these surface processes are determined by the surface concentrations. However, in contrast to the gas concentrations, surface concentrations are not directly accessible to measurement.

2.2.1 Surface processes

Adsorption/desorption

As precursor molecules are fed to the growth system in the gas phase, the growing crystal surface acts as a sink for incoming molecules, and a concentration gradient will occur close to the substrate surface, with a higher concentration of precursor molecules further away from the substrate. This concentration gradient drives molecules in the gas towards the substrate surface by a process of diffusion. However, close to the substrate surface, other processes become dominant.

As a molecule in the gas phase approaches the substrate surface, it will eventually feel an attractive force from the substrate due to interactions with the surface atoms. The attractive force arises from dipole interactions between the molecule and the substrate. Even non-polar molecules are attracted, because they behave as oscillating dipoles, which causes instantaneously induced dipoles. The attractive force is known as the van der Waals force, and begins to influence the gas molecules when they are a few atomic distances away from the surface.

The van der Waals force acting on a gas molecule makes it loosely bound to the substrate surface, trapped in a state known as physical adsorption, or physisorption. The adsorbed molecule is able to diffuse on the substrate (a process described in more detail below), and it may further decompose if it is a precursor molecule, or desorb again if given enough energy, or create chemical bonds with the surface atoms and become a part of the crystal. If the adsorbed molecule creates new chemical bonds with the surface atoms, it is in a chemisorbed state, and is a part of the solid crystal. Only some of the adsorbed molecules will be incorporated into the crystal, and the fraction of adsorbed molecules that becomes chemisorbed is called the sticking coefficient, S_c. The sticking coefficient can be defined as [36]:

$$S_c = \frac{R_c}{J_i} \tag{2.9}$$

Where R_c is the rate of chemisorption and J_i is the flux of molecules hitting the surface. From the Knudsen equation, $J_i = k * p / \sqrt{MT}$, with partial pressure p, molar weight M, temperature T and k as a proportional factor, we see that the impinging flux is directly dependent on two accessible parameters of the growth process: temperature

and the precursor gas pressure. However, the rate of chemisorption is more complex. For low J_i and low surface coverage of adsorbed molecules, R_c can be written as:

$$R_c = \frac{J_i \delta}{1 + k_d/k_c} \tag{2.10}$$

Here, δ is the fraction of molecules incident upon the surface that is adsorbed, $k_{d/c}$ is the reaction rate constant for desorption and chemisorption, respectively. The rate constants follow the Arrhenius equation:

$$k_{d/c} = v_{d/c} e^{-E_{d/c}/k_B T_s} \tag{2.11}$$

Where $v_{d/c}$ are pre-exponential factors and $E_{d/c}$ are activation energies for desorption and chemisorption, respectively. k_B is the Boltzmann constant and T_s is the substrate temperature. The desorption and chemisorption rate constants depend on the substrate surface, for example the chemisorption rate decreases drastically on a H-passivated Si surface, whereas the chemisorption rate increases at atomic steps on an otherwise atomically flat surface [36]. In general, surfaces with a high density of dangling bonds and high surface energies will have a higher chemisorption rate. Hence, when growing structures with several different types of facets and a complex geometry, the sticking coefficient may vary significantly across the sample.

Surface diffusion
Between adsorption and potential chemisorption or desorption, the adsorbed molecules are able to move around on the surface, a process called surface diffusion. The distance a molecule is able to move before chemisorption or desorption is described as the surface diffusion length Λ_s [36]:

$$\Lambda_s = 2\sqrt{D_s \tau_s} \tag{2.12}$$

Here, D_s is the surface diffusion coefficient and τ_s is the average life-time of the molecule on the surface. Both D_s and τ_s are temperature-dependent and vary with the surface structure. Using the Arrhenius equation, and taking both chemisorption and desorption into account, it is possible to rewrite the surface diffusion length as:

$$\Lambda_s = a \sqrt{\frac{v_D}{v_c}} e^{\frac{(E_c - E_D)}{2 k_B T_s}} \tag{2.13}$$

Where a is the distance between adsorption sites, $v_{D/c}$ are pre-exponential factors for surface diffusion and chemisorption, respectively, E_D is the activation energy for surface diffusion, and E_c the chemisorption energy. In a temperature regime where desorption

is significant, E_c-E_D is always positive and the diffusion length will decrease with increasing temperature. The effect results because desorption rates are higher with increasing temperature, and because adatoms are more likely to desorb rather than being incorporated into the solid. However, at low enough temperatures, the desorption rate is negligible compared to chemisorption rate, and only the activation energy for surface diffusion limits the surface diffusion length, which is then given as:

$$\Lambda_s = a\sqrt{v_D}e^{\frac{(-E_D)}{2k_BT_s}} \tag{2.14}$$

In this temperature regime, the diffusion length increases with temperature. Different crystal planes and directions will have different E_D, which could cause highly anisotropic diffusion behavior [40]. In addition, different species will have different pre-exponential factors and activation energies, and by choosing growth conditions carefully, it is possible selectively to suppress diffusion of one species during growth of ternary crystals (Paper xiii).

2.2.3 Nucleation and adatom incorporation

For a solid crystal to grow, a phase change from a liquid or vapor to the solid phase is required. If this is to happen, the system has to be out of equilibrium, so that it moves towards its lowest energy state, i.e. towards equilibrium. The driving force for a phase change is given by the difference in the chemical potential $\Delta\mu$ between the two phases, α and β:

$$\Delta\mu = \mu_\alpha - \mu_\beta \tag{2.15}$$

At chemical equilibrium $\Delta\mu$ equals zero, and no phase change will occur [37]. For a system with constant temperature and pressure, the Gibbs free energy is also at a minimum at chemical equilibrium.

The difference in chemical potentials between the two phases is closely related to the supersaturation. Taking the simplest case as an example, an ideal gas in a single-component system, the relation between the difference in chemical potential and the vapor supersaturation is given by [36]:

$$\Delta\mu = \mu_v - \mu_\beta = k_BT\ ln\left(\frac{p}{p_v}\right) \tag{2.16}$$

Where μ_v is the vapor chemical potential, and μ_β is either the liquid or solid phase of the element, with which the vapor is in chemical equilibrium at its saturation vapor

pressure p_v. Increasing the pressure p above p_v, the vapor becomes supersaturated and formation of phase β becomes thermodynamically favorable.

For an adatom to be incorporated, it either has to find an epitaxial site such as an edge or kink site, or form a new nucleus together with other adatoms. Forming a new nucleus will cause a volume of adatoms to change phase, but at the same time create new facets of the solid. Hence, the change in Gibbs free energy of a new nucleus will have two terms, one volume related and one surface related. From classical nucleation theory, we can then write the change in Gibbs free energy for a new nucleus as:

$$\Delta G = -\Delta \mu \frac{V}{V_{mn}} + \sum^{n} \gamma_n A_n \qquad (2.17)$$

Here, V is the volume of the nucleus, V_{mn} its molar volume; γ_n the surface energy of facet n of the nucleus, and A_n its area. For a three dimensional nucleus, the volume term will be dependent on r^3, whereas the surface term will have a r^2 dependency. As the volume of the nucleus increases, the phase change will decrease the Gibbs free energy, driving the system closer to chemical equilibrium. At the same time, the increased surface area of the crystal will increase the Gibbs free energy. Hence, the change in Gibbs free energy for the nucleus will have a maximum, ΔG^*, the nucleation barrier, at a certain size, the critical nucleus size. For a nucleus this size or larger, it is energetically favorable to increase in size, and more and more adatoms will be incorporated into the growing island. Nuclei smaller than the critical size are unstable and will evaporate. From Equation 2.17 it can be seen that to decrease ΔG^*, and hence increase the possibility for nucleation, either the supersaturation may be increased (see Equation 2.16), or the surface energies of the new nuclei should be decreased. For nanowire growth, it is local changes in the surface energies of new nuclei that causes the highly anisotropic growth, as will be discussed further in Chapter 4.

2.2.4 Precursor chemistry

In vapor phase epitaxy, the input gas is typically a mixture of a carrier gas, such as H_2, and precursor gases. For epitaxy of III-V materials, the precursor gases are usually metal-organic or hydride molecules. In this thesis, GaAs has been grown from the metal-organic precursor trimethylgallium ((CH_3)$_3$Ga, or TMGa) and the hydride arsine (AsH_3), with the addition of gaseous hydrogen chloride (HCl) as an additive. The precursor gases are diluted in a carrier gas – here H_2 is used. Other precursors for growing GaAs by vapor phase epitaxy do exist, which offers a large freedom to choose a precursor to fit a specific process, but this will not be discussed here. As a large variety of precursors exists, the number possible reactions between different molecules makes precursor chemistry very complex. A good overview of common precursors and their kinetics for metal-organic vapor phase epitaxy can be found in ref [41, 42].

To leave the metal atom of the precursor molecule free for incorporation, the ligands have to leave the parent molecule. This pyrolysis of the precursors can either be homogeneous, where the molecule decomposes in the vapor; or heterogeneous, where the molecule decomposes with the aid of a surface. In addition, different precursor molecules might affect the decomposition of each other.

The Group III metal-organic precursor used in this thesis, TMGa, is known to decompose homogeneously, with an onset of pyrolysis at around 375°C, and it is close to being fully decomposed at 475°C in a H_2 ambient [43]. For the homogeneous pyrolysis, it is believed that decomposition is done via a chain reaction, starting with a reaction between CH_3 and H_2. The released atomic H then attacks a parent molecule, forming another CH_3-H from one of the ligands. TMGa is also able to decompose heterogeneously on GaAs surfaces, which is an important decomposition pathway in the absence of H_2 as carrier gas [44].

For AsH_3, the pyrolysis proceeds via heterogeneous decomposition on the GaAs surface, and roughly half of the AsH_3 molecules are decomposed at 475°C [45]. It is thought that the decomposition pathway starts with adsorption of AsH_3 onto the surface, followed by consecutive dissociation, one H at the time, eventually leaving atomic As adsorbed on the surface. The dissociated H atoms remain on the surface until two of them combine to form H_2, which then desorbs [46].

Using MOVPE to grow GaAs crystals, both TMGa and AsH_3 are most often supplied simultaneously in the H_2 carrier gas. By mixing TMGa and AsH_3, the pyrolysis of both precursors is enhanced [45, 47]. In combination with a GaAs surface, the temperature at which the precursors are 50% decomposed is lowered by around 100°C compared to the individual precursors on their own. A possible explanation is that the precursors form a Lewis acid-base adduct, and the three ligands together form CH_4. As an result, the two precursors decompose at the same temperature for a V/III ratio of 1. For higher V/III ratios, the excess AsH_3 is likely to decompose via heterogeneous decomposition on the GaAs surface, and for V/III ratios lower than 1, the excess TMGa undergoes homogeneous decomposition in the gas phase.

3 Characterization methods

The focus of this thesis is the crystal structures of semiconducting nanowires, which means that the arrangement of their atoms with respect to each other is of central importance. With a different atomic arrangement, the optical and electrical properties of the semiconductor will also be different. Numerous methods can be used to probe the differences between ZB and WZ GaAs, and a combination of several techniques is typically necessary to gain a more complete picture. Here, single crystal X-ray diffraction is used to extract information about lattice plane spacings and orientations from ensembles of as-grown nanowires. The diffraction signal averages information from a few square millimeters of the sample surface, and millions of nanowires may contribute to it. In order to determine morphology, and observe the structure variations within as well as between single nanowires, various types of electron microscopy are used. For an overview of the morphology of grown nanowires, scanning electron microscopy (SEM) is used, which gives a spatial resolution down to a few nanometers. Transmission electron microscopy (TEM), where electrons pass through the sample, allows the imaging of atomic columns of a crystalline sample and the determination of crystal structure down to single bilayers. In electron microscopy, X-rays are generated as the electron beam is inelastically scattered by the sample, and this can be used to determine the elemental composition of the sample, with a technique called X-ray energy dispersive spectroscopy (XEDS). Finally, photoluminescence is used to discover when the optical properties of the GaAs WZ-ZB heterostructures has been affected. In this, a laser with a higher photon energy than the band gap of the semiconductor is used to generate electron-hole pairs, and as they recombine and emit photons at lower energy, the spectrum of emitted photon energies gives a fingerprint of the band gap and band alignment of the structure.

3.1 X-ray diffraction

A very powerful technique for analyzing crystalline material is X-ray diffraction (XRD). The sample is irradiated with X-rays, which interact with the sample atoms, diffracting off its crystal planes, and changing the direction and intensity of the X-ray beam. By measuring the angles of the incident and exit beams at which the strongest diffraction occurs, information on lattice plane spacings and their angle with respect to the sample surface is obtained. By carefully analyzing the recorded data, it is possible to determine

parameters such as the crystal structure, composition, mosaicity, layer thickness (for thin films), strain, and grain sizes [48].

The phenomena underlying X-ray diffraction is wave interference. Similar behavior can be observed in macroscopic waves, for example, when water waves are generated by two water bugs as they jiggle their legs at a constant rate on a calm water surface. Each bug will generate a series of circular waves around them, and as the waves pass each other, they will interfere. At some locations on the water surface, the two series of waves will cancel each other out – destructive interference – and at some locations they enhance one another – constructive interference. If the distance between the water bugs changes, the locations of destructive and constructive interference will also change. By only looking at the pattern of destructive and constructive interference, it is possible to tell where the two water bugs are. The same principle is used in X-ray diffraction: knowing at which angles constructive interference occurs, it is possible to tell where the lattice planes are located.

When the radiation field of X-rays interacts with the electron cloud around an atom, its electrons are forced to oscillate with the same frequency as the radiation. The oscillating electrons re-emit new radiation with the same frequency, but in all directions around the atom (in the plane perpendicular to the electron's oscillatory motion). This elastic scattering process is known as Thomson scattering and in crystals, where the scattering atoms are periodically arranged, constructive and destructive interference will occur between the re-emitted light, at angles depending on the periodicity of the crystal planes.

Consider a row of equally spaced atoms which are irradiated with a plane wave perpendicular to the row, as in Figure 3.1a. Each atom will scatter the incident wave and act as a point source for re-emitted waves (compare with the water bug example above). As the re-emitted waves interfere with each other, a new wave front will appear perpendicular to the row of atoms. From a distance, it will look like the initial plane wave has been transmitted through the row. However, the exit wave fronts perpendicular to the row of atoms are not the only allowed direction for exiting wave fronts, which can be graphically proven, as in Figure 3.1b. Mathematically, the conditions for constructive interference are given by the Laue conditions, here in one dimension:

$$a(\cos \alpha_0 - \cos \alpha_n) = n\lambda \qquad (3.1)$$

where *a* is the distance between the atoms, α_0 the angle of the incident wave with respect to the row of atoms and α_n the exit angle. λ is the wavelength of the wave and *n* is an integer, 0,1…,n. The trivial solution, where $\alpha_0 = \alpha_n$ and *n=0* gives the zero order Laue zone. Consequently, the solution for *n=1* gives the first order Laue zone. For a three

dimensional crystal with lattice distances a_1, a_2 and a_3[3], the Laue conditions are typically written as:

$$a_1(\cos\alpha_0 - \cos\alpha_n) = n_h\lambda$$
$$a_2(\cos\beta_0 - \cos\beta_n) = n_k\lambda \qquad (3.2)$$
$$a_3(\cos\gamma_0 - \cos\gamma_n) = n_l\lambda$$

Knowing λ and which lattice planes give rise to the diffraction, the lattice distances can be calculated.

The Laue conditions can also be written using wave vectors. An X-ray beam can be approximated to a plane wave, Ae^{ikr}, where A is the amplitude of the wave, $\boldsymbol{k}$ the wave vector of the light with a wavelength of $\lambda = 2\pi/|\boldsymbol{k}|$. If $\boldsymbol{k_0}$ is the incoming wave vector
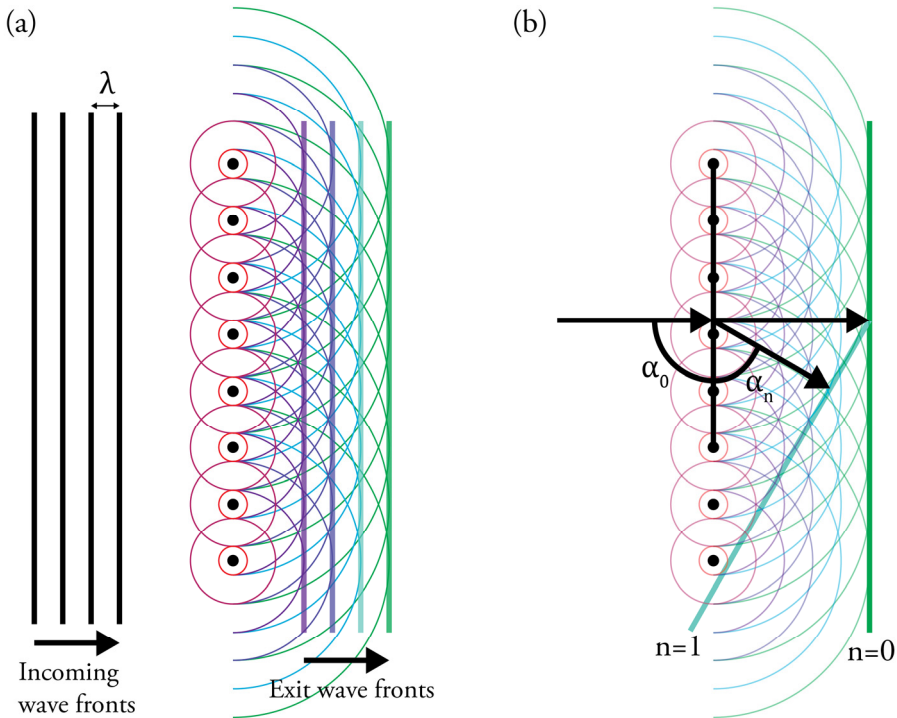
Figure 3.1. Scattering of incoming wave fronts from a row of atoms. (a) Each atom re-emits waves with the same wavelength as the incoming waves, acting as a line of point sources. Constructive interference will cause the waves to appear transmitted.. Constructive interference also results in wave fronts at oblique angles, with the angles given by the Laue conditions, as is graphically shown in (b).

---

[3] For a crystal where a_1, a_2 and a_3 define the unit cell, as, for example, in ZB.

and $\boldsymbol{k}$ the outgoing (or diffracted) wave vector, then the scattering wave vector $\boldsymbol{Q}$, is given as:

$$\boldsymbol{Q} = \boldsymbol{k} - \boldsymbol{k}_0 \tag{3.3}$$

Using Miller indices as described in section 2.1.1, Equation 3.2 can be written:

$$a_1 \cdot \boldsymbol{Q} = 2\pi h$$
$$a_2 \cdot \boldsymbol{Q} = 2\pi k \tag{3.4}$$
$$a_3 \cdot \boldsymbol{Q} = 2\pi l$$

In single crystal XRD, the sample is typically too thick to allow for transmission of X-rays through the full thickness of the sample. Instead, the incident X-ray are arranged to irradiate the sample at a particular angle to the lattice planes of interest: a special case of the Laue conditions, the so called Bragg condition [49]:

$$n\lambda = 2d_{hkl} \sin\theta_B \tag{3.5}$$

Here, d_{hkl} is the lattice plane distance and θ_B the incident and exit beam angle with respect to the lattice plane, also called the Bragg angle. A schematic view of the geometry required for the Bragg condition is shown in Figure 3.2a (blue waves). By measuring the angles at which the Bragg condition is satisfied and strong diffraction spots occur, it is possible to extract the crystal structure and the unit cell parameters of the crystal. When the Bragg condition is satisfied, the relationship between the scattering wave vector and the lattice plane distance is simple: $|\boldsymbol{Q}| = 2\pi/d_{hkl}$ [4].

When performing XRD on small crystals (a few micrometer in size or smaller, depending on the measurement geometry), the finite size of the crystal starts to influence the shape of the diffraction spot. Consider an incoming beam scattering against two planes at conditions slightly deviating from the Bragg condition, as in Figure 3.2a (red waves). The outgoing waves then do not perfectly overlap, and even if the interference between the waves is mainly constructive, it is not optimal. Increasing the number of planes contributing to the diffraction, the deviation from Bragg conditions that still gives some intensity for the outgoing wave decreases. Hence, the angular width of a diffraction spot is inversely proportional to the number of planes along the scattering vector $\boldsymbol{Q}$. For nanowires, this effect can be used to decouple the scattering signal from nanowires from that of any surface layer grown on the substrate. For a thin film, the broadening parallel to the substrate surface is typically limited by

---

[4] This relationship is sometimes written as $|\boldsymbol{Q}| = 1/d_{hkl}$, depending on how $\boldsymbol{k}$ is defined.
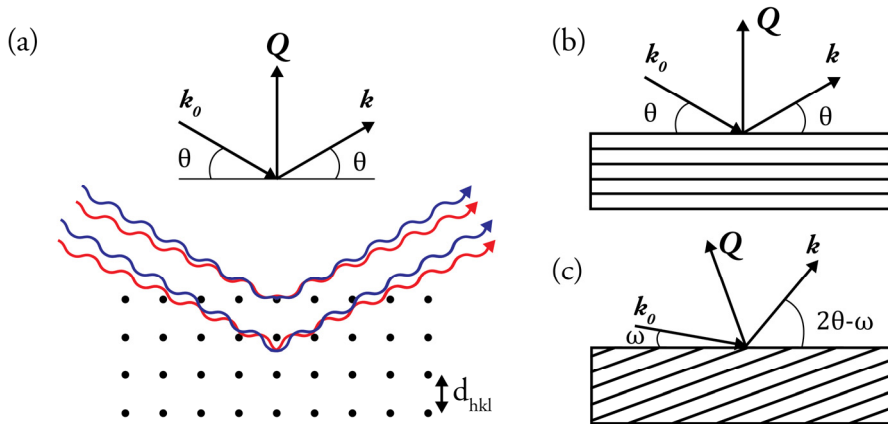
Figure 3.2. Incident X-ray beams diffracted from a crystalline sample. (a) shows the geometry for the Bragg condition. The blue waves are at the Bragg angle, but the red waves have a small deviation, and constructive interference for the exit waves is not optimal. A vector representation of the Bragg condition is also shown. (b) and (c) show symmetric and asymmetric measurement geometries respectively. In the asymmetric geometry, the angle between k_0 and substrate, ω, is smaller than the Bragg angle θ_B, and this geometry is called grazing incidence.

instrumental broadening, depending on the measurement setup, whereas the small radius of the nanowire causes a larger broadening. Measuring with an offset away from Bragg conditions, the substrate and surface layer signal is attenuated more strongly than the nanowire signal [50] (Paper xiii).

Another way to decouple substrate diffraction and diffraction from the nanowires is to use diffraction from planes which only exist in the nanowires. III-V nanowires are typically grown on $(\bar{1}\bar{1}\bar{1})$ substrates, in the $[\bar{1}\bar{1}\bar{1}]$ direction. Lattice plane spacings in the growth direction are measured in a symmetric XRD measurement geometry, where the incoming beam and the exit beam have the same angle with respect to the substrate surface. If instead an asymmetric geometry is used, as in Figure 3.2c, planes with an oblique angle to the substrate surface cause diffraction. In this way, diffraction spots from ZB material with a different twin direction from the substrate, and diffraction from WZ nanowires, can be well separated from the substrate spots.

3.2 Electron microscopy

When describing a microscope as simply as possible, three parts of the system are essential: an illumination source, a magnifying lens, and a detector (in the simplest case, the eye). In an optical microscope, visible light from a lamp or the sun is directed onto the sample, and a set of optical lenses collects the scattered light and focuses it into the

eye or camera. Assuming perfect lenses, the spatial resolution limit for an optical microscope is approximately given by the Rayleigh criterion [33]:

$$\delta = \frac{0.61\lambda}{\mu \sin \beta}$$

(3.6)

Here, δ is the smallest distance that can be resolved, λ is the wavelength of the light, μ is the refractive index of the viewing medium and β is the semi-angle of collection of the magnifying lens. The refractive index of the viewing medium and the magnifying lens properties together determine the numerical aperture of the microscope, which can be approximated to unity for a good microscope. Using green light with a wavelength of about 550 nm, to which the human eye is most sensitive, the resolution limit according to the Rayleigh criterion will be around 300 nm. To reduce the resolution limit, the wavelength of the illumination source has to be changed. By using electrons instead, the wavelength of the illumination source becomes related to the particle energy by de Broglie's equation:

$$\lambda = \frac{h}{p}$$

(3.7)

where h is Planck's constant and p the particle momentum. For an electron accelerated by an electric potential V (the acceleration voltage), the kinetic energy gained by the potential is $e*V$, where e is the elementary charge. The momentum of the electron can then be written as:

$$p = \sqrt{2m_0 eV}$$

(3.8)

where m_0 is the electron mass. At an acceleration potential of 10 kV, which is a common acceleration voltage on scanning electron microscopes, the electron wavelength is already below 0.1 nm, and at 300 kV, which is a common acceleration voltage on transmission electron microscopes, the electron wavelength is below 0.002 nm, if relativistic effects are accounted for. Clearly, using electrons for illumination, it is possible to improve the spatial resolution by as much as five orders of magnitude compared to an optical microscope.

Using electrons in a microscope instead of visible light requires electromagnetic lenses instead of optical ones. An electromagnetic lens is used to create an image of an object or to bring parallel beams to a focus. Similarly to optical lenses, electromagnetic lenses have defects such as spherical aberration, chromatic aberration and astigmatism, all of which limit the resolution of the microscope. Spherical aberration causes electrons further away from the center of the lens to be bent more strongly and brings them to a focus closer to the lens. The energy of the electrons will also determine how strongly they will be bent, which causes chromatic aberration. The electromagnetic lenses in an
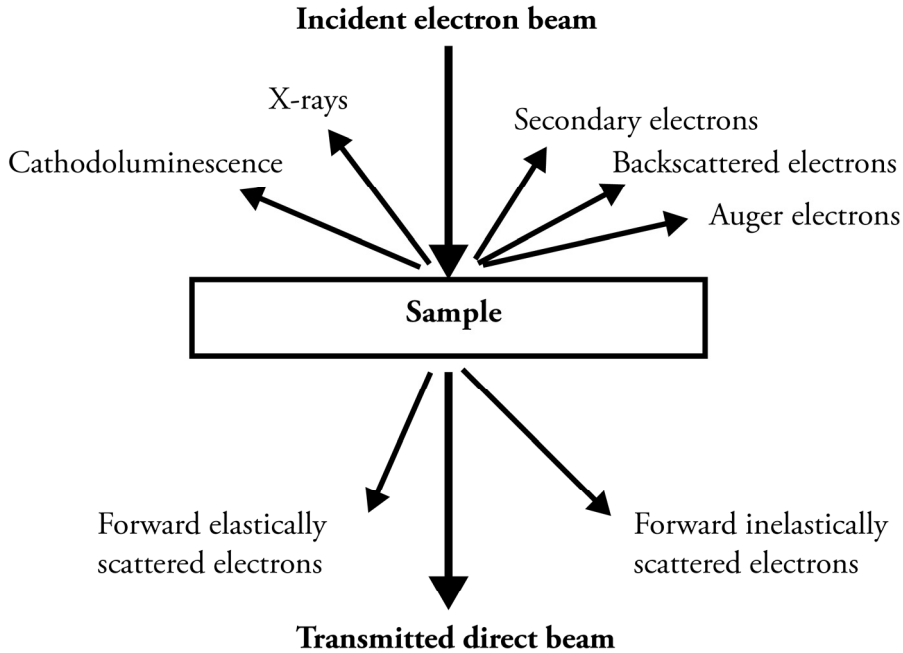
electron microscope are not perfectly cylindrically symmetric, which causes a non-uniform magnetic field. Such non-uniformity will give rise to astigmatism.

In most electron microscopes today, it is not the wavelength of the electrons that limits the resolution, it is the lenses. Electron microscopes are developing rapidly, and techniques to compensate for aberrations are constantly evolving. To reduce the effect of chromatic aberration, monochromators may be used [51] or the energy spread of the accelerated electrons may be improved by using a more stable acceleration voltage and electron gun. Cylindrical electromagnetic lenses are not perfectly symmetric, which can lead to an asymmetric probe. For twofold astigmatism, this causes a smearing of the image in one direction, but may be compensated for by stigmator coils. Positive spherical aberration is unavoidable in cylindrical electromagnetic lenses [52], which causes electrons further away from the optical axis to be bent more strongly than those close to the center of the lens. Inserted apertures can screen electrons far off axis, but won't compensate for the aberration. Instead, modern transmission electron microscopes can have corrector consisting of extra multipole lenses to compensate for spherical aberration in the cylindrical lenses. By allowing cylindrical lenses to work together with multipole lenses, the total spherical aberration may be tuned to either a small positive or negative value [53].

The electrons in a beam may interact with the sample in several different ways. Electrons that interact with the sample will either be elastically scattered or inelastically scattered, and depending on the type of interaction, it is possible to extract different information about the sample. Figure 3.3 summarizes some of the signals generated as an electron beam interacts with a sample. In a scanning electron microscope (SEM), secondary electrons (SE) and back-scattered electrons (BSE) are used for imaging, whereas in a transmission electron microscope (TEM), the transmitted direct beam and forward scattered electrons are used to create images. For analytical electron microscopy (AEM), other signals such as X-rays or photons generated by cathodoluminescence may be used.

Electron microscopes can generally be divided into different sections, some of which are common for both SEM and TEM. For an SEM, the two major sections are the *illumination system* and the *detection system*. For TEM, an *image formation system* and a *projection system* are added. As the *illumination system* is common for both SEM and TEM, it will be discussed here. The *detection system*, consisting of various electron or photon detectors will not be described here, but relevant details will be given in the following sections, depending on the imaging technique. The *image formation system* and *projection system* will be discussed separately in the section on TEM.

The purpose of the *illumination system* is to form either a parallel beam of electrons in conventional TEM mode, or a well focused, small probe in scanning TEM (STEM) mode, or in an SEM. The electrons used in the beam originate from an electron gun, mounted at the top of the microscope column. Two general types of electron guns are used in electron microscopes: either a thermionic gun, where a filament is heated until

Incident electron beam

X-rays

Cathodoluminescence

Secondary electrons

Backscattered electrons

Auger electrons

Sample

Forward elastically
scattered electrons

Forward inelastically
scattered electrons

Transmitted direct beam

Figure 3.3. Different types of signals generated when an electron beam meets the sample in an electron microscope. Depending on the microscopic or spectroscopic technique, different signals are recorded.

it emits electrons, or a field emission gun (FEG), where a strong electric field extracts electron from the tip of a filament. A heated FEG, a so called Schottky FEG, has a higher emission stability and higher operating pressure than a cold FEG, at the cost of a larger energy spread of the extracted electrons. Comparing the FEG to the thermionic gun, the FEG emits electrons from a much smaller area and with a much smaller spread in energy, resulting in much more coherent illumination, which is important for high resolution imaging. However, the thermionic sources are able to operate at pressures which are several orders of magnitude higher: a typical Schottky FEG requires operating pressures below 10^{-9} Torr, whereas a thermionic LaB_6 filament only requires pressures below 10^{-6} Torr.

Once the electrons are extracted from the filament, they are accelerated by the potential in the acceleration tube. The more accurate and more stable the acceleration voltage is, the better controlled is the velocity, and hence the wavelength, of the electrons. In a 300 kV TEM, the electrons are accelerated to about ¾ of the speed of light and have a relativistic wavelength of about 0.002 nm.

Because not all the electrons in the gun are emitted from the same point and at the same angle, the illumination system also contains an aperture, the condenser aperture,

to exclude electrons emitted at high angles. However, the use of a condenser aperture comes at the cost of a reduced beam current.

3.2.1 Scanning electron microscopy

In this thesis, the SEM is the tool most frequently used to characterize nanowires, and almost all samples grown are initially characterized using SEM. Luckily, modern SEMs are very user-friendly, with a highly intuitive user interface, and provide rapid and reproducible results. Sample preparation for a semiconductor sample is typically straightforward, and no more than a mechanically stable and electrically-conductive connection to the sample holder is necessary. As the name of the technique implies, the operating principle of the SEM is to focus the electron beam to a small probe and scan it across the sample. For each beam position, scattered or emitted electrons (or X-rays for analytical microscopy) are recorded and a digital image is formed where the brightness in each pixel is determined by the number of collected electrons. However, in order to interpret the images formed properly, knowledge of how the collected electrons are generated in the sample is essential. Both secondary electrons (SE) and back-scattered electrons (BSE) can be used to create images, which will result in different types of contrast.

In the SEM, the sample is usually thick enough that no electrons pass through, and all of the electrons in the incident beam will interact with the sample. As the electrons meet the sample, a fraction of these will interact inelastically and transfer some of their kinetic energy to the sample. If the energy is transferred to an electron in the outer shells of an atom, the excited electron may gain enough energy to overcome the work function of the material and be ejected. These ejected electrons are referred to as secondary electrons (SE). Electrons may also be ejected via the Auger process, where an excited ionized atom returns to its ground state. As the SE have very low kinetic energy (<~50 eV), they can only escape the material if they originate from close to the sample surface. The number of SE escaping the sample mainly depends on the angle between the incident beam and the sample surface: the smaller the angle between the surface and the beam, the more SE are ejected from the sample. To collect low energy SE, an electric field is used to attract them into a detector. Hence, SE ejected from surfaces tilted away from the detector may also be detected, and any surfaces with a tilt relative to the electron beam will appear brighter than those which are perpendicular to it. Similarly, small topographical variations may also increase the amount of SE that are able to escape from the sample surface, which makes it possible to detect roughness on an otherwise flat surface.

Inelastic scattering is not the only scattering process to consider in a SEM, electrons from the incident beam may also scatter elastically. In elastic scattering, no energy

transfer from the electron to the sample occurs during the scattering event[5]. As an electron passes through the electron clouds in an atom and comes closer to the positively-charged nucleus, an attractive Coulomb force will cause the electron to deflect towards the nucleus. This process is called Rutherford or Coulomb scattering. If the scattering is strong enough, the incident electron may be deflected back to where it came, and escape the sample. These elastically scattered electrons which escape the sample are called back scattered electrons (BSE). As the generation of BSE requires a strong Coulomb interaction, the charge of the nucleus is important. As a result, BSE may be used to create SEM images with Z-contrast – material with higher nuclear charge typically give more BSE. As the BSE have higher energy compared to the SE, they are able to escape the sample from much deeper within it, and from a larger volume, so the spatial resolution using BSE is lower compared to SE. As the BSE have energies comparable to the incident beam, no electric field can be used to direct the electrons to a detector, and only BSE ejected towards the detector will be captured. Depending on the detector geometry, it is possible to create images with strong topographic contrast, as BSE from surfaces tilted towards the detector will be more likely to be detected.

The spatial resolution in a SEM is governed by the beam probe size and the electron penetration depth. Both are influenced by the acceleration voltage of the microscope, and the penetration depth also depends on the sample material. For semiconductor nanowires, the penetration depth is similar for different III-V materials, and the spatial resolution depends more on the acceleration voltage. Generally, a high acceleration voltage increases the penetration depth, which decreases the signal to noise ratio for SE. On the other hand, higher acceleration voltages generally give better control of the beam probe size, which increases the spatial resolution. By choosing imaging conditions properly, a resolution of a few nanometers or better can be achieved on semiconductor samples.

3.2.2 Transmission electron microscopy

By making a sample thin enough, an electron beam with a high enough energy can pass straight through, with a low probability of inelastic scattering. By using the elastically scattered electrons that pass through the sample, it is possible to generate images, and this is the basis of a TEM. The probability for scattering in a thin sample decreases as the electron energy is increased. However, too high an electron energy can cause severe knock-on damage where the electrons displace atoms in the sample. The TEMs used in this thesis are a JEOL 3000F operating at a 300 kV acceleration voltage, and a

---

[5] The scattering is not fully elastic, since the Coulomb interaction between an electron and an atom could, for example, cause emission of bremsstrahlung X-rays. The distinction between inelastic and elastic is hence somewhat simplified here.
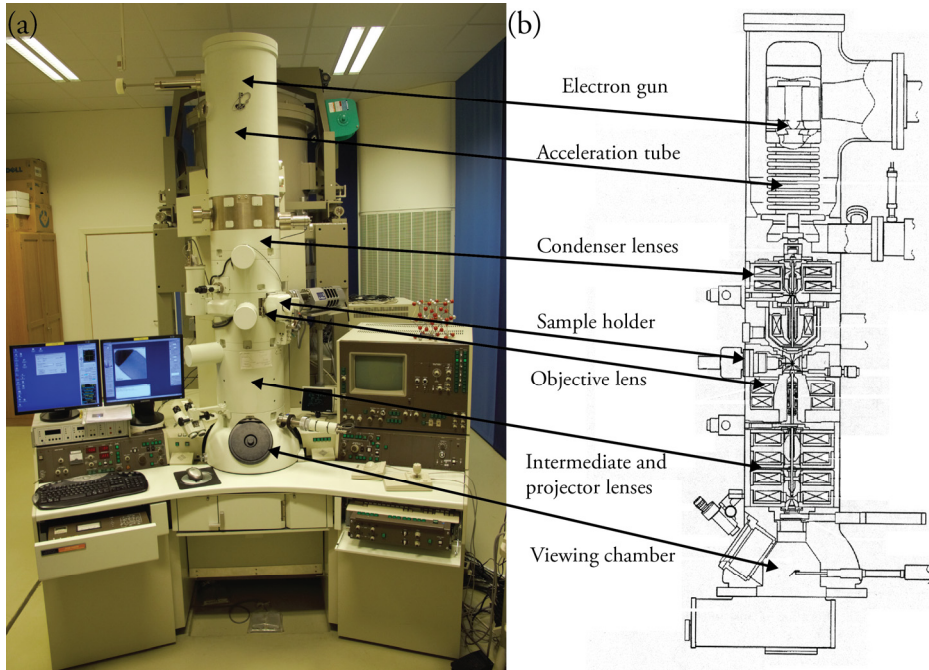
Figure 3.4. (a) The JEOL 3000F in Lund and (b) a schematic of the same microscope.

Hitachi H-9000 also operating at 300 kV. These are both medium voltage TEMs. As several imaging methods have been used, the TEM will be discussed in more detail than the SEM, so as to highlight the differences in these methods. If no other references are given, the explanation of different parts of the TEM are based on the excellent textbook by William and Carter [33].

Figure 3.4a displays a photograph of the JEOL 3000F microscope together with a schematic drawing of it. A TEM can generally be divided into four major sections: the *illumination system, image formation system, projection system* and *detection system*. The JEOL 3000F is capable of operating in both conventional TEM mode with a parallel, coherent, broad electron beam, and in scanning TEM (STEM) mode, where the beam is converged to form a small probe and scanned across the sample, similarly to in the SEM. When operating in STEM mode, the lenses in the projection system are in principle not necessary, but they are still used to change the effective camera length or to form an image of the electron probe. In the following sections, the TEM will first be described in general and then different imaging methods will be discussed.

The *illumination system*, consisting of the electron gun, acceleration tube and condenser lenses, is described in general above. The next part of the TEM is the *image formation system*, which consists of the objective lens and the sample. The objective lens is the strongest on the TEM and is placed as close as possible below the sample. In some cases, the sample is actually mounted between the upper and lower pole pieces of the objective

lens. The purpose of the objective lens is to capture the scattered electrons from the sample and bring them to a focus. Because the objective lens captures electrons at higher angles than following projector lenses, and because it is off axis electrons that are most severely affected by aberrations, the objective lens is regarded as the most important lens in the TEM. Below the objective lens, two sets of apertures are placed: the objective aperture and the selective area aperture. The objective aperture is placed in the back focal plane of the objective lens, where electrons scattered with the same angles from the sample are brought to a single focus, independently of where they originate in the sample. For a crystalline sample, the back focal plane contains the sample's diffraction pattern. The selective area aperture is placed in the conjugate image plane, which makes it possible to select electrons originating only from a part of the illuminated area.

In the last section of the TEM lens system, the *projection system*, projector lenses either magnify the back focal plane of the objective lens or its conjugate image plane onto a screen or an electron detector, the *detection system*. For quick viewing, a fluorescent screen is used, which may be removed to allow the electrons to strike a detector which converts the impinging electrons to a digital signal, for example a CCD. The contrast in the final TEM image will depend on how many electrons are collected at each pixel. To understand the contrast in the image, it is important to understand how electrons interact with the sample.

Images recorded in a TEM may be divided into two categories depending on the contrast of the background. If unscattered electrons are used to form an image, the background where the electrons pass only through the vacuum of the TEM will appear bright, and the imaging mode is called bright field imaging. If only scattered electrons are used, the background where no scattering occurs will appear dark, and the technique is called dark field imaging. Both types of imaging are used in TEM and in STEM.

Bright field TEM

To describe how contrast arises in TEM, it is easiest to think of the electrons as waves and it is the state of the transmitted electron wave after passing through the sample that determines the contrast. Contrast in the image arises if either the amplitude or the phase of the wave has been altered by scattering. Both amplitude and phase contrast may contribute simultaneously to the image, but generally one of them dominates. For low resolution TEM and STEM, amplitude contrast has the major contribution, whereas high resolution TEM (HRTEM) relies on phase contrast.

Amplitude contrast originates from either diffraction or mass-thickness variations in the sample. Mass-thickness contrast is the most intuitive contrast contribution: heavier and thicker areas of the sample have a higher probability of incoherently, elastically scattering electrons at high angles. These high angle electrons will either be lost in the column or excluded by the objective aperture. Areas with heavier and thicker segments will then appear darker in bright field images. Diffraction contrast, which will be discussed in more detail later, arises from coherent elastic scattering in crystalline

samples. Depending on the crystal structure and the sample orientation, the pattern of diffracted beams, i.e. the diffraction pattern, will be different and will have different intensities. By including electrons from specific diffracted beams to form the image, different crystal structures or orientations may be highlighted.

Phase contrast allows for high resolution imaging, but is also present in low resolution images. When an electron penetrates the electron shells around an atomic nucleus in the sample, it will feel an attractive force from the positive nucleus and be temporarily accelerated. The electron will have no net velocity change once it has completely passed the nucleus, as it will decelerate as it travels away from it. However, the changes in velocity will give the electron a different phase compared to the electrons passing the atom at a greater distance, for which the nucleus will be screened by the atom's electron clouds. Hence, every point *(x,y)* in the image plane will cause a phase change of the electron wave depending on the potential it sees while passing through the sample (assuming it is thin enough that this is the only interaction between the electrons and the sample). The image plane can be seen as a map of the atomic column positions, which can give the appearance of atomically resolved images. The map of atomic columns can be described as a function *f(x,y)*, the so-called sample function. However, the TEM is not capable of perfectly reproducing *f(x,y)* in the final image, as imperfections in the microscope will cause a smearing, resulting in every point in *(x,y)* being transformed into a disk. How a given point spreads to a disk can be described by a function *h(x,y)*, the point-spread function, and the final image can then be described as a convolution of *f(x,y)* and *h(x,y)*, such that *g(x,y)=f(x,y)⊗h(x,y)*. Because every point in *g(x,y)*, the image function, has contributions from several points in *f(x,y)*, the contrast in the final image is not always easy to interpret. The goal with high resolution TEM imaging is to create a function so that the contrast is still directly interpretable, typically the atomic columns will appear darker and the areas between them brighter.

To achieve high resolution images, a high spatial resolution is required. If we perform a Fourier transform on *g(x,y)*, this means that the high spatial frequencies need to be transferred correctly. Using ***u***, the reciprocal lattice vector, to describe the spatial frequency for a particular direction, the sample function, point spread function and image function may each be written as a separate Fourier transform – *F(**u**), H(**u**)* and *G(**u**)*. The three Fourier transforms are related by:

$$G(\boldsymbol{u}) = H(\boldsymbol{u})F(\boldsymbol{u}) \qquad (3.9)$$

*H(**u**)* tells us how contrast in reciprocal space is transferred to the image and is known as the contrast transfer function (CTF). The CTF depends on the microscope and its focus settings, and will have a maximum ***u*** at which phase information is transmitted in a directly interpretable way. For the JEOL 3000F, this point is at 6 nm^{-1} at optimum focus, which gives a maximum point resolution of 0.17 nm in the final image.

Diffraction and dark field TEM

In Chapter 3.1, the Laue conditions for constructive interference and the Bragg condition were introduced. The same basic concepts apply for electron diffraction in a TEM. To recap, Figure 3.5a shows diffraction from a set of planes with spacing *d*. The angle of the planes with respect to the incident beam, k_0, is set to fulfill the Bragg condition and give the diffraction spot G. This is also represented by the fact that the scattering vector Q goes from the origin O (unscattered beam) to G. Tilting the sample further to increase θ_B will eventually give the 2G diffraction spot instead.

The diffraction spots depicted in Figure 3.5a are a few of the reciprocal lattice points of the crystal. The full reciprocal lattice is a 3D array of points, but to simplify matters, the following discussion will be limited to 2D. Drawing the lattice points of the crystal together with the wave vectors for the incident beam and a diffracted beam, k, the so called Ewald sphere can be constructed, showing which lattice points will give diffraction, as in Figure 3.5b. The lattice points cut by the drawn circle, the Ewald sphere, are those which will be present in the diffraction pattern. The length of k_0 and k is given by $2\pi/\lambda$, where λ is the wavelength of the electrons. In Figure 3.5b, the diffraction conditions resulting in the black, solid Ewald sphere fulfill the Bragg condition for the diffraction spot marked G, and it can also be seen that the Ewald sphere cuts through G. Increasing the angle between the incident beam and the lattice plane, leads to the grey, dashed Ewald sphere, for which the Bragg condition is instead fulfilled for the 2G spot.

(a)   (b)

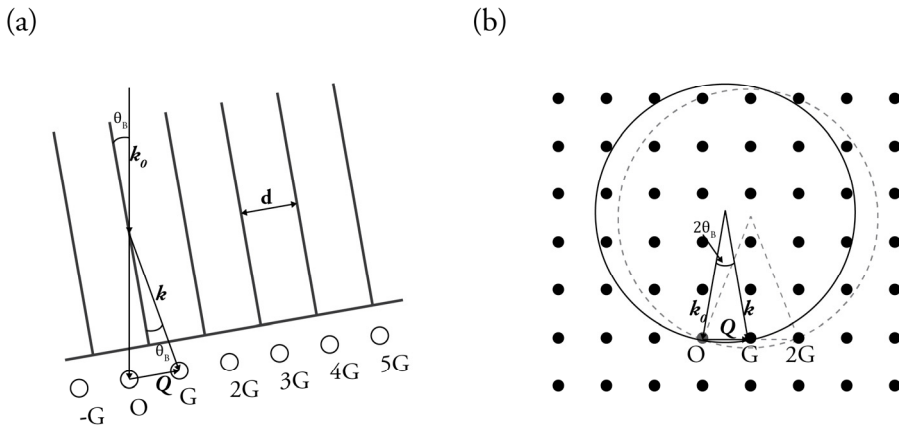Figure 3.5. (a) Diffraction from a set of a lattice planes. The angle between the lattice planes and the incident angle fulfills the Bragg condition for diffraction spot G. (b) A cubic 2D array of reciprocal lattice points with an Ewald sphere. Increasing the angle between the incident beam and the crystal plane, which also increases the angle between k_0 and k, moves the Ewald sphere, as illustrated with the grey, dashed lines.

The short wavelength of the electrons will result in a very large Ewald sphere, which will be almost flat around O. However, in an infinitely large crystal, the reciprocal lattice points will be just points, and the Ewald sphere has to cut perfectly through the reciprocal lattice point for constructive interference to occur. Luckily, as a TEM sample has to be very thin to be transparent to the electrons, and the finite size of the crystal will cause an elongation of the reciprocal lattice points. For a nanowire, which is limited in size in its radial direction, the reciprocal lattice points will be elongated in the corresponding direction as well. Hence, even if the incident beam is perfectly parallel to a lattice plane, and the Ewald sphere only perfectly cuts O, the Ewald sphere intersects with several elongated lattice points close to O. Figure 3.6a shows a schematic view of diffraction from a sample with k_0 parallel to a plane, and Figure 3.6b for the same sample with a slight offset in angle between the beam and the lattice planes. With a small angle between the incident beam and the lattice planes, a different set of elongated lattice points are cut by the Ewald sphere. Since the Ewald sphere also cuts the elongated reciprocal lattice points when the sample is not aligned with a zone axis, the tilt requirements are not as stringent as for high resolution imaging where phase contrast is used.

Diffraction patterns are very useful for identifying crystal type, orientation and lattice plane spacing. Once the diffraction pattern is known for a sample crystal and for a specific direction, the pattern can be used to tilt the sample to a specific zone axis, which is a requirement for high resolution imaging. When a sample has different crystal structures or orientations, the diffraction patterns are used to distinguish one from the
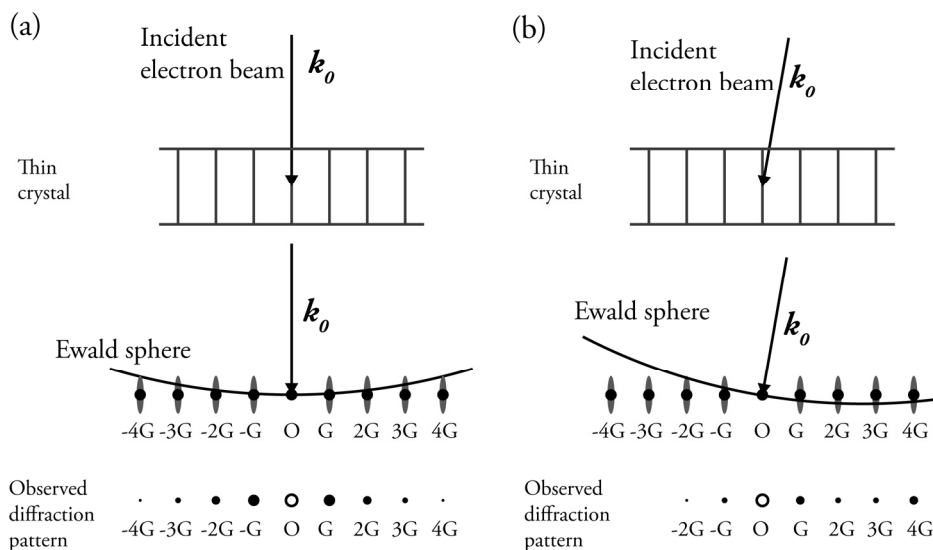
Figure 3.6. Diffraction from a thin sample. (a) with the incident beam parallel with the lattice planes of the crystal and (b) with a small angle between the incident beam and the lattice planes.

other. Using a selective area aperture in the conjugate image plane of the objective lens, diffraction patterns from selected parts of the illuminated sample can be recorded. Once the different crystal structures or orientations in a sample have been identified, different diffracted beams in the combined diffraction pattern can be used to image where in the sample specific selected crystal structures or orientations are to be found. Placing a small objective aperture in the back focal plane of the objective lens, it is possible to select only one or a few diffracted beams to form the image. Using only diffracted beams, dark field (DF) images are recorded, in which areas which diffract to the specific location of the objective aperture will appear bright in the image.

It is possible to achieve diffraction dark field conditions in two ways: either the objective aperture is mechanically moved from the central, undiffracted beam to a diffracted beam, or the incident beam is tilted so that the diffracted beam ends up at the aperture opening. Figure 3.7 shows ray diagrams and the position of the objective aperture in bright field and dark field imaging. As ZB and WZ have different diffraction patterns in some zone axes, it is possible to use dark field imaging to see where in a nanowire the different structures are located. Additionally, thicker samples than those for which high resolution imaging is possible give diffraction signals which may be used for dark field imaging. However, the spatial resolution is not as high, and in many cases high resolution imaging and dark field imaging are used to complement each other.
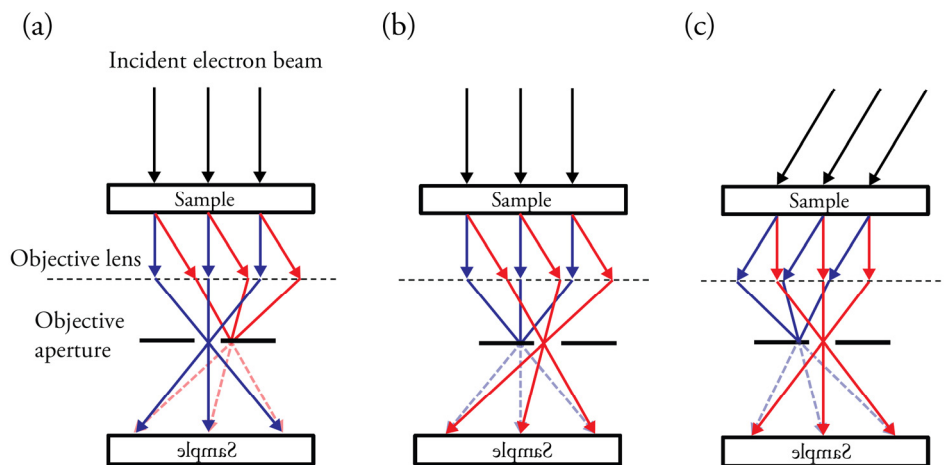
Figure 3.7. Ray diagram of the objective lens showing the position of the objective aperture during bright field imaging (a) and dark field imaging (b,c). Diffracted beams are colored red, direct beams are colored blue. In (b), dark field conditions are achieved by moving the objective aperture to select one diffraction spot while the direct beam is blocked. Dark field conditions may also be achieved by tilting the incident beam, as shown in (c).

Scanning TEM – STEM

In scanning TEM (STEM), the coherent, parallel TEM beam is condensed to form a small, incoherent probe and scanned across the sample, as in SEM. As with diffraction in TEM, the direct beam lies on the optic axis in the back focal plane of the objective lens, while scattered and diffracted beams which leave the sample at the same angle are collected at a single point in the back focal plane[6] independently of where in the sample they are created.

To create an image in STEM mode, the back focal plane of the objective lens is projected to different detectors, where the readout from the detector is coupled to the position of the scanning electron beam. Figure 3.8 shows a ray diagram of a convergent scanning beam, where the direct beam and scattered beams are captured with different detectors. BF STEM images are created using the direct beam, while DF STEM images result when using only scattered beams. The detector used in the all the work in this thesis was an annular dark field detector (ADF), a circle-shaped detector that captures all electrons scattered within a specific range of angles. For low angle scattering, contrast results from a combination of diffraction contrast and mass-thickness contrast, while the contribution from diffraction contrast decreases at higher angles. Using only
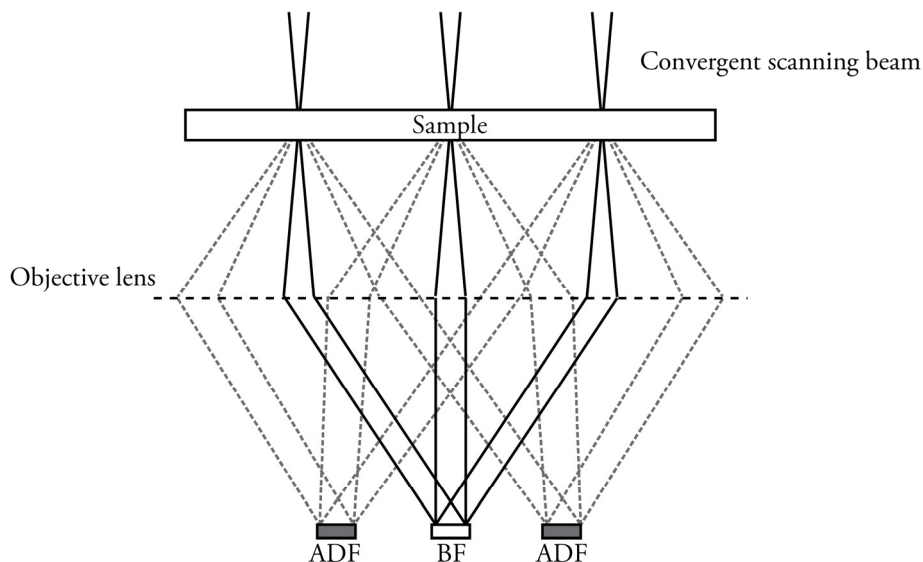
Figure 3.8. Ray diagram of a convergent scanning beam, where the direct beam and scattered beams are captured with different detectors.

---

[6] As the scanning beam converges to a spot, it is not parallel as in TEM, and so the diffraction spots are discs instead of well-defined points. The simplification is made for clarity.

electrons scattered to high angles, the imaging technique is typically called HAADF (high angle annular dark field). Scattering to high enough angles, typically above 50 mrad for 300 kV electrons, is dominated by incoherent diffuse scattering which depends primarily on sample thickness and mass. For a sample with the same composition, and hence constant Z, the HAADF signal has a linear relationship with the sample thickness for a wide range of thicknesses, which gives a direct correlation between the HAADF image contrast and the sample thickness. Similarly, the Z-contrast is possible to interpret straightforwardly: high Z gives high contrast.

X-ray energy dispersive spectroscopy – XEDS

Imaging in a TEM relies on elastic scattering of electrons in the sample. However, inelastic scattering of electrons is also used in several analytical methods in electron microscopy. Figure 3.3 above lists some of the signals generated as electrons interact with a sample. One of the most common analytical techniques uses the characteristic X-rays emitted from a sample, a technique known as X-ray energy dispersive spectroscopy (XEDS or EDS or EDX). If an incoming electron scatters inelastically and ejects a core electron, the excited atom may relax by allowing an electron from an outer shell fill the empty state. An X-ray photon is emitted in the process, with an energy corresponding to the difference between the energies of the two electron states involved. As different atoms have different electron configurations and electron energy levels, the energy of the emitted X-rays can be used to deduce which elements have been excited. Each element will have a set of intensity peaks in the XEDS spectra, where the energy of any peak is correlated to the two electron states involved in the X-ray photon generation.

For samples with several different atoms, the ratio of the intensities of X-ray peaks from different elements is proportional to their abundance in the sample. The exact relationship depends on the elements and the system, but can be calculated using the Cliff-Lorimer equation:

$$\frac{C_A}{C_B} = k_{AB}\frac{I_A}{I_B} \tag{3.10}$$

where C_x is the concentration of x and I_x the peak intensity, and k_{AB} is the Cliff-Lorimer factor, which depends on the elements A and B as well as the X-ray detection system, TEM acceleration voltage, and the sample thickness. Cliff-Lorimer factors may be determined experimentally or theoretically. For most elements, the typical minimum detectable fraction is about 0.5–1.0 at%. Combining XEDS with STEM, it is possible to create compositional maps with a spatial resolution of a few nanometers, depending on the beam size and beam broadening within the sample.

XEDS may be used in any electron microscope, whether SEM or TEM/STEM. For SEM and STEM, the use of a small scanning probe enables spatially resolved spectroscopy, and it is possible to record elemental maps. In TEM, where a broad beam

illuminates a large portion of the sample simultaneously, X-rays are generated from the whole illuminated portion. However, spreading the beam over a larger area does reduce the risk of damaging the sample during collection of X-rays for analysis.

In situ TEM

It is very appealing for a researcher working with epitaxy to be able to follow the growth of a crystal in real time, and observe its dynamics with high spatial and temporal resolution. *In situ* TEM offers one possibility to study the physical processes which control growth, such as by timing nucleation events or monitoring catalyst stability, but introducing gases and heating a sample inside a TEM imposes some challenges. For example, a TEM operates under high vacuum so as to reduce diffuse scattering from gas molecules and to limit deposition on the electron gun filament, which could otherwise cause it to break down. A MOVPE reactor typically operates at 100 mbar which is at least six orders of magnitude higher than the pressure in a typical TEM (for the gun chamber, the difference is typically at least eight orders of magnitude). Hence gas handling in a TEM has to be done with great care. To be able to introduce gases or liquids onto the sample in a TEM, two different methods can be employed: either using an environmental cell (E-cell), or differential pumping.

The use of E-cells was proposed and demonstrated as early as 1934 to study biological samples [54], where two Al foils were used as upper and lower windows to contain a suitable environment for a live biological sample situated between them. Since then, E-cells have been refined, and today's state-of-the art cells are capable of controlled gas flows at pressures up to a few bar with simultaneous heating, allowing for studies of catalytic reactions at atmospheric pressure while still achieving sub-nanometer resolution [55]. Simpler E-cells, constructed by sandwiching two SiN thin film TEM grids, are capable of allowing remarkable observations of nanowire growth [56]. E-cells also make it possible to study processes in liquids, but great care has to be taken over beam exposure as the irradiating electrons can potentially change the liquid solution [57].

A drawback to using E-cells is that two windows have to be used, which can limit the resolution. Also, heating may cause problems, as heating the sample can cause different thermal expansion for different parts of the cell, leading to cracks and leakage. For *in situ* studies with a solid sample and gases, the gases may instead be introduced directly at the sample stage, as close as possible to the sample. By using restrictive apertures above and below the sample together with a differential pumping system, it is possible to achieve a pressure difference of several orders of magnitude between the sample and, most importantly, the gun. The pressure difference depends on the size of the restrictive apertures and the pumping capabilities of the TEM.

For the *in situ* TEM studies performed in this thesis, a modified Hitachi H-9000 ultra-high vacuum TEM has been used [58]. The TEM was originally designed for ultra-high vacuum studies, and is capable of reaching a base pressure of $\sim 2 \times 10^{-10}$ Torr. By

using the differential pumping system of the microscope, a local pressure of $\sim 10^{-5}$ Torr at the sample can be maintained while the electron beam is turned on. The precursor gases are injected into the microscope via a capillary tube, which ends a few millimeters above the heated sample, as is shown in Figure 3.9. In the experiments here, trimethylgallium (TMGa) and arsine (AsH_3) are used, which are typical precursor gases for MOVPE growth of GaAs. The precursor gas pressures are much lower than those typically used in MOVPE, and no H_2 carrier gas is used, which gives lower growth rates and a different decomposition chemistry. However, the lower growth rates facilitates more accurate measurements of kinetics. The spatial resolution of the H-9000 microscope does not allow for atomically-resolved images, but instead diffraction dark field imaging is used to differentiate between different crystal structures. This way, it is possible to study the growth of polytypic GaAs nanowires with high enough temporal and spatial resolution to observe the growth of single bilayers.
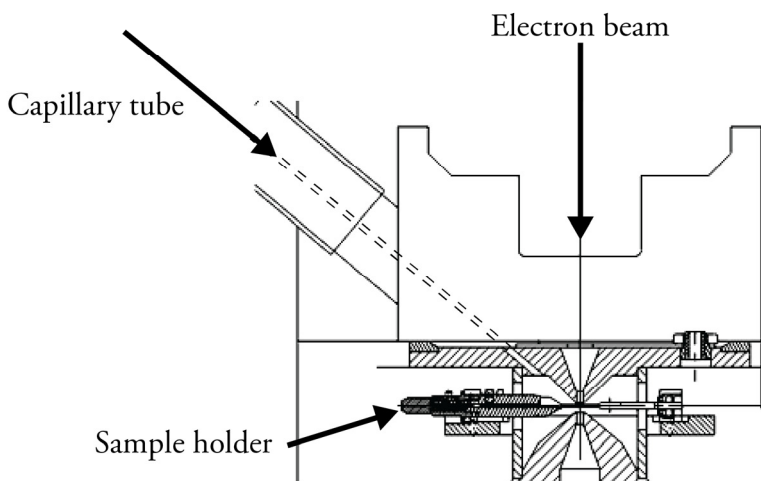

Figure 3.9. The pole piece region of the H-9000 *in situ* TEM with the sample holder and the capillary tube for precursor gases. The capillary tube ends a few millimeters above the sample, which is resistively heated. Adopted from [59] with permission.

3.3 Photoluminescence

One intrinsic property of a semiconductor crystal is its band gap, the smallest distance between the valence band, which is filled with electrons, and the conduction band, which is empty (at T=0 K). The bandstructure depends on structure of the periodic crystal, and changing either the constituent atoms or their arrangement will lead to changes in the bandstructure. One method to probe the properties of the bandstructure is photoluminescence, where a laser is used to excite electrons from the valence band to the conduction band. Typically, the excitation laser has a higher energy than the band gap of the semiconductor, and electrons are excited high up into the conduction band. The excited electrons lose energy via phonon scattering, and relax to the lowest available state in the conduction band. From here, they recombine with holes in the valence band, and the photon emitted may be measured, as is shown in Figure 3.10a.

In a defect-free structure, recombination will happen across the band gap, but if defects are introduced, they will break the symmetry of the crystal and can introduce new electronic states within the band gap. If such defect states are involved in the recombination process, photons with energy lower than the band gap are emitted, as shown in the example in Figure 3.10b.

The recombination process involves transfer from an occupied state in the conduction band to an empty state in the valence band, and is possible to influence the degree of occupation of the states in the conduction band by the intensity of the excitation laser. For high laser intensity, the excitation rate is higher than the recombination rate between the lowest energy states in the conduction band and the highest unoccupied states in the valence band. As a result, more and more states in the conduction band are filled, and excited electrons at higher energy states begin to recombine with holes in the valence band, as in Figure 3.10c. The state filling effect pushes the average energy
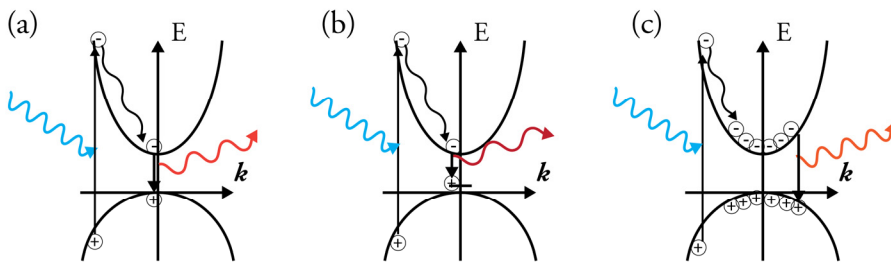
Figure 3.10. A schematic of photoluminescence, with excitation due to light irradiation, followed by recombination and photon emission. (a) shows band-to-band recombination, and (b) shows band-to-defect recombination. At high excitation powers, state filling may occur, which blue-shifts the emission energy, as shown in (c).

of the emitted photons to higher energies, an effect known as the Burstein-Moss shift [60, 61].

In heterostructures, the conduction band or the valence band of the two materials might not be at the same energy level. A thin slice of a material whose conduction band has a lower energy than to the surrounding material can create a quantum well where electrons may be confined. The confinement of the electrons raises the energy of the lowest allowed state by an amount which depends on the material and shape of the well. For a well of finite depth, the electron wavefunctions are able to penetrate into the surrounding barriers, resulting in a probability, while low, of finding an electron in the surrounding barrier close to the quantum well. An interesting effect of the penetration of the wavefunction into the surrounding barrier is that recombination is possible from a state in the quantum well to the valence band of the barrier material. As it appears that the electron and hole which recombine in this case originate from different spatial parts of the structure, this process is called spatially indirect recombination, and it can be analyzed to extract information about the band alignment of heterostructures.

In this thesis, photoluminescence studies are carried out to measure the band gap of WZ and ZB GaAs nanowires, as well as the band alignment between the two crystal structures. To estimate the band alignment, a spatially indirect recombination was studied with varying excitation laser intensity, which caused state-filling close to the WZ-ZB interface.

4 Growth of polytypic nanowires

The history of growing semiconducting nanowires goes back to around 1957, when Si and Ge "whiskers" were successfully grown as a part of a survey of the growth direction of different metal whiskers [62]. The research originated from trying to understand metallic wire-like structures which spontaneously formed between a metal mounting plate and a capacitor, causing short circuits in frequency band filters for telephones [63]. For the semiconducting whiskers, it was first proposed that growth was driven by a screw dislocation, but in 1964, Wagner and Ellis proposed that Si whiskers could be grown from a liquid alloy, in a vapor-liquid-solid (VLS) mechanism [64]. The proposed mechanism was based on a detailed study of Si whisker growth, where an "impurity" was essential for mediating the growth, and not a screw dislocation. It was already foreseen at this time that "*controlled growth can be obtained through appropriate use of impurities in patterns or films on substrate surfaces and on single-crystal seeds of many substances*", which is in line with the focus of nanowire research today. The name "impurity" has now been replaced with 'seed particle', and similarly, "whisker" is now most commonly "wire". It was suggested that suitable seed particles need not be limited to foreign metal particles, but that for compound semiconductors such as GaAs, one of the components could form the liquid seed. In 1965, Barns and Ellis showed that GaAs wires could be grown from Au, Pd, Pt and Ga seed particles [65]. Today, fifty years after the initial work on VLS by Ellis and co-workers, research is still being carried out on the properties of the seed particle, and the impact it has on the growth of nanowires.

4.1 Fundamental nanowire growth principles

To grow a crystal in the form of a nanowire, extremely anisotropic growth has to be promoted. For free-standing III-V semiconductor nanowires, this can be done in three different ways: (1) by the use of a seed particle made of a foreign material; (2) by forming a droplet of one of the constituent parts, which is also called self-seeded; and (3) by using a growth template to promote growth in one crystallographic direction. Using MOVPE, all three of these have been achieved. When using a foreign material seed particle, Au is the most common [66], but other metals such as Fe [67], Cu [68], Pd [69], and Sn have been demonstrated. For self-seeding, In droplets may be used, for example, for InP [70], or Ga droplets for GaAs [71]. By tuning the growth conditions,

it is possible to promote growth in one crystallographic direction only, and by using a mask with only small openings onto the substrate, nanowires can be grown without any seed droplet on top, a method sometime referred to as selective area (SA) growth [72]. All nanowire growth discussed in this thesis has been performed using Au seed particles, and the following chapters will be focused on the VLS-mechanism. When growing GaAs using Au seed particles, Ga alloys readily with the Au, while the solubility of As is very low.

The growth of a crystal relies on a phase transition from the supply phase to the solid phase, where the driving force is provided by the difference in chemical potential between the two. For growth of planar structures in MOVPE, the difference in chemical potential promoting layer growth, here written as $\Delta\mu_{v-s}$, is that between the vapor phase, μ_v, and the solid phase, μ_s. Recalling the thermodynamics discussed in Chapter 2, the difference in chemical potential can be written as (see Equation 2.16):

$$\Delta\mu_{v-s} = \mu_v - \mu_s = k_B T \; ln\left(\frac{p}{p_v}\right) \qquad (3.1)$$

Introducing a seed particle to promote nanowire growth, the axial growth of the nanowire will be driven by the chemical potential difference, $\Delta\mu_{l-s}$, between that of the seed droplet, μ_l, and the solid, μ_s. The difference in chemical potential between the liquid seed and nanowire can be expressed as:

$$\Delta\mu_{l-s} = \mu_l - \mu_s = k_B T \; ln\left(\frac{c}{c_0}\right) \qquad (3.2)$$

where c is the adatom concentration in the seed droplet and c_0 its equilibrium concentration. For nanowire growth, the droplet has to be supersaturated, which ensures that $c/c_0 > 1$ during growth and $\Delta\mu_{l-s}$ is positive.

During steady-state growth of the nanowire, the adatom concentration in the seed particle does not change as the net arrival rate of adatoms from the vapor phase equals the incorporation rate into the solid at the seed particle-nanowire interface. In this regime the following relationship holds: $\Delta\mu_{v-s} = \Delta\mu_{v-l} + \Delta\mu_{l-s}$, where $\Delta\mu_{v-l}$ is the difference in chemical potential between the vapor and the seed particle [73]. As $\Delta\mu_{l-s}$ has to be positive for growth and $\Delta\mu_{v-l}$ must be positive for supply of adatoms from the vapor to the seed particle, steady state growth implies that $\Delta\mu_{v-s} > \Delta\mu_{l-s}$. If $\Delta\mu_{l-s}$ is negative, the seed particle would start to etch the nanowire, and if $\Delta\mu_{v-l}$ is negative, atoms will diffuse out of the seed particle into its surroundings.

Interestingly, if we only look at the supersaturation, it appears that a seed particle should not promote nanowire growth over substrate growth, because $\Delta\mu_{v-s} > \Delta\mu_{l-s}$. However, if kinetics is taken into account it can be seen that the seed particle is able to

increase the growth rate of the nanowires substantially. The explanation starts by assuming that the nucleation rate follows an Arrhenius expression:

$$k_{nuc} = v_{nuc} e^{-\Delta G^*/k_B T} \qquad (3.3)$$

Here, ΔG^* is the Gibbs free energy at the critical nucleus size (see Equation 2.17), and the prefactor v_{nuc} depends on the adatom concentration, the rate at which adatoms attach to the nuclei, and the Zeldovich factor [74]. Assuming a similar prefactor for nucleation at the substrate surface from the vapor and nucleation at the seed particle-nanowire interface, a higher growth rate for the nanowire can only be achieved if ΔG^* for a nucleus at the seed particle-nanowire interface is smaller than that for a nucleus on the bare substrate. The only factor remaining that could achieve this is the surface energies of the different nuclei.

To compare the differences between nuclei on a bare substrate and at a seed particle-nanowire interface, consider the two different positions for a nucleus shown in Figure 4.1a, labeled A and B, respectively. As a first approximation, assume that the nuclei have the same crystal structure and composition as the substrate and nanowire so that the structure of the top facet of a nucleus is the same as the surface present before it was formed. In this case, the only additional surfaces formed during nucleation are the side facets of the nucleus. For a nucleus on the bare substrate, the surface energies of those facets are given by $\gamma_{v\text{-}s}$, which for the following example will be considered to be independent of the type of facet (which is a simplification, as will be discussed further in the next chapter). For a nucleus at the seed particle-nanowire interface, with side facets only exposed to the seed particle, the surface energies are given by $\gamma_{l\text{-}s}$, which in

(a)   (b)
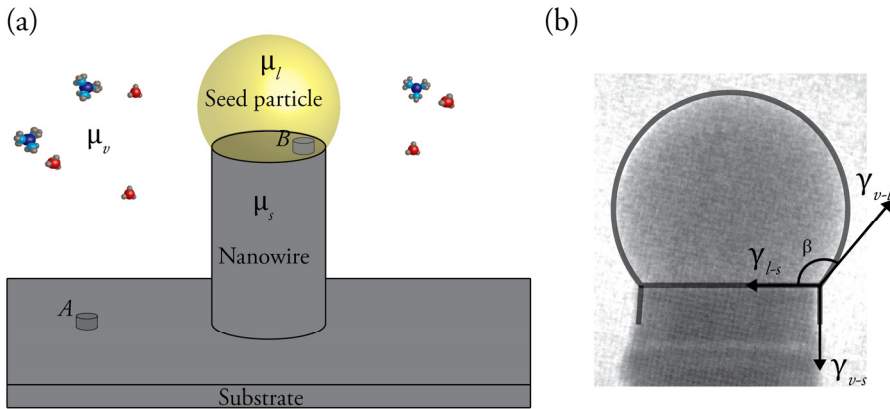
Figure 4.1. (a) Schematic of a growing nanowire, with a nucleus on the bare substrate, A, and at the nanowire-seed particle interface, B. (b) Surface energies at the triple phase line for a GaAs nanowire during growth.

the following example will also assumed to be facet-independent. In addition to the surface energies of the different nuclei, the seed particle surface energy, γ_{v-l}, is also important, as will be seen in the following example.

As an example, consider the case of Au-seeded GaAs nanowires. For GaAs, γ_{v-s} has been calculated and measured to be between 1.27–2.2 J/m^2, depending on the facet [75]. For Au-seeded GaAs, the seed particle will mainly be an alloy between Au and Ga, for which the surface energies are 1.15 J/m^2 and 0.7 J/m^2, respectively [76]. To a first approximation, γ_{v-l} will in that case be somewhere in-between, depending on the Au-Ga composition. The last surface energy, γ_{Ls}, is not known, but may be estimated using Young's equation [77]. In Figure 4.1b, a nanowire imaged during growth shows the typical wetting angle of the liquid Au-Ga seed particle. The horizontal components of the surface forces acting on the point where the solid seed particle meets the wire are balanced if [78-80]:

$$\gamma_{l-s} = -\gamma_{v-l}\cos(\beta) \qquad (3.4)$$

For equation 4.4, it is assumed that the seed droplet only wets the top facet of the nanowire and does not de-pin to wet the nanowire side facet during growth. Moreover, the wetting angle should be higher than 90° (the Nebol'sin-Shchetinin criterion for stable nanowire growth [78]).

Typical wetting angles for steady state growth of nanowires during growth in the *in situ* experiments carried out in Paper IV were 100–130°, which gives $\gamma_{Ls} < \gamma_{v-l}$. It is worth noting that Young's equation is valid at equilibrium, whereas growth only occurs when equilibrium is not established. However, the low growth rates observed in the *in situ* experiments suggest only low supersaturations, and these systems are close to equilibrium.

Assuming that the seed particle is close to equilibrium with the vapor phase ($\Delta\mu_{v-s} \approx \Delta\mu_{v-l}$) and $\Delta\mu_{v-l} = 300$ meV per III-V pair, which is reasonable for typical Au-seeded GaAs growth [81], and that the wetting angle is 130°, it is possible to estimate the change in Gibbs free energy for a 2D nucleus (one bilayer high) for nuclei on the bare substrate and at the seed particle-nanowire interface, as is shown in Figure 4.2. Since surface energies are the only difference between a nucleus on a bare surface and one on a growing nanowire, the lower facet energy for the nucleus at the seed particle-nanowire interface reduces ΔG^*. As a consequence, the rate of nucleation at the nanowire will be much higher than on the bare substrate, and the fact that the nanowire grows is a consequence of the kinetics of the system. However, the differences in $\Delta\mu_{v-s}$ and $\Delta\mu_{v-l}$ depend on the growth conditions, and it is possible to alter the differences in ΔG^* so that $\Delta G^*_{surf} < \Delta G^*_{NW}$ and substrate growth is promoted instead. This typically occurs when the growth temperature is increased, which causes, among other effects, a higher decomposition rate of the precursor, increasing the vapor supersaturation (neglecting the effect of increasing equilibrium vapor pressure). An increase in the vapor
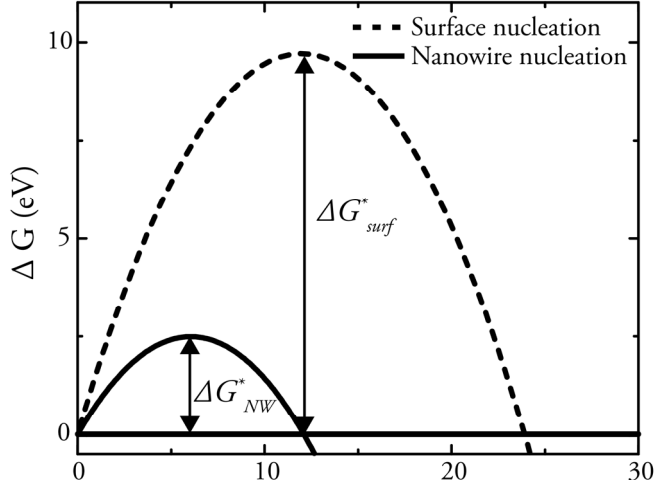
Figure 4.2. The change in Gibbs free energy for nuclei at the bare surface and at the seed particle-nanowire interface. A difference in chemical potential of 300meV was used, together with surface energies of $\gamma_{v\text{-}s}$=1.27J/m² and $\gamma_{l\text{-}s}$=1J/m². Wetting angle of 130° was used to calculate $\gamma_{v\text{-}l}$.

supersaturation may also lead to an increased supersaturation in the seed particle due to an increased concentration of adatoms. However, if the temperature-dependent solubility parameters for the constituents of the seed particle are taken into account, an increase in temperature decreases the supersaturation at a fixed adatom concentration [81].

4.2 Nucleation and growth at the liquid-solid interface

4.2.1 Nucleus position

In a growing nanowire, forming the ZB crystal structure in the $[\bar{1}\bar{1}\bar{1}]$ direction differs from forming the WZ structure in the $[000.\bar{1}]$ direction only in the lateral position of the new nucleus with respect to the second-nearest bilayer in the solid (see Chapter 2.1.). To understand where the preferred sites for nucleation are located at the seed particle-nanowire interface, the geometry at different possible nucleation sites and the surface energies of different possible nuclei have to be analyzed in detail. Models used to explain polytypism in both MOVPE and MBE-grown nanowires are most often based on the same conceptual idea: that the interface energies related to the formation of a new nucleus determine if it is a ZB or a WZ nucleus. Many such models are based on the one outlined by Glas et al. [28]. In principle, if WZ facets can be formed with lower surface energies than ZB, a lower nucleation barrier for WZ may exist, even if it
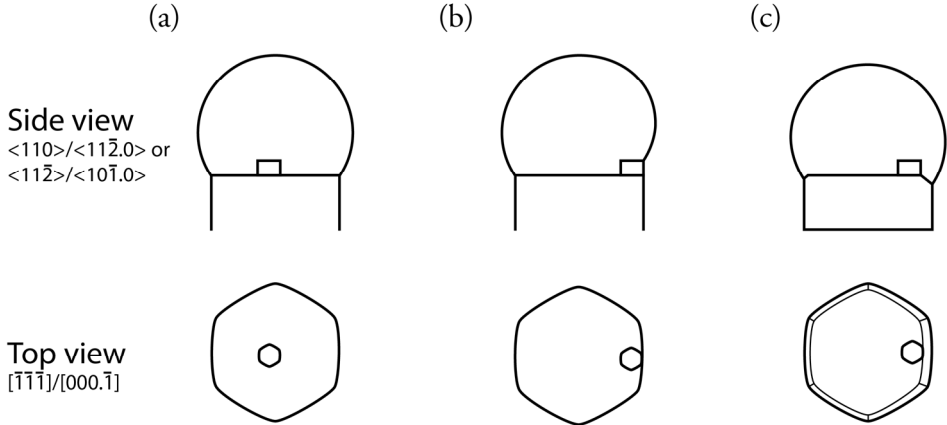
Figure 4.3. Different possible nucleus locations. In (a), the new nucleus forms at a position on the flat top facet, completely surrounded by the liquid seed particle. In (b) nucleation is at the triple phase line, and part of the nucleus is exposed to the vapor. With a truncated morphology of the nanowire top facet, nucleation may occur in contact with a truncated facet, as in (c).

is not the most stable phase. Several extensions to the model have been made, where the effects of dopants [80, 82, 83], the inclination of the nucleus side facet[19], relative droplet size [84], and the surfactant effects of Group V species [85] (Paper xii) have been taken into account.

Nucleation at the seed particle-nanowire interface can occur either at a central position, where the nucleus is completely surrounded by the seed particle on a homogeneous, flat facet; or at the triple phase line between nanowire, seed particle and vapor, which results in a part of the nucleus being exposed to the vapor; or on the top facet, but where it meets a truncated facet, also surrounded completely with the seed particle. These possibilities are illustrated in Figure 4.3. The position at which nucleation occurs has consequences for the change it induces in the total surface energy. For all three positions, the nucleus could either be of ZB or WZ type, according to the position of the new bilayer with respect to its second-nearest bilayer.

For the central position, as illustrated in Figure 4.3a, the lateral surface energies of the nucleus are independent of its position. However, for GaAs the difference in cohesive energy for WZ and ZB stacking, calculated as 24 meV per III-V pair [86], results in a lower difference in chemical potential between a WZ nucleus and the seed particle, and we can write: $\Delta\mu_{l\text{-}s}^{WZ} = \mu_l - (\mu_s^{ZB} + \Phi) = \Delta\mu_{l\text{-}s}^{ZB} - \Phi$, where Φ is the difference in cohesive energy. As a result, the nucleation barrier for WZ at a central position will always be higher than for ZB.

At the triple phase line, as illustrated in Figure 4.3b, a part of the nucleus is exposed to the vapor, which makes the expression for the surface energies of the new nucleus more complicated. A fraction, x, of the nucleus which is exposed to the vapor will now have

a surface energy depending on the type of side facet formed. As the nucleus forms at the triple phase line, a part of the liquid-vapor interface is also removed, and the change in Gibbs free energy for 2D nucleation at the triple phase line can be written, with A as the nucleus area, h as its height and P its perimeter length, as:

$$\Delta G = -\Delta\mu_{l-s}\frac{Ah}{V_{mn}} + Ph[(1-x)\gamma_{l-s} + x(\gamma_{v-s} - \sin(\beta)\gamma_{v-l})] \qquad (4.5)$$

By removing a part of the vapor-liquid interface, the energy cost of replacing a part of the liquid-solid interface with a more costly vapor-solid interface could be compensated for. Hence, nucleation at the triple phase line could in many cases be favored over central nucleation. In addition, nucleation at the triple phase line could explain the growth of WZ if facet-dependent surface energies are taken into account [28]. Comparing semi-equivalent low index facets of WZ and ZB, WZ has, in general, lower surface energies than ZB [75], and so nucleation at the triple phase line could favor WZ. However, surface energies are dependent on the surface chemistry, and it is possible for surface reconstructions to change which phase is favored. In addition, the vapor-liquid interface energy also has to be considered. A decrease of the vapor-liquid interface energy due to the surfactant effect of Group V species has been suggested as promoting ZB formation [85] (Paper xii). Also, dopants could alter the surface energies to promote either ZB [80, 82] or WZ [83].

For nucleation to occur at the triple phase line, at least some part of the top facet of the nanowire has to be in contact with the vapor. However, experimental observations of growing nanowires using *in situ* TEM has revealed that this might not be the case, as the top facet could be faceted with an oscillating behavior during growth [29, 31]. With truncation of the top facet, nucleation where the top facet meets the truncated facet will be favored, as illustrated in Figure 4.3c. Extending the truncated facet must have lower energy than introducing a new step, otherwise the truncated facet would break up into steps [31]. Similarly to nucleation at the triple phase line, WZ and ZB nuclei will now be different as they have different relationships to the truncated facet, which may change their surface energy. However, detailed modeling of WZ and ZB nuclei at a truncated facet is still lacking for Au-seeded nanowires. Attempts to implement possible nucleation at a truncated facet have been made for Ga-seeded GaAs [87].

4.2.2 Crystal structure dependency on local V/III ratio

Great efforts have been made to understand the effect growth parameters have on the crystal structure of III-V nanowires. For MOVPE-grown InAs nanowires, extensive work has been carried out to map out the crystal structure dependency on the precursor flow ratio (the V/III ratio), total precursor flow, the temperature, and the seed particle size [20]. For GaAs, less extensive studies had been made prior to the work in this thesis, but growth of defect-free ZB [85, 88] had been demonstrated using low a growth

temperature. For MOVPE-grown GaAs, it had also been shown that increasing the growth temperature and decreasing the V/III precursor ratio would favor a WZ crystal structure, a common feature with InAs [19]. However, reports have been published on Au-assisted GaAs nanowire growth using a different growth technique, molecular beam epitaxy (MBE) showing ZB at a low V/III ratio and WZ at a high V/III ratio [25-27]. To be able to model the polytypic behavior, it would be preferable to study a simple system with as few parameters as possible. Another complication is that it is the conditions at the growth front that are of interest, but these are only indirectly changed when the real input parameters, such as temperature and gas flows to the growth system, are adjusted. In the following discussions, the focus lies on the effective V/III ratio, which means the local ratio between Group V and Group III adatoms at the growing nanowire. The V/III ratio of the input gases is not necessarily replicated at the growing nanowire, as will be discussed later.

To examine the effects on the crystal structure of GaAs nanowires caused by changing the effective V/III ratio, a single temperature for growth of both crystal phases is preferred. In Paper I, an approach to growing both high crystal quality WZ and ZB was developed, using MOVPE with AsH_3 and TMGa as precursors. Based on ref. [19], where the WZ fraction in GaAs was found to increase with increasing growth temperature and decreasing V/III ratio, we further optimized the conditions for WZ growth, and were able to produce WZ with less than twenty stacking defects per micrometer of length. Increasing AsH_3 by a factor of at least 20, but keeping TMGa and temperature constant, changed the preferred grown structure to ZB. Interestingly, the increase in AsH_3 decreased the growth rate by roughly a half. Assuming Ga-limited growth for the ZB structure, the decrease in the nanowire axial growth rate can be explained by a decrease in the Ga migration length with increasing AsH_3 due to a higher incorporation rate on the nanowire side facets, and hence a lower Ga arrival rate at the seed particle. The assumption that ZB growth is Ga-limited is justified by the observation that turning off the TMGa first before cooling in AsH_3 after growth of a pure WZ nanowire, forms a ZB top segment on the WZ nanowire (Paper II). The ZB is formed by the excess Ga stored in the seed particle, and as the Ga chemical potential drops, the structure changes to ZB.

Ex situ analyses of the last section grown on the nanowire and the seed particle have to be performed with care, as the seed particle may lose material while cooling. In particular, it may lose the more volatile Group V element, as well as gain material from adsorbed species on the surface diffusing to the seed particle. However, by comparing different sets of samples which have been cooled in the same fashion, it is possible to deduce important trends, even though the observations are not quantitative measurements of the actual state of the particle during growth. Figure 4.4 shows TEM images of the top of WZ and ZB nanowires grown at the same temperature and cooled in AsH_3/H_2 and H_2 only, showing a ZB "neck" region for the WZ nanowires cooled in AsH_3/H_2. For cooling in H_2 only, WZ is found all the way to the seed particle. Using
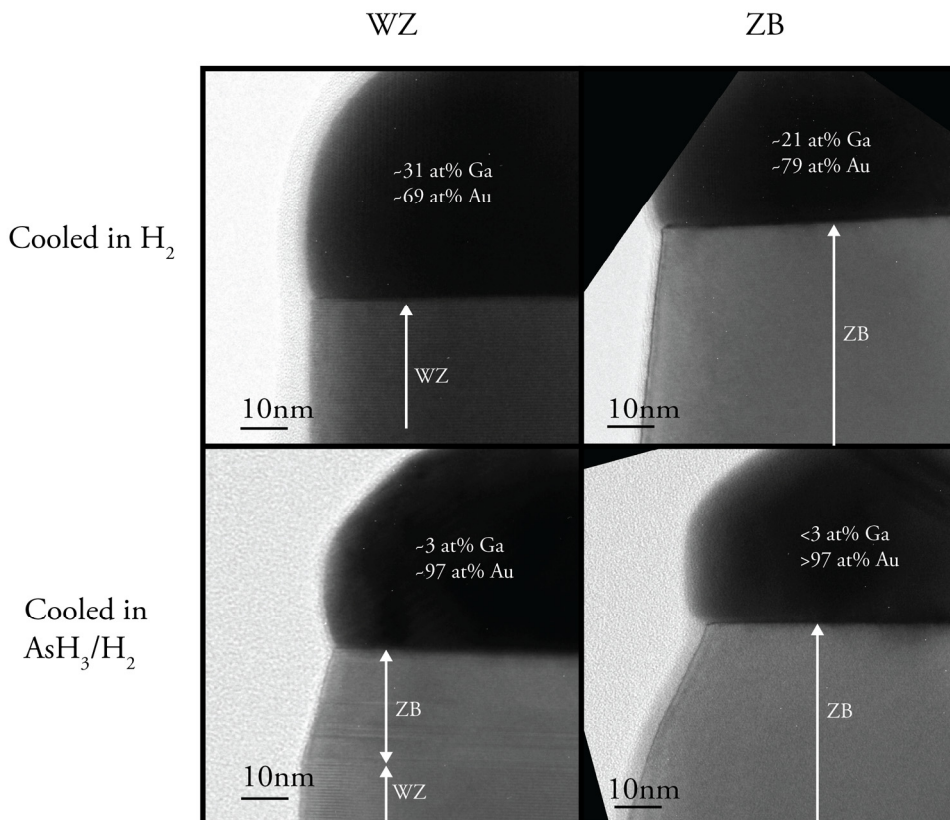
Figure 4.4. TEM images of GaAs nanowire top segments for different cooling procedures. Cooling in only H_2 keeps the initial crystal structure all the way to the seed particle. During cooldown with an AsH_3/H_2 mixture, a ZB neck region is formed on WZ nanowires. Composition of the different seed particles is measured by XEDS, the results are given in atomic percent.

XEDS, the composition of the different seed particles was measured, indicating a higher Ga content for the WZ nanowires.

If using a high AsH_3 flow causes Ga-limited growth, it seems obvious to ask whether the same switch to ZB can be achieved by reducing the Ga concentration. Reducing TMGa significantly from WZ growth conditions did indeed result in a change to ZB (Paper III). Using HCl, the same change to ZB is found, because of chlorination of Ga species which then leave the reactor chamber without contributing to growth. In conclusion, the WZ to ZB switch observed in papers I, II and III is due to an increase in the effective V/III ratio at the seed particle, which may be caused either by increasing the Group V precursor flow, or decreasing – or chlorination of – the Group III precursor.

To understand the switch from WZ to ZB with increasing effective V/III ratio in terms of current models of nucleation, consider nucleation at the triple phase line. For WZ to be grown, the surface energy of the WZ facet has to be significantly lower than the ZB, and the vapor-liquid surface energy should be low enough to compensate for the higher vapor-solid surface energy compared to the liquid-solid. The possible facets of a ZB nucleus exposed to the vapor have surface energies which decrease with higher As coverage [35], whereas the case for WZ is unknown. An increased As coverage could also act as a surfactant at the seed particle surface, lowering the vapor-liquid surface energy [85]. Decreasing the difference in γ_{v-s}^{WZ} and γ_{v-s}^{ZB}, and decreasing γ_{v-l} both give a higher probability to form ZB, and both can occur in an As-rich environment.

Interestingly, the WZ to ZB switch with increasing V/III ratio in the Au-seeded MOVPE-grown nanowires is not observed in Au-seeded MBE-grown nanowires [26, 28, 89, 90], and neither is it seen for Ga-seeded MBE-grown nanowires [25, 91] grown at similar temperatures, where an increasing V/III ratio typically promotes WZ. For the MBE results, one could argue that the As-rich environment for ZB growth in MOVPE has not been reached in the high-vacuum MBE chambers, where the As desorption rate is too high. In the case of Ga-seeded nanowires, reaching a Ga-limited growth regime would result in a diminishing Ga seed droplet, and the nanowires would eventually stop growing. The growth of ZB at low V/III ratio in the MBE systems has been speculated as being caused by a change in nucleation position, where the low V/III ratio, and hence high Ga content in the Au-Ga seed particle, results in nucleation at a central position rather than at the triple phase line [25, 92]. Arguably, a similar growth regime should also be possible to achieve in MOVPE, if the V/III ratio is decreased sufficiently. Indeed, if the V/III ratio is decreased even further below the value used for WZ GaAs growth in MOVPE, an increase in seed particle volume can be observed, as a result of the higher Ga content. Eventually, this decrease in the V/III ratio, and increase in the Ga content in the seed particle, also increases the ZB content in Au-seeded MOVPE grown nanowires. Some results suggest that that it would be possible to achieve a similar As-limited growth regime to that observed in MBE in MOVPE as well (unpublished results).

4.2.3 Seed particle dynamics – *in situ* TEM studies

Using only *ex situ* characterization to deduce the parameters governing the crystal structure has its limitations, for example, because of the changes in the seed particle during cooling discussed above. If possible, time-resolved *in situ* observations of growing nanowires should provide a more precise picture of the processes involved. So far, *in situ* TEM studies on Si, Ge and GaP have revealed remarkable results [31, 93], showing that the nanowire-seed particle interface does not have to be flat, but may have a truncated facet. Moreover, in Group V rich conditions, introduction of twin defects could increase the growth rate for III-V nanowires. In Paper IV, we used a modified

Hitachi H-9000 ultra high vacuum TEM (see Chapter 3.2.2), which allows for study of the growth of each bilayer in the nanowire, to study the growth of WZ and ZB GaAs nanowires. By using the periodic changes in the morphology of the seed particle-nanowire interface to time nucleation of each new bilayer (see Chapter 4.2.4), the local growth rate of the nanowire can be measured with high precision.

Using a similar growth temperature to that used in MOVPE for WZ-ZB structures – 550°C – it was possible to grow WZ and ZB in the *in situ* TEM, with a switch between the two crystal structures triggered by changes in V/III ratio. However, the structural trend was similar to that reported when using MBE, where a low V/III ratio results in ZB and a high V/III ratio in WZ. Keeping the TMGa flow constant, a stepwise change in AsH_3 resulted in slow changes in the Au-Ga seed particle size. In Figure 4.5, the seed particle height divided by the nanowire diameter at the growth interface (the h/d ratio) is plotted versus time for different AsH_3 flows. Overlaid on the h/d ratio (black line) is an indication of when ZB layer nucleation (red) and confirmed WZ growth (blue) occur.

After an AsH_3 decrease, the seed particle initially increases in size as the Ga arrival rate is faster than Ga incorporation into the nanowire. As the temperature is well above the melting temperature of Au-Ga alloys for any Au-Ga alloys with more than ~10at.% Ga, the liquid droplet has no thermodynamic limitation on how much Ga it can collect [94]. Hence, as long as the Ga arrival rate is larger than the incorporation rate into the nanowire, the Ga content in the seed particle will increase, and so will its volume. However, we found that within a certain V/III range, the h/d ratio of the nanowire stabilizes (a steady-state h/d ratio), where a low V/III ratio gives a larger seed
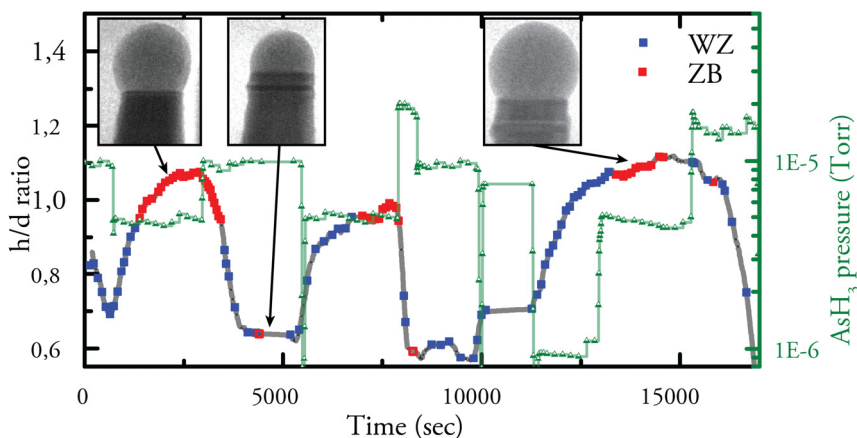

Figure 4.5. Seed particle height relative to the nanowire diameter, the h/d ratio, during *in situ* TEM growth of a GaAs nanowire. Changing the AsH_3 pressure (green), changes the seed particle volume, which triggering a switch in crystal structure between WZ (blue) and ZB (red). The red squares mark the occurrence of truncated corner oscillation and nucleation of a new ZB bilayer.

droplet. At too low a V/III ratio, the seed droplet grows uncontrollably and eventually falls off the top facet and wets the side of the nanowire, leading to kinked growth. At high V/III ratios the growth should reach a Ga-limited growth regime, a regime not accessible during these experiments because of limitations on the maximum AsH_3 pressure and difficulties with stabilizing the TMGa at very low flow rates.

The steady-state h/d ratio for different V/III ratios could be explained either by a difference in the Ga chemical potential in the seed particle, or a change in Ga incorporation into the nanowire for different h/d ratios. To understand the first explanation, consider increasing the Ga chemical potential in the seed particle while holding the vapor Ga chemical potential constant. An increased Ga chemical potential in the seed particle would decrease the Ga supersaturation between the seed particle and its surroundings, decreasing the driving force for diffusion to the seed particle. Such an explanation could be plausible for Au-Ga seed particles where the Au fraction is significant. However, for close to pure Ga droplets, changing the Ga volume would only change the Ga fraction by a negligible amount, and the Ga chemical potential would be unaffected. It would be necessary to study a nanowire with the same steady-state h/d ratio at different Au-Ga compositions to better understand the effect of the Ga chemical potential on the steady-state h/d ratio. It is possible to achieve an increase in the nanowire diameter at the seed particle interface by promoting radial overgrowth close to the seed particle. To maintain the steady-state h/d ratio of the seed particle, its Ga content increases. For the third cycle with a large h/d ratio for the nanowire in Figure 4.5, the nanowire width has been increased, and hence the droplet is highly Ga rich. Still, a steady-state h/d ratio is achieved at a similar V/III ratio to earlier cycles, with lower Ga content. Hence, the steady-state h/d ratio is not dependent on the Ga chemical potential.

Increasing Ga incorporation into the nanowire would also imply a higher As incorporation, and hence a higher growth rate. By timing the nucleation of each new bilayer in a ZB segment as the AsH_3 flow is changed, it is found that the growth rate depends both on the seed particle size and the AsH_3 flow, see Figure 4.6. The AsH_3 pressure change is much faster than the change in seed particle volume, and as the seed particle volume decreases, so does the growth rate. The As collection rate, to which the growth rate is proportional, can be written as:

$$As\ collection\ rate \propto \frac{\int_{t_1}^{t_2} P_{As}(t) * A_d(t)dt}{t_2 - t_1} \tag{4.6}$$

Where $P_{As}(t)$ is the AsH_3 pressure and $A_d(t)$ is the seed particle surface area. As $A_d(t)$ is inversely proportional to P_{As} at steady-state, an increase in AsH_3 pressure will give an initially high growth rate that will slowly decrease as size of the seed particle decreases. An increase in AsH_3 may also trigger a structural change from ZB to WZ, which
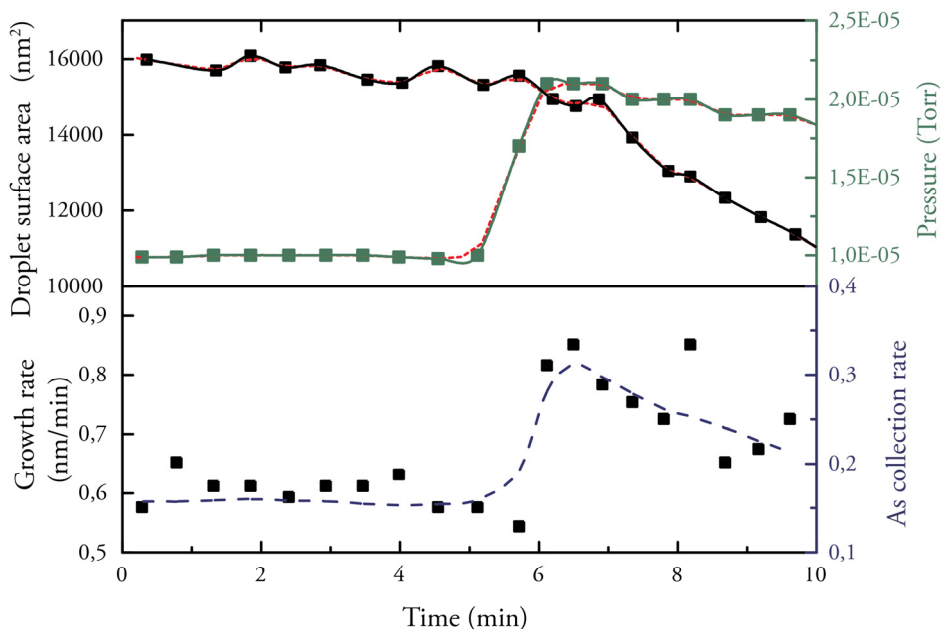
Figure 4.6. Local growth rate dependency on seed droplet surface area. The upper panel shows the seed droplet surface area (black) and the AsH₃ pressure (green). With an increased AsH₃ pressure, the seed droplet decreases in size. The lower panel shows the local growth rate of the GaAs nanowire, based on the ZB corner oscillation (black). The blue line shows the As collection rate according to Equation 4.6.

together with the transient droplet volume could explain the higher formation rate of WZ in transient conditions reported by Krogstrup et al. [91].

To summarize the crystal structure dependency on effective V/III ratio, three growth regimes are found for the MOVPE and *in situ* TEM grown nanowires. For the highest V/III ratio, an As-rich environment results in ZB, a regime only accessible using MOVPE. Reducing the V/III ratio and leaving the As-rich regime causes a change in crystal structure to WZ, and a growth regime common for both MOVPE and *in situ* TEM growth is reached. In this regime, the seed particle volume and nanowire growth rate depend on both precursor flows, where the ratio between the two determines the size of the seed particle. Reducing the V/III ratio even further, the seed particle increases in size due to its increased Ga content, which also triggers another change in crystal structure from WZ to ZB. Here, the growth regime common for MOVPE and the *in situ* TEM studies behaves in a similar way to that reported for MBE-grown Au-seeded GaAs nanowires. In all three regimes, it is possible to grow the relevant polytype with very high crystalline quality and very low stacking defect density. In between the conditions that produce pure crystal structures, nanowires with a much higher defect density are to be expected. Figure 4.7 summarizes the crystal structure dependency on
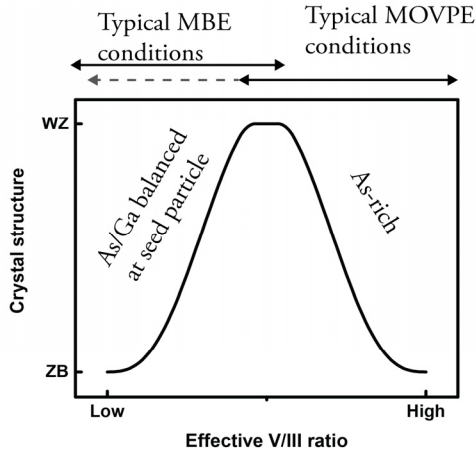
Figure 4.7. Effect on the crystal structure of Au-seeded GaAs nanowires at 550°C with different effective V/III ratios. Typical MBE and MOVPE growth conditions are marked with solid arrows, but MOVPE growth conditions can be extended to overlap with the MBE conditions to a larger extent (dashed grey line).

the effective V/III ratio for Au-seeded GaAs nanowires at growth temperatures around 550°C.

4.2.4 After nucleation - completion of the new bilayer

Once a nucleus has formed at the seed particle-nanowire interface, it is generally assumed that the growth proceeds as a fast step-flow growth across the top facet [28, 87, 95, 96]. Between each successive bilayer, the supersaturation of the seed particle has to increase until a critical supersaturation is reached to allow for a new nucleus to form (so that the nucleation barrier, ΔG^*, is lowered sufficiently, recall Equation 2.17). During the step-flow growth of the new bilayer, the supersaturation is assumed to be lower than the critical supersaturation for nucleation of a new bilayer, as the energy barrier for incorporation at a step site is negligible. Hence, a new nucleus cannot form until the previous bilayer is complete, and the growth proceeds in a mononuclear regime [28, 30, 31, 95-98]. The mononuclear regime is valid if the newly formed bilayer removes a substantial amount of material from the seed particle, which requires a relatively large number of atoms in the bilayer volume compared to the number of adatoms in the seed particle. This effect is specific to nano-sized systems, and even more prominent in systems with low solubility of one of the adatoms in the seed particle, for example, As in Au-Ga seed particles. In addition, the diffusivity of adatoms has to be high in the seed particle to achieve a homogeneous adatom concentration. For comparison, it has been observed that with solid seed particles where the adatom diffusivity is low, a new nucleus can form before the previous step-flow has

Particle refill, Δt_r	Nucleation, Δt_n	Step flow growth, depletion of seed particle, Δt_g	Particle refill, Δt_r	Nucleation, Δt_n
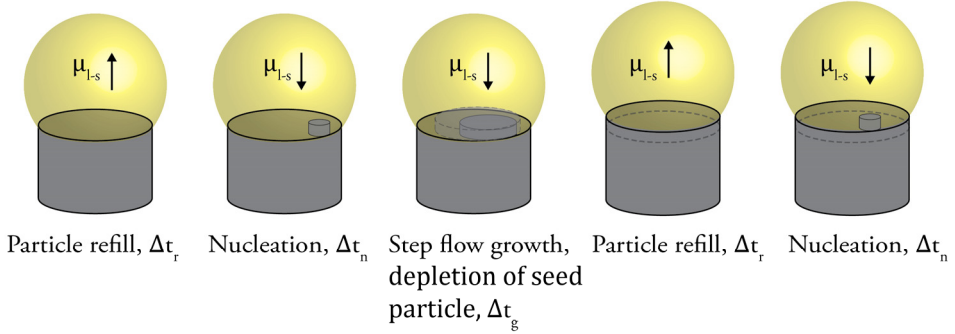
Figure 4.8. Illustration of the slow refill of the seed particle, nucleation and fast step flow growth, following the time hierarchy in Equation 4.7.

finished [99]. In principle, if the supersaturation is high enough that a new nucleation does not significantly change the adatom concentration, or if the seed particle is large enough to allow for significant concentration gradients within itself, polynucleation may occur. However, this will not be considered here as these conditions are unlikely for the growth regimes studied in this thesis.

In the mononuclear regime where a fast step-flow after a nucleation is followed by a slow refill of adatoms into the seed particle, nucleation events are temporally anticorrelated, which results in very narrow length distributions for the nanowires [95, 96]. As long as the seed particle is refilling with adatoms after completion of a step-flow, the probability of a new nucleation is virtually zero, as $\Delta\mu_{l-s}$ is below the critical value for nucleation, $\Delta\mu_{l-s}^*$. Once the supersaturation is increased enough so that $\Delta\mu_{l-s} \approx \Delta\mu_{l-s}^*$, the probability for nucleation of a new layer increases, which then happens stochastically within a characteristic timespan, Δt_n [96]. With a fast step-flow growth, completed in Δt_g, and a long refill time, Δt_r, the following timescale hierarchy holds for anticorrelated nucleation events:

$$\Delta t_g \ll 2\Delta t_n \ll \Delta t_r \tag{4.7}$$

For these inequalities to hold, enough adatoms to complete the bilayer should be available in the seed particle, and a nucleation event should take place much faster than the time required for refill. Fast nucleation and growth of the new bilayer, along with slow refill, leads to a sawtooth time evolution of the supersaturation in the seed particle. The sequence of events for a nucleation at the triple phase line or at central position with completion of the bilayer and subsequent refill of the particle is shown schematically in Figure 4.8.

For nanowire growth with timescales as in Equation 4.7, the rate limiting step for growth is the refill time. It has been argued that this is not the case for nucleation at a

truncated facet [31]. Vapor-liquid-solid growth of nanowires with a truncated facet has been correlated with an oscillating mass transport in several material systems such as sapphire [29], Ge [30, 31], and Si and GaP [31]. In Paper IV, we also found similar behavior for ZB GaAs. With a truncated facet, the morphology of the seed particle-nanowire periodically changes. Between each successive nucleation on the nanowire top facet, the size of the truncated facet decreases. Once a nucleation occurs on the top facet, the size of the truncated facet rapidly increases. Figure 4.9 shows the time evolution of the truncated facet of a GaAs ZB nanowire from the *in situ* TEM studies in Paper IV.

To understand why the truncated facet oscillates, the free energy of the extra facet should be analyzed. In the model proposed in ref. [31], the free energy ΔG_f of the truncated facet can be written as:

$$\Delta G_f = c_1 yL + \frac{1}{2\tan(\theta)} y^2 L \Delta\mu_{l-s} + c_2 y^2 L \qquad (4.8)$$

Here, y is the height of the truncated facet, L its width, and θ the angle it makes with the top facet. The linear term with coefficient c_1 reflects the capillary forces acting on the edge facet (the change in surface energies with facet size y). For $c_1>0$, the truncated
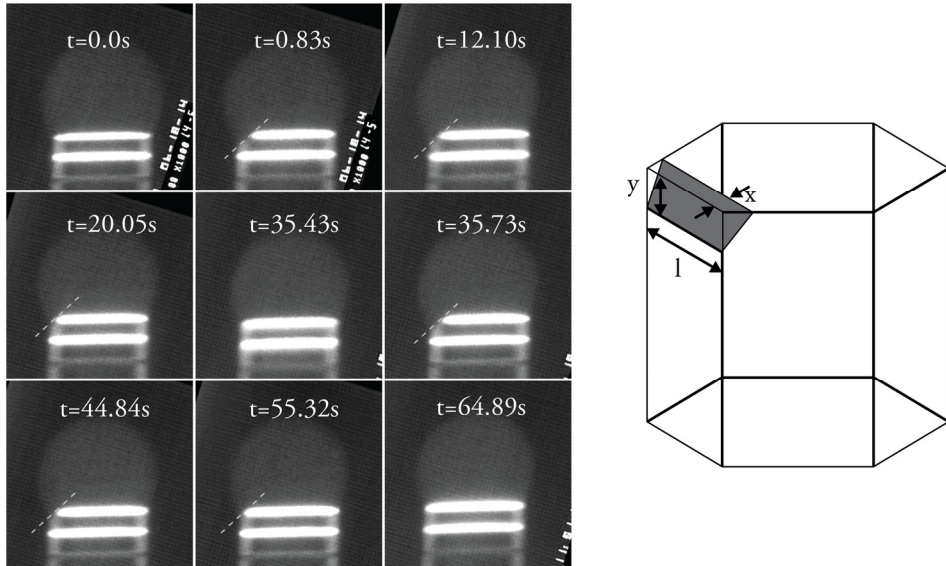

Figure 4.9. Truncated facet during growth of a ZB GaAs nanowire. On nucleation of a new ZB bilayer in the axial direction, a corner at the top facet is dissolved. Before the next nucleation in the axial direction, the truncated corner is regrown. The diagram shows the geometry of the truncated corner used in Equation 4.8, with $y = x \tan\theta$.

facet is unstable and will shrink and disappear. However, for a crystal in a fluid, $c_1 < 0$ for any facet present in the equilibrium crystal shape [100], and a truncated facet is expected to be present at equilibrium.

The quadratic terms in Equation 4.8 determine the size to which the truncated facet will grow when $c_1 < 0$. The first term depends on the supersaturation, and shows that the truncated facet will be smaller for higher supersaturations. Hence the size of the truncated facet can be used as a relative measure of the supersaturation, given that the surface energies do not change. For steady-state growth with a truncated facet, the oscillating size of the truncated facet has a direct relationship with the supersaturation and will have a sawtooth-like time dependency. The time hierarchy is similar to that of Equation 4.5 but Δt_r is replaced with Δt_f, where Δt_f is the time required for grow the truncated facet to its minimum size.

As a nucleation on the top facet happens with a truncated facet geometry, the truncated facet also increases its size. A plausible chain of events could be that as nucleation on the top facet takes place, the nucleus continues to grow in a step-flow fashion, which rapidly decreases the supersaturation. With the lower supersaturation, the truncated facet is too small to minimize ΔG_f. As a result, material at the truncated facet is dissolved to increase the size of the facet, and the released adatoms are used to complete the growing top layer. It is indeed the case that the volume removed at the truncated facet when nucleation takes place at the top facet is comparable the volume needed to complete one bilayer on the top facet.

The ZB GaAs grown with the *in situ* TEM in Paper IV clearly showed an oscillating facet at the triple phase line, but the WZ phase grew in a different way. For particular diffraction conditions, no oscillating facet was observed, and instead, a slow moving step propagates across the top facet. Slow step-flow has been observed in nanowire growth with solid particles [101, 102], but to date has not been reported for liquid seed particles. Figure 4.10 shows a time series of two step flow events across the top facet of a GaAs nanowire during WZ growth.

In the liquid seed particle, there is an excess of Ga, and As kinetics control the growth rate of the WZ step. Assuming a high diffusivity of As in the liquid seed particle, excess As in the particle can readily diffuse to the growing step. Once the excess As is depleted, the step cannot grow until more As is supplied to the droplet. Without any truncation of a facet as in the case for ZB, the remaining part of the WZ step will grow at the same rate as As arrives at the seed particle. As a result, the timescale hierarchy for the WZ case will be:

$$2\Delta t_n \ll \Delta t_g \qquad (0.9)$$

Nucleation events are still anticorrelated, because $\Delta\mu_{l-s}$ cannot increase to $\Delta\mu_{l-s}^*$ until the step is complete. Being able to measure the propagation rate of the WZ step
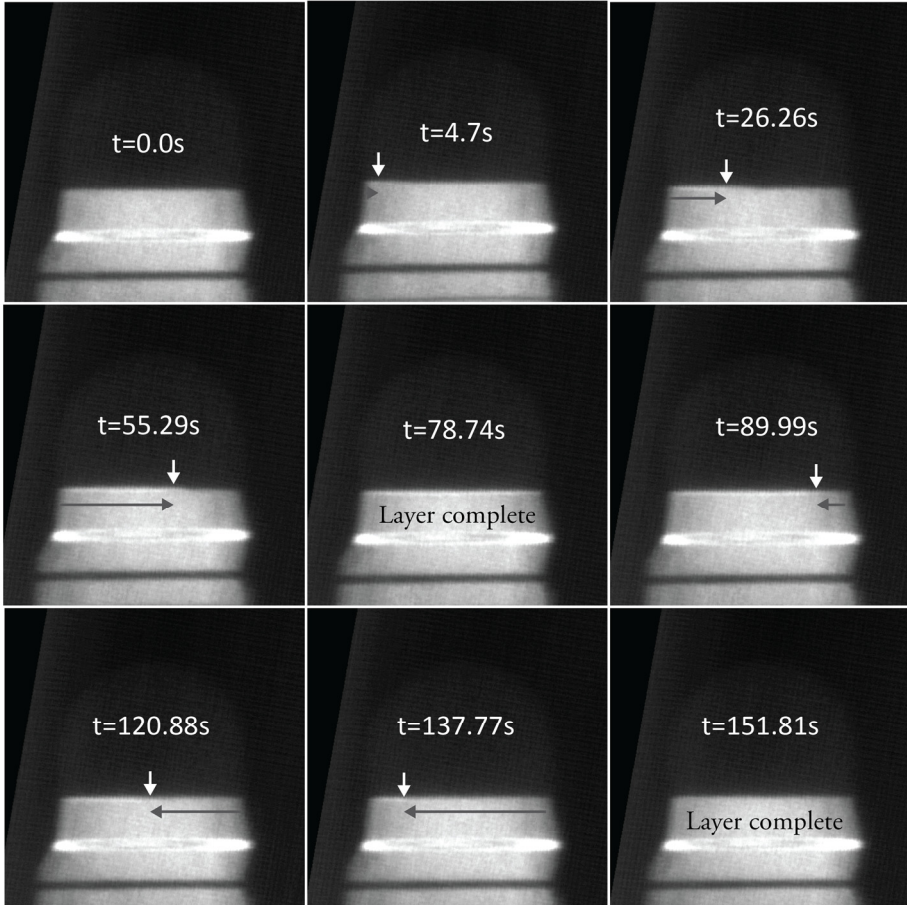
Figure 4.10. Growth of WZ GaAs proceeding as a slow step flow across the top facet of the nanowire.

accurately would give insight into the As arrival rate, which could also give information on the excess As concentration needed to nucleate a new WZ layer. However, the imaging conditions used to observe the moving step do not have enough spatial resolution to allow for such accurate measurements.

Interestingly, when growing WZ-ZB heterostructures, it is possible that the first WZ nucleus on ZB already results in a slow moving step, showing that is more energetically favorable to keep the WZ step than to dissolve a truncated facet. Using only dark field imaging, we cannot determine if it is the first WZ layer that results in slow step-flow, or if a few bilayers are required. However, based on the regular timing of nucleation event, it is highly likely that the very first WZ nucleus results in slow step-flow. On the other hand, ZB growing on WZ shows a truncated facet after the first ZB nucleation,

indicating that completing the top facet by removing material at the truncated facet gives a lower total energy. This behavior could be explained by the difference in cohesive energy between WZ and ZB, which makes the adatom binding energy at a WZ step site lower than for the corresponding ZB.

A model to describe the differences of WZ and ZB growth based on the droplet geometry is being developed based on the observed differences in completion of a new bilayer on the top facet.

4.3 Memory effects

To grow heterostructures in particle-seeded nanowires, either where the crystal structure is abruptly changed or with different materials, the input gases to the growth chamber have to be changed. A change in the input gases, which may take only milliseconds, depending on the mass flow controllers, will eventually be reflected at the growing interface between the nanowire and its seed particle. However, the change at the growth interface is in many cases not as abrupt as the change in the input gases. Two effects that can smear out a rapid change in the input gases are the *reactor memory effect* and the *seed particle reservoir effect*.

4.3.1 Reactor memory effect

The *reactor memory effect* causes a carry-over of adatoms after a change in the precursor gases, either in the form of adatoms still diffusing on the surface, or from decomposition of the substrate [103]. Desorbing species then give a slowly decaying background for a relatively long time after the gas switch. For As and P, which have a high vapor pressure and are hence are quickly desorbed, the effect is considered minor. The high vapor pressure and low solubility of As and P in Au seed particles ensure that very abrupt heterointerfaces can be grown using both MOVPE [104] and chemical beam epitaxy (CBE) [105]. Elements with lower vapor pressures, such as Sb, will remain in the reactor chamber for much longer. One strategy to reduce the carry-over with low vapor pressure elements is to introduce a pause in the growth to allow for desorption of as much as possible of the low vapor pressure species before continuing [106].

Even for high vapor pressure As, reactor memory effects influence the sharpness of polytypic heterostructures, as is discussed in Paper II. In Paper I, we create defect-free WZ-to-ZB transitions in GaAs nanowires by abruptly increasing the AsH$_3$ flow. However, switching the structure back to WZ by simply reducing the AsH$_3$ flow to the value used for the previous WZ segment typically resulted in the new WZ segment having a very high density of stacking defects, as shown in Figure 4.11 a-d.
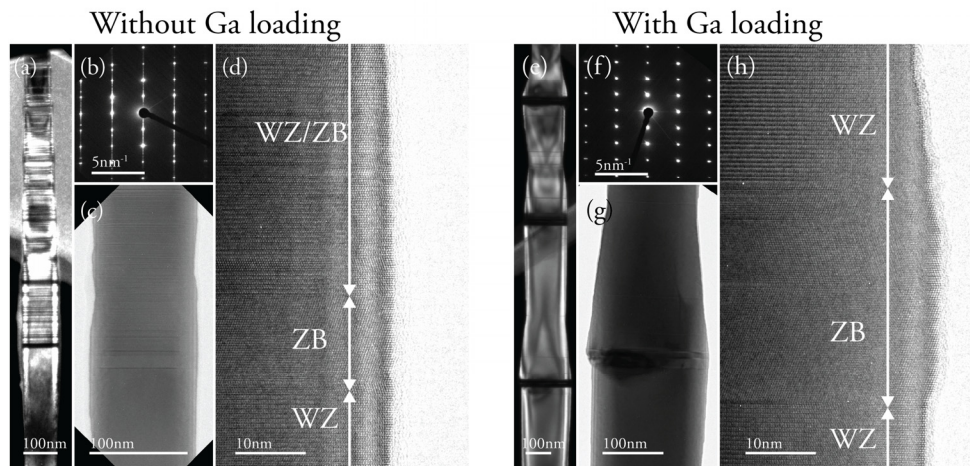
Figure 4.11. GaAs WZ NW with ZB insets grown without a TMGa pulse after each ZB segment imaged in the $\langle\bar{1}01\rangle/\langle\bar{1}\bar{1}2.0\rangle$ zone. The dark field image in (a) was obtained using the $[000.\bar{1}]$ diffraction spot, which only arises from WZ. (b) Selective area electron diffraction pattern from the WZ after the ZB segment.(c) (d) High resolution TEM images of the first ZB inset. (e-h) similar as for (a-d), with a 30s TMGa supply after each ZB inset before AsH₃ was turned on.

For ZB, As-rich conditions are used, which results in a lower Ga content in the seed particle, and possibly As-terminated surfaces as well. Reducing the AsH₃ flow will cause an increase in Ga diffusion to the seed particle and a change from As rich to potentially Ga rich surfaces. However, such a transition is likely to be much slower than the change in input precursor gas pressure. To force the system away from As rich conditions, the AsH₃ could instead be turned off for a short time, with only TMGa kept flowing. In Figure 4.11 e-h, a WZ GaAs nanowire with multiple ZB insets is shown, where only TMGa was supplied for 30 s after each ZB segment. It is clear that the ZB-to-WZ interface is improved compared to Figure 4.11 a-d.

Potentially, the reactor memory effect could be dependent on the reactor geometry. For the nanowires grown in this thesis, two horizontal flow reactors were used; an EPIQUIP VP502-RP and an AIXTRON 200/4. In both reactors, the input precursor gases pass a gradually hotter susceptor before reaching the samples. Arguably, some deposition may already take place on the susceptor before the sample, which creates an extra reservoir of material that could desorb later on, and follow the gas stream to the samples. Changing the reactor type to a close-coupled showerhead (CCS) reduces such effects, as the precursor gases are not exposed to a hot susceptor prior reaching the samples. With reduced reactor memory effects, better control of heterostructures is possible to achieve, which allowed for the highly precise crystal structure control in Paper xviii.

4.3.2 Seed particle reservoir effect

When using a foreign liquid seed particle to mediate the growth of nanowires, the adatoms alloy with the particle (for Au-seeded III-V nanowires this is typically true for one of the Group III elements). Even after turning off the precursor gas flow, the solute (Group III) could precipitate out from the solvent (Au). This causes, for example, the occurrence of "neck" regions when a GaAs nanowire is cooled down after growth in only AsH_3/H_2, as seen in Figure 4.4 above. The seed particle reservoir also causes graded interfaces in nanowire heterostructures where two dissimilar solutes are switched. For example, growing GaP on InP, In remaining inside the seed particle will precipitate out and incorporate during the growth of GaP, resulting in a graded interface and an In background in the GaP (Papers vii and viii). The interface for changing Group III in the other direction, InP on GaP, is much sharper. This can be explained by the different affinity of Au for the different Group III atoms. Au has a higher affinity for In than Ga, which results in a much lower solubility of Ga in Au-In than in pure Au. When switching from Ga to In as the solute in the Au particles, In swiftly replaces Ga, whereas in the other direction, the new solute is only slowly dissolved in the solvent particle, and to a much-reduced extent [107-109]. One method to increase interface sharpness when switching between a solute with high affinity to the seed particle to one with low affinity is to pulse the element with low affinity in order to reduce the solubility of the other solute without incorporating the pulsed element into the nanowire [110].

In Paper IV, we encountered the seed particle reservoir effect in a slightly different way to that discussed above. With decreasing AsH_3 pressure, we noted a slow increase in the seed particle volume, caused by its increasing Ga content. With an increase in AsH_3, the seed particle initially decreases in volume faster than the incorporation rate of Ga at the seed particle-nanowire interface. To explain the rapid decrease of Ga in the seed particle, diffusion from the seed particle has to be considered. With increasing AsH_3, radial growth of the nanowire increases, which lowers the Ga adatom concentration on the nanowire surfaces. As a result, the Ga chemical potential in the seed particle ends up higher than the Ga chemical potential on the nanowire side facets, and Ga diffuses out of the seed particle. On changing the AsH_3 pressure, the seed particle volume and composition also slowly change. In this case, because the seed particle size triggers the structural switch between WZ and ZB, a delay between the change in V/III ratio and the change in structure is observed.

4.4 Radial growth

During axial growth of a nanowire, some radial growth is inevitable. The final shape of a nanowire will be dependent on how the radial growth proceeds, and even in nanowires with very little radial overgrowth the seed particle-nanowire interface differs from the nanowire cross-section further down the nanowire [111]. Without control of radial growth, there could be detrimental effects on axial nanowire devices, as the upper segments of the nanowire could be short circuited to lower segments or to the substrate, even when the upper segment is supposed to be insulated from these segments. To suppress radial overgrowth, a low growth temperature [88, 112, 113], high supersaturation [85] or *in situ* etching [114-117] (Paper vii) could be used. If the radial growth is made in a controlled fashion, radial heterostructures result, and it becomes possible to make core-shell or core-multishell nanowires with tunable properties [118-123].

The growth of a shell around a nanowire is to a very large extent similar to the growth of epitaxial thin films. In highly lattice-mismatched systems, the Stranski-Krastanov type of quantum dot can be grown on the nanowire side facets [124, 125], and the lattice mismatch between the nanowire and the quantum dot may induce stacking faults in the dot [126]. The shell adopts the crystal structure of the core, and stacking faults in the core are transferred into the shell. On the other hand, stacking faults can acts as preferential nucleation sites for the shell, and position-controlled defects open a way to obtain position-controlled quantum dots [127].

As stacking faults in the core nanowire influence the shell growth, tight control of the structure of the core is essential to achieve well-controlled shell growth. The shell growth dynamics in InAsP-InP and InAs-InP core-shell nanowires with different crystal structures have been analyzed, showing that shell growth occurs preferentially on ZB facets [128, 129].

In Papers I and II, the same higher radial growth rates on ZB compared to WZ as was seen in [128, 129] was found when analyzing radial growth on ZB insets in WZ nanowires. In some cases, twin defects occurred in the radial overgrowth on the ZB insets, as shown in Figure 4.12. The blister-like structures caused by the twin defects occurred in three directions, which are deduced to be of $\langle \overline{1}\overline{1}\overline{1} \rangle$-type. For the $\langle 111 \rangle$ directions, less overgrowth was observed, and there were no twin defects. The increased overgrowth on the ZB facets caused a diameter increase of the nanowires around ZB insets, resulting in a modulation of the diameter along the nanowire length. The increased growth on ZB is attributed to a higher nucleation rate (due to higher surface energy) and lower diffusion lengths on the ZB facets compared to the WZ.
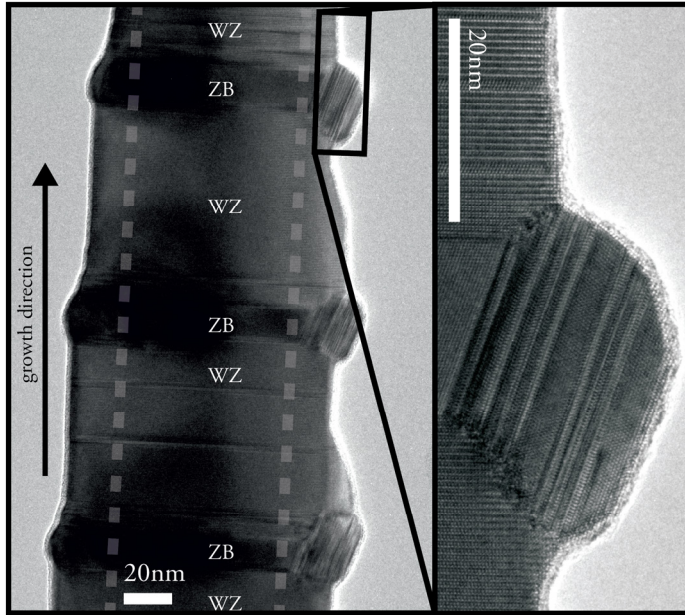
Figure 4.12. Bright field TEM images of a WZ GaAs nanowire with several ZB short segments. On the $\{\bar{1}\bar{1}\bar{1}\}$-type facets of the ZB segments, anisotropic overgrowth with twin defects results in blister-like features. Overgrowth also occurs on the WZ facets, as seen when comparing the nanowire diameter at the seed particle (as indicated with dashed grey lines) with the diameter further down the nanowire.

Lateral overgrowth on nanostructures has also been used to decrease interface-related defects in heteroepitaxy of thin films. In epitaxial lateral overgrowth (ELO), a mask is used which only allows growth in specific openings, from which the crystal later grows laterally to form a continuous film, see ref. [130] and references therein. In Paper VI, we used a similar approach to examine the possibility of growing a continuous film of WZ GaAs. Having a large WZ GaAs crystal with very few stacking defects would allow for optical and electrical measurements without interference from surface states, which otherwise are a nuisance in GaAs.

For the radial overgrowth in Paper VI, we started with pure GaAs WZ nanowires, using the growth parameters established in Paper I. To reduce axial growth during radial overgrowth, the Au seed particles were etched off prior to the second growth step (shell growth) using a commercial cyanide-based Au-etchant (Transene TFAC). A set of SEM images showing the shell growth with increasing growth time is shown in Figure 4.13, together with a graph of the measured nanowire length and diameter. For the shorter radial overgrowth times, it is mainly the pyramidal base which increases in size, until it develops $\{10\bar{1}.0\}$ facets. Once such facets are formed, we believe that nucleation occurs at step sites between the nanowire and the substrate. From there, the growth proceeds

in a Frank-van der Merwe mode with step flow along the $\{10\bar{1}.0\}$ facets in the $[000.\bar{1}]$ direction.

Using XRD and TEM, we investigated the crystal structure of the radially overgrown GaAs WZ nanowires. For radial growth times up to 60 min, we observed an increase in the XRD scattering intensity for WZ, whereas for longer growth times the intensity decreased with increasing growth time. For the longest growth time (240 min) the WZ scattering intensity was below that of a reference sample with only core WZ nanowires. By preparing thin lamellae for TEM investigation using FIB (Paper xvi), we observed a mixed WZ/ZB structure whenever two or more nanowires grew together radially, see Figure 4.14. For nanowires which were still free-standing, the crystal structure remained as pure WZ.

To explain the phase transformation, a similar mechanism to that proposed by Patriarche et al. was used [131]. In the work by Patriarche et al., highly defective GaAs nanowires were gradually buried, bilayer by bilayer, by a perfect ZB substrate growth. Each time a bilayer in the nanowire was out of registry with the burying ZB matrix, a dislocation propagated through the nanowire, shifting the faulty bilayer to the same position as the matrix. As the burying matrix completely surrounded the faulty bilayer,
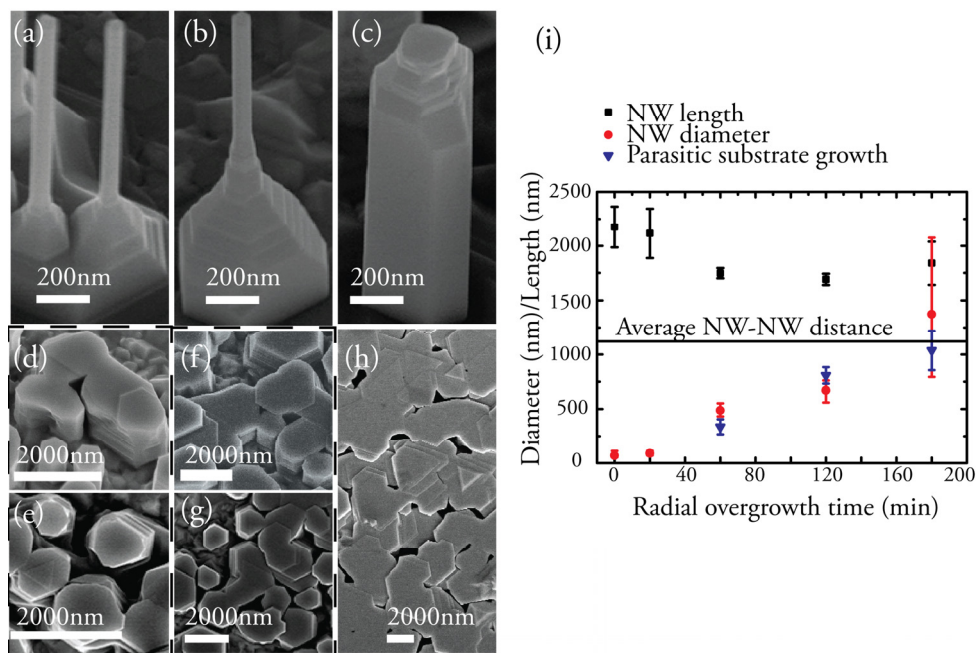
Figure 4.13. SEM images of WZ GaAs nanowires with different radial overgrowth times, (a) 5 minutes, (b) 20 minutes, (c) 60 minutes, (d,e) 120 minutes, (f,g) 180 minutes and (h) 240 minutes. (a-d) and (f) are recorded with 30° sample tilt. Measured nanowire diameter and length for increasing radial overgrowth time.
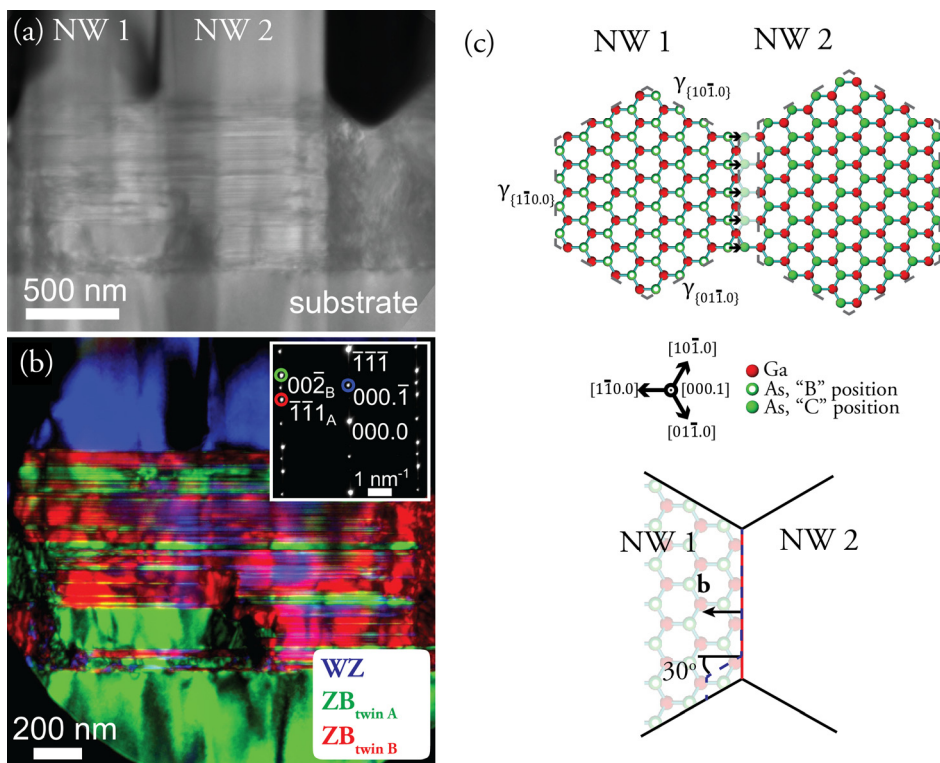
Figure 4.14. (a,b) TEM images of partly merged WZ GaAs nanowires. Using the diffraction spots indicated in the inset in (b) for DF imaging, the occurrence of WZ and the two ZB twin orientations are mapped and marked with different colors in (b). (c) shows diagrams of two miss-matched WZ nanowires viewed in the $[000.1]$ direction. The miss-match at the interface between the two nanowires gives rise to a dislocation with a Burgers vector as indicated, which may propagate.

propagation of the dislocation was thermodynamically favorable as the length of the dislocation thereby decreased. In our case, two WZ nanowires with different stacking, for example …ABABAB… and …CBCBCB… result in a similar defect at the interface between the nanowires once the radial overgrowth brings them into close enough proximity. In such a case, two scenarios are possible: either the mismatch is preserved at the nanowire-nanowire interface, or a dislocation is introduced in one of the nanowires, similar to the dislocation induced by the burying matrix in ref. [131].

Introducing a dislocation in the (000.1) plane with a Burgers vector, **b,** of $1/3\langle 10\bar{1}.0\rangle$, would change the bonds from hexagonal to cubic, which changes one bilayer to ZB. As ZB has a higher cohesive energy [86], this would give the structure a lower total energy. For nanowires, the free surfaces will then also change, with a change in surface energy. As WZ $\{10\bar{1}.0\}$ planes are assumed to have lower surface energy than ZB $\{11\bar{2}\}$, the total surface energy will increase if such a dislocation propagates

through the nanowire. In addition, the geometry of the nanowires would also require an increase in the length of the dislocation, which increases its total energy, as discussed in Chapter 2.1.3.

To make an estimate of which of the three components dominate the total change in free energy, consider moving one III-V pair from a WZ position to a ZB one closest to the nanowire surface. Such change will give an energy gain of 24 meV due to the higher cohesive energy of ZB, but changing the position of the atom will also change the surface structure. As a crude approximation, assume that surface energy calculations for unreconstructed, large $\{10\bar{1}.0\}$ and $\{11\bar{2}\}$ facets also are valid for very small facets, and can be linearly scaled. If so, changing from $\{10\bar{1}.0\}$ to $\{11\bar{2}\}$ facets increases the surface energy by 3.06 meV/nm^2 [75]. For the dislocation line energy, the shear modulus of GaAs ZB has to be used, as the shear modulus in WZ is unknown. Using Equation 2.8 with α=1, a dislocation line with a Burgers vector of $1/3 \langle 10\bar{1}.0 \rangle$ has an estimated line energy of 10.74 eV/nm. Changing one III-V pair at the nanowire surface would then result in energy change of:

$$\Delta E_{dis} = \frac{b}{cos(30)} * 10.74 \ eV = 2.85 \ eV$$

$$\Delta E_{coh} = -24 * 10^{-3} \ eV = -0.024 \ eV \tag{4.10}$$

$$\Delta E_{\gamma} = \frac{b}{cos(30)} * 0.65 * 3.06 * 10^{-3} \ eV = 0.00053 \ eV$$

Clearly, the change in dislocation line energy, ΔE_{dis}, is the dominant change, as it is about two orders of magnitude larger than the change in cohesive energy, ΔE_{coh}. The change in surface energy, ΔE_{γ}, is negligible. Assuming similar shear moduli for WZ and ZB, ΔE_{dis} will be similar for a propagation of the dislocation line through WZ and ZB. Allowing the dislocation to propagate fully through either nanowire decreases the total energy, as the interface defect between the nanowires is removed. As a result, using WZ GaAs as a growth template to form a continuous film by radial overgrowth and merging of nanowires does not give bulk WZ, but a highly defective film.

5 Properties of GaAs WZ, ZB and WZ-ZB heterostructures

Since it is possible to grow high quality WZ and defect-free ZB segments with controlled lengths within the same nanowire, direct comparisons between WZ and ZB can be made. In this chapter, some differences between WZ and ZB will be discussed. The examples highlighted here are by no means the only differences, and other studies have also been performed, such as scanning tunneling microscopy and spectroscopy to measure surface morphology and local densities of states (Paper ix), Raman spectroscopy during strain to reveal details of the bandstructure [132], and time-resolved PL to determine carrier lifetimes [21].

5.1 Morphology differences

III-V nanowires grown along $[\bar{1}\bar{1}\bar{1}]$ could have a variety of side facets, whose formation is governed by the growth conditions. Figure 5.1 shows diagrams of possible nanowire morphologies for WZ, ZB and ZB with twin defects. For WZ, either $\{11\bar{2}.0\}$ or $\{1\bar{1}0.0\}$ surfaces will result in a hexagonal prism geometry, as in Figure 5.1a and b. Both types of surfaces are non-polar, and the six facets should consequently be of equal width. The equivalent ZB surfaces, $\{1\bar{1}0\}$ and $\{11\bar{2}\}$ would also result in a hexagonal cross-section, shown in Figure 5.1a and b. As the $\{1\bar{1}0\}$ planes are also are non-polar, this type of facets should also be of equal width. However, the $\{11\bar{2}\}$ planes are polar, and are either Group III terminated ($\{\bar{1}\bar{1}2\}$A) or Group V terminated ($\{11\bar{2}\}$B). The polarity of the surfaces is reflected in anisotropic lateral overgrowth, where $\{\bar{1}\bar{1}2\}$A grows faster than $\{11\bar{2}\}$B in Group V rich growth conditions [133, 134]. As a result, the cross-section will adopt a truncated triangular shape, as in Figure 5.1c.

For ZB with a single twin defect, the defect rotates the facets 60° about the $[\bar{1}\bar{1}\bar{1}]$ growth axis. For a nanowire with $\{11\bar{2}\}$-type facets, the $\{\bar{1}\bar{1}2\}$A below the twin will be parallel with $\{11\bar{2}\}$B above the twin. With anisotropic lateral overgrowth, the nanowire cross-section will be a truncated triangle with different orientations above and below the twin. At the interface between the two twin directions, a new type of facets occurs to accommodate the change in cross-section, see Figure 5.1d. For a thin twinned

segment in an otherwise perfect ZB segment, the twins could create a groove between two $\{\bar{1}\bar{1}2\}$A facets, as depicted in Figure 5.1e [133].

For ZB with regular twin defects, the resulting nanowire morphology can be as shown in Figure 5.1f. Here, each twin segment is composed of an octahedral segment, each with three $\{111\}$A and three $\{\bar{1}\bar{1}\bar{1}\}$B facets [82, 135-137]. At every twin defect, the facets are rotated 60°, which gives the nanowire a zigzag morphology.
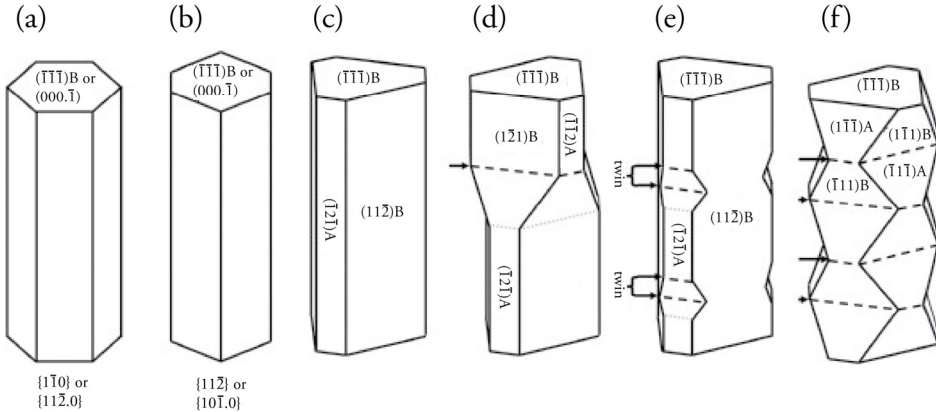
Figure 5.1. Schematic illustration of possible nanowire morphologies, from [138] with permission. For WZ, either $\{11\bar{2}.0\}$ or $\{1\bar{1}0.0\}$ surfaces will result in a hexagonal prism geometry (a,b). The equivalent ZB surfaces, $\{1\bar{1}0\}$ and $\{11\bar{2}\}$ may also result in a hexagonal cross-section (a,b), but the polar $\{11\bar{2}\}$ surface can also lead to a truncated triangular cross-section (c-e). (f) Regular twinning in ZB can result in a zigzag morphology with alternating $\{\bar{1}\bar{1}\bar{1}\}$B and $\{111\}$A facets.

Which facets form depends on the relative growth rates of the respective facets, which is also dependent on the relative surface energies of the facets. As nanowire growth takes place away from equilibrium conditions, the final shape of the nanowire does not necessarily fully reflect the equilibrium crystal shape under the growth conditions used. Taking kinetic effects into account, a qualitative comparison between different facets and their relative surface energy may still be carried out. Comparing facets formed for WZ and ZB at similar growth conditions can give an experimental measure of their relative surface energies.

In Paper I, GaAs WZ-ZB heterostructures were grown with a high crystal quality WZ bottom segment, a defect-free top ZB segment, and a defect-free interface between the two polytypes. To elucidate the terminating facets formed by the different polytypes in the nanowires, high resolution TEM and selective area diffraction patterns (SADP) together with STEM-HAADF were used. With HRTEM and SADP, the

crystallographic directions of the nanowire with respect to the image plane can be deduced. Using STEM-HAADF to obtain thickness profile of the nanowires, the orientation of the terminating facets with respect to the image plane can also be determined. Figure 5.2 displays STEM-HAADF, SEM images and a schematic illustration of the WZ-ZB heterostructure.
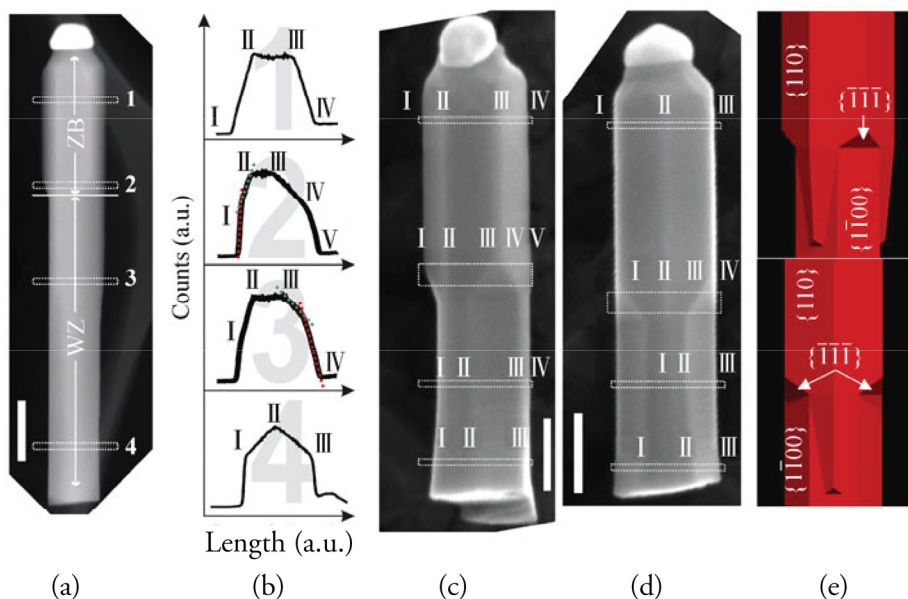
Figure 5.2. (a) STEM HAADF of WZ-ZB a heterostructure in the $\langle\bar{1}01\rangle/\langle\bar{1}\bar{1}2.0\rangle$ zone. (b) Intensity line profile from the four marked regions in (a). (c) and (d) shows SEM images of similar nanowires imaged in directions close to $\langle\bar{1}01\rangle/\langle\bar{1}\bar{1}2.0\rangle$ and $\langle11\bar{2}\rangle/\langle10\bar{1}.0\rangle$ zone axes. In (e), a schematic illustration of the facets close to the WZ-ZB interface is shown.

Both the WZ and the ZB sections have a hexagonal cross-section, but their facets are rotated 30° with respect to each another. The WZ part of the nanowire has side facets parallel to the electron beam if imaged in the $\langle\bar{1}\bar{1}2.0\rangle$ zone axis, as well as parallel to the growth axis, which means it is terminated with $\{1\bar{1}0.0\}$ surfaces. The top ZB part has side facets parallel to the growth axis and image plane if imaged in the $\langle\bar{1}01\rangle$ zone axis, which means it is terminated with $\{110\}$ surfaces. As the WZ and ZB facets are rotated with respect to each other, extra facets occur at the interface. The extra facets consist of three $\{\bar{1}\bar{1}\bar{1}\}$B facets on the ZB side of the interface, and overgrowth on three WZ $\{1\bar{1}0.0\}$ facets results in facets close to $\{\bar{1}\bar{1}2.0\}$. However, the overgrowth of the three WZ facet is not homogeneous, and its facets couldn't be determined unambiguously. The appearance of the overgrowth on the WZ is a result of the lack of stable ZB facets at the WZ-ZB interface, which increases the growth rate at this point.

The ZB section has a larger diameter than the WZ, caused by faster lateral overgrowth on ZB than WZ. From the analysis of the faceting, it is concluded that WZ {1$\bar{1}$0.0} surfaces have the lowest growth rate in the growth conditions used, and hence are most likely to be the lowest energy surfaces. For ZB, {110} and {$\bar{1}\bar{1}\bar{1}$}B are the facets with lowest growth rate, but these still grow faster than WZ {1$\bar{1}$0.0}.

5.2 Lattice structure

Converting a cubic close-packed structure to a hexagonal close-packed structure, layers in the ⟨111⟩/⟨000.1⟩ direction are shifted from the cubic to the hexagonal close-packed arrangement. For ideal structures, the distance between the close-packed planes would be the same, and it is possible to derive the lattice constants of WZ from geometrical conversion of the ZB lattice constants. The WZ lattice constants would then be calculated from the ZB, using following relationship:

$$c_{geom,WZ} = \frac{2a_{ZB}}{\sqrt{3}}$$

$$a_{geom,WZ} = \frac{a_{ZB}}{\sqrt{2}}$$

(5.1)

However, using only geometrically converted lattice constants does not take into account distortions from the symmetric tetrahedral coordination which are typically found in hexagonal structures [139-145]. The deviation from an ideal tetrahedron comes from interactions with third next nearest atomic neighbors, as in the diagram in Figure 5.3. Depending on the ionicity of the III-V bonds, the interaction could be either repulsive or attractive, which results in either ZB being stable (repulsive) or WZ (attractive) [86, 145].

For GaAs, the repulsive forces between hexagonal bilayers causes an elongation along the c-axis (the [000.1] direction) of the WZ crystal, which has been observed using XRD [146] and electron diffraction [147] in nanowires, as well as in WZ GaAs powder obtained at high pressure [148]. However, in these reports, the WZ consists of shorter segments sandwiched between ZB, and the lattice parameters are likely to be influenced by the polytype mixing. In addition to the elongation along the c-axis, the in-plane spacing perpendicular to the c-axis, a, is smaller, which further increases the deviation from an ideal tetrahedron. Measuring lattice parameters from such mixed structures could easily give deviations from the lattice parameters of a fully relaxed structure.
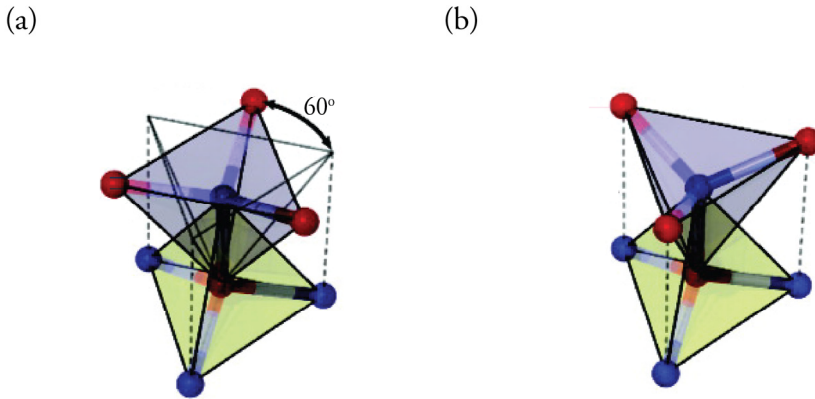
Figure 5.3. Diagram of the different stacking/bond configuration for a cubic (a) and a hexagonal (b) bilayer. In the hexagonal stacking, the third next nearest neighbor is located directly below in the [$000.\bar{1}$] direction. Adopted from [141], with permission.

If we define the hexagonality of a crystal as the ratio of the number of bilayers with hexagonal stacking to the total number of bilayers, ZB has a hexagonality of 0%, whereas WZ has 100%. For higher order polytypes, the hexagonality would be in between, depending on the fraction of hexagonal bilayers. For 4H, a polytype sometimes found in short segments in nanowires [149, 150], the hexagonality is 50% (alternate stacked bilayers are hexagonal). As the repulsive forces along the c-axis result from hexagonal stacked bilayers, 4H should have a c/a deviation of half that of WZ. To test such hypothesis experimentally, a large enough, relaxed 4H crystal is needed for measurement of the lattice parameters. In addition, the repulsive forces will also influence the cohesive energy of the crystal, and the cohesive energy of 4H should be in between WZ and ZB.

In Paper VI, accurate XRD measurements on the lattice parameters of both WZ and 4H were carried out. With superior WZ crystal quality with very few stacking faults, the WZ crystal in these measurements is believed to be unstrained and not influenced by any ZB inclusions. The 4H occurred due to a nanowire-nanowire interaction as nanowires radially merged with large lateral overgrowth, and were not grown to a controlled length. Still, both XRD measurements and TEM results suggest an average 4H segment length of a few hundred nanometers, which should be enough to measure the lattice parameters accurately. The measured lattice parameters with their deviation from the geometrically converted ZB values are given in Table 5.1.

For an ideal tetrahedron, the c/a ratio is 1.6333, but as the c-axis lattice plane distance increases and the in-plane lattice parameter decreases for hexagonal structures with repulsive interactions between bilayers, the c/a ratio increases. For the GaAs WZ in Paper VI, the c/a ratio increases to 1.649, which is 0.98% higher than the ideal

structure. The value found is in good agreement with theoretical values of 1.646-1.651 [86, 151, 152]. For 4H, the c/a ratio was found to be 3.282, which is 0.49% higher than ideal. Comparing the deviations in c/a from an ideal tetrahedron for WZ and 4H, it is found that the deviation in 4H is only half that of WZ, which is in line with the discussion above regarding the hexagonality of the structures.

Table 5.1. Experimental measured lattice parameters of GaAs WZ and 4H from Paper VI, together with the deviation from the geometrically converted GaAs ZB lattice parameters.

	a [Å]	Δa/a [%]	c [Å]	Δc/c [%]
WZ	3.9845	-0.324	6.5701	0.647
4H	3.9900	-0.186	13.0964	0.313

With a break in symmetry from an ideal tetrahedron, a displacement of charges occurs within WZ and 4H unit cells. The displacement of charges leads to layers of alternating charge density along the $[000.1]$ direction, which gives rise to a spontaneous polarization of the crystal [153, 154]. The spontaneous polarization affects electronic and optical properties of the material, which is well known to occur in WZ III-nitride structures [153, 155]. In heterostructures, the polarization could create internal electric fields induced by charge accumulation at interfaces, which causes the so-called quantum-confined Stark effect [156, 157]. So far, the spontaneous polarization in GaAs has not gained much attention, but it has been observed experimentally [158].

5.3 Band alignment

Because of the different atomic arrangements in the ZB and WZ crystals, the band structure is also different. For GaAs, *ab initio* calculations have proposed a rather wide range of band gaps for WZ, ranging from 1.38 eV to 1.81 eV [17, 86, 159, 160]. The range of experimental measurements of the WZ band gap is more narrow, spanning from 1.44 eV to 1.54 eV [21-24, 161], which is close to the ZB band gap of 1.52 eV. In Paper V, the measured band gap was also very similar for both WZ and ZB, very close to the values measured in ref. [23]. In Paper V, we were also able to show that the valence and conduction band alignment at a WZ-ZB interface is of type II, with a band offset of around 100 meV, in agreement with theoretical predictions [17, 160].

A type II band alignment, with WZ having higher energy bands, causes a spatial separation of charge carriers at the interface, with electrons confined in the ZB and holes in the WZ. When power-dependent photoluminescence measurements are performed on such an interface, the spatially separated charge carriers induce a strong power-dependent emission peak [153, 162]. In Figure 5.4, power-dependent PL spectra, recorded at a temperature of 4K from a single WZ-ZB nanowire are shown,

together with the position of the power-dependent emission peak with increasing excitation power.

The power dependency can be qualitatively explained as follows: for low excitation power, the conduction and valence bands are unaffected by the small increase in excited charge carriers, see Figure 5.5a, and the emission energy is given by the energy difference between the ZB conduction band and the WZ valence band. At higher excitation power, the increased density of excited carriers close to the interface between ZB and WZ causes band bending, which creates triangular potential wells with confined states at the interface, see Figure 5.5b. The increased density of charge carriers will cause state-filling in the wells, leading to a blue-shift in the emission energy (a Burstein-Moss shift). At even higher excitation power, both the triangular well in the ZB for electrons and the triangular well for holes in the WZ will be filled, and the emission energy will be similar to the band gap emission, as depicted in Figure 5.5c.

Following the reasoning above, the WZ-ZB valence band offset should be the difference between the ZB band gap and the lowest emission energy for the power-dependent emission peak. From Figure 5.4b, it can be seen that the emission energy starts at 1.42 eV, which gives a valence band offset of 100 meV, close to theoretical predictions [17, 160] and estimates from scanning tunneling spectroscopy (Paper ix). To estimate the conduction band offset as well, the only unknown variable is the band gap of WZ. Measuring photoluminescence on pure WZ nanowires, without a ZB top segment, we found the WZ band gap to be 1.52 eV, very similar to the band gap of ZB. Hence due to symmetry, the conduction band offset between WZ and ZB is also estimated to 100 meV.
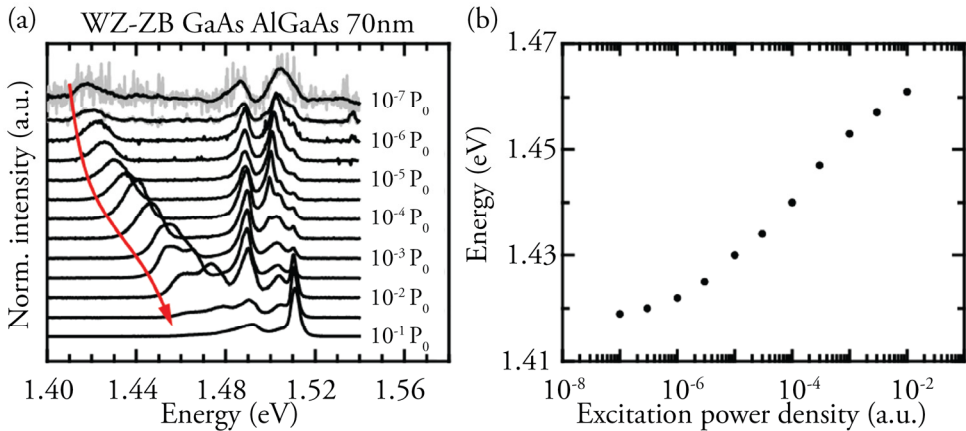
Figure 5.4. (a) Power-dependent PL measurements on GaAs WZ-ZB nanowires. The peak position of the power-dependent emission is plotted versus excitation power in (b).
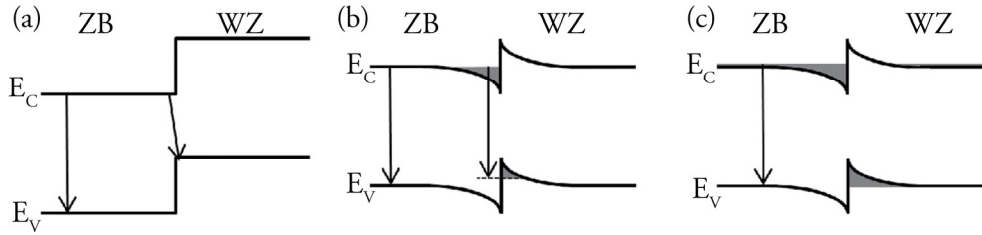
Figure 5.5. A diagram of the band alignment at the ZB-WZ interface in GaAs nanowires. Two types of transitions are marked: band-to-band within the ZB (the same type of transition also occurs in the WZ, with similar energy) and the spatially indirect band-to-band transition from the ZB conduction band to the WZ valence band. At low excitation power (a), the spatially indirect emission energy is directly dependent on the band offsets. At intermediate excitation power (b), state filling occurs in the electron potential well on the ZB side of the ZB-WZ interface. At high excitation power (c), state filling also occurs in the hole potential well at the WZ side of the interface.

Being able to grow GaAs nanowires with very precise control of the crystal structure has enabled studies on the intrinsic properties of the metastable WZ phase, as well as the interface between the different polytypes. The photoluminescence results presented here are some of our first results on WZ-ZB GaAs heterostructures. By increasing the complexity of the nanowires, further details of the electron and hole dynamics can be studied. For example, GaAs nanowires with short segments of WZ in a ZB matrix allow for hole confinement in the WZ and the effective mass of holes in the GaAs WZ valence band can be estimated (Paper xviii). The growth procedures developed during the work in this thesis, and the knowledge gained on nanowire growth dynamics, are now being used to fabricate designed polytypic GaAs nanowires for further luminescence studies.

6 Concluding remarks and outlook

Over the last two decades, our knowledge of why and how semiconductor nanowires grow has expanded tremendously. Today, a wide variety of devices have been demonstrated, in both axial and radial geometries. To push the possibilities further and design nanowires with the desired properties, the possibility of grow nanowires with crystal structures which are not stable in the bulk can be used. However, details of the formation and properties of metastable phases in III-V nanowires are still to be investigated.

This work has focused on the growth of polytypic GaAs nanowires, where development of MOVPE growth of pure GaAs WZ nanowires, WZ-ZB heterostructures, and WZ nanowires with multiple ZB insets was carried out. For typical MOVPE growth conditions, it was shown that ZB is grown in a As-rich environment, whereas WZ requires Ga-rich conditions. Using *in situ* TEM, the conditions for WZ growth were found to be more complex, where the balance between Ga and As at the seed particle determines its size, which in turn influences the growth rate of the nanowire. Further, it was shown that for very low V/III ratios, another transition to ZB is made. Combining the two growth regimes, it can be seen that WZ grows at an intermediate V/III ratio, where a higher V/III ratio causes a change to ZB because of the As-rich environment; and a lower V/III ratio causes a change to ZB because of a larger seed particle. Theoretically, both ZB regimes should be possible to reach in MOVPE, and experiments to verify this have been carried out and are being analyzed. Hopefully, these will show that results from polytypic growth of Au and Ga-seeded MBE-grown GaAs nanowires may be transferred to MOVPE.

By preparing high quality WZ and WZ-ZB heterostructures, some properties of the metastable WZ phase and the interface between WZ and ZB have been studied. As case studies, the unit cell dimensions of GaAs WZ and 4H were accurately determined using X-ray diffraction, as well as the band gap alignment between WZ and ZB using photoluminescence on single nanowires.

Further studies on electron and hole confinement in WZ-ZB-WZ and ZB-WZ-ZB structures are presently being performed to determine the effective masses of electrons and holes in WZ GaAs. Pushing the crystal structure tuning to create one and only one twin plane in ZB GaAs, which also could be regarded as a single layer of WZ, it should be possible to create a 2D sheet of polarized excitons at high photon excitation densities.

Such sheets of polarized excitons should include the exotic Wigner supersolid, which so far has only been theoretically proposed [163, 164].

With most of the analyses of nanowire growth done *ex situ* after cooling down from the growth temperature, it is only possible to estimate the true state of the seed particle governing the growth, not to determine it unambiguously. Here, the use of *in situ* TEM investigations plays a crucial role in verifying (or falsifying) models explaining nanowire growth which are based on *ex situ* observations. This thesis presents the first *in situ* TEM observations of growing GaAs nanowires. Moreover, it presents the first *in situ* TEM study of controlled polytypic growth of nanowires, showing a striking difference between WZ and ZB in the dynamics at the seed particle-nanowire interface. However, limitations in resolution still leaves some questions to answer. In terms of temporal resolution, what comes first: a new ZB nucleus or truncation of a corner facet? With respect to spatial resolution, how large are the critical nuclei for WZ and ZB, and where do they actually form?

With a modern environmental TEM, an increased spatial and temporal resolution could be achieved, and if it is designed with a gas handling system capable of handling the dangerous hydrides and metal-organics used for MOVPE growth, even more details of the growth of semiconductor crystals could be determined. Combining such a microscope with analytical capabilities such as XEDS or electron energy loss spectroscopy (EELS) would give information about the composition of seed particles and nanowires during growth. Studies of how the composition of the seed particle influences the growth could then be performed, as well as detailed investigations of the formation of axial heterostructures in nanowires. Even if we today are able to fabricate complex nanowire structures, many questions regarding the details of the nanowires' growth remain to be explained. The more such details we know, the more precise control of nanowire growth becomes possible.

7 References

1. Gil, E., et al., *Record Pure Zincblende Phase in GaAs Nanowires down to 5 nm in Radius.* Nano Letters, 2014. **14**(7): p. 3938-3944.
2. Salfi, J., et al., *Electronic properties of quantum dot systems realized in semiconductor nanowires.* Semiconductor Science and Technology, 2010. **25**(2): p. 024007.
3. Samuelson, L., et al., *Semiconductor nanowires for 0D and 1D physics and applications.* Physica E: Low-dimensional Systems and Nanostructures, 2004. **25**(2–3): p. 313-318.
4. Li, Y., et al., *Nanowire electronic and optoelectronic devices.* Materials Today, 2006. **9**(10): p. 18-27.
5. Caroff, P., et al., *High-Quality InAs/InSb Nanowire Heterostructures Grown by Metal–Organic Vapor-Phase Epitaxy.* Small, 2008. **4**(7): p. 878-882.
6. Gudiksen, M.S., et al., *Growth of nanowire superlattice structures for nanoscale photonics and electronics.* Nature, 2002. **415**(6872): p. 617-620.
7. Svensson, C.P.T., et al., *Monolithic GaAs/InGaP nanowire light emitting diodes on silicon.* Nanotechnology, 2008. **19**(30): p. 305201.
8. Wallentin, J., et al., *InP Nanowire Array Solar Cells Achieving 13.8% Efficiency by Exceeding the Ray Optics Limit.* Science, 2013. **339**(6123): p. 1057-1060.
9. Soci, C., et al., *ZnO Nanowire UV Photodetectors with High Internal Gain.* Nano Letters, 2007. **7**(4): p. 1003-1009.
10. Ganjipour, B., et al., *High Current Density Esaki Tunnel Diodes Based on GaSb-InAsSb Heterostructure Nanowires.* Nano Letters, 2011. **11**(10): p. 4222-4226.
11. Dey, A.W., et al., *High-Performance InAs Nanowire MOSFETs.* Electron Device Letters, IEEE, 2012. **33**(6): p. 791-793.
12. Zheng, G., et al., *Multiplexed electrical detection of cancer markers with nanowire sensor arrays.* Nature Biotechnology, 2005. **23**(10): p. 1294-1301.
13. Caroff, P., Bolinsson, J., and Johansson, J., *Crystal Phases in III-V Nanowires: From Random Toward Engineered Polytypism.* Selected Topics in Quantum Electronics, IEEE Journal of, 2011. **17**(4): p. 829-846.
14. Thelander, C., et al., *Effects of Crystal Phase Mixing on the Electrical Properties of InAs Nanowires.* Nano Letters, 2011. **11**(6): p. 2424-2429.
15. Spirkoska, D., et al., *Structural and optical properties of high quality zinc-blende/wurtzite GaAs nanowire heterostructures.* Physical Review B, 2009. **80**(24): p. 245325.
16. Akopian, N., et al., *Crystal Phase Quantum Dots.* Nano Letters, 2010. **10**(4): p. 1198-1201.
17. De, A. and Pryor, C.E., *Predicted band structures of III-V semiconductors in the wurtzite phase.* Physical Review B, 2010. **81**(15): p. 155210.

18. Dick, K.A., et al., *Crystal Phase Engineering in Single InAs Nanowires.* Nano Letters, 2010. **10**(9): p. 3494-3499.

19. Joyce, H.J., et al., *Phase Perfection in Zinc Blende and Wurtzite III–V Nanowires Using Basic Growth Parameters.* Nano Letters, 2010. **10**(3): p. 908-915.

20. Dick, K.A., et al., *Parameter space mapping of InAs nanowire crystal structure.* Journal of Vacuum Science & Technology B, 2011. **29**(4): p. 04D103.

21. Ahtapodov, L., et al., *A Story Told by a Single Nanowire: Optical Properties of Wurtzite GaAs.* Nano Letters, 2012. **12**(12): p. 6090-6095.

22. Hoang, T.B., et al., *Observation of free exciton photoluminescence emission from single wurtzite GaAs nanowires.* Applied Physics Letters, 2009. **94**(13): p. 133105.

23. Ketterer, B., et al., *Untangling the Electronic Band Structure of Wurtzite GaAs Nanowires by Resonant Raman Spectroscopy.* ACS Nano, 2011. **5**(9): p. 7585-7592.

24. Heiss, M., et al., *Direct correlation of crystal structure and optical properties in wurtzite/zinc-blende GaAs nanowire heterostructures.* Physical Review B, 2011. **83**(4): p. 045303.

25. Munshi, A.M., et al., *Crystal phase engineering in self-catalyzed GaAs and GaAs/GaAsSb nanowires grown on Si(111).* Journal of Crystal Growth, 2013. **372**(0): p. 163-169.

26. Dheeraj, D.L., et al., *Controlling crystal phases in GaAs nanowires grown by Au-assisted molecular beam epitaxy.* Nanotechnology, 2013. **24**(1): p. 015601.

27. Soda, M., et al., *Transition from Au to pseudo-Ga catalyzed growth mode observed in GaAs nanowires grown by molecular beam epitaxy.* Physical Review B, 2012. **85**(24): p. 245450.

28. Glas, F., Harmand, J.-C., and Patriarche, G., *Why Does Wurtzite Form in Nanowires of III-V Zinc Blende Semiconductors?* Physical Review Letters, 2007. **99**(14): p. 146101.

29. Oh, S.H., et al., *Oscillatory Mass Transport in Vapor-Liquid-Solid Growth of Sapphire Nanowires.* Science, 2010. **330**(6003): p. 489-493.

30. Gamalski, A.D., Ducati, C., and Hofmann, S., *Cyclic Supersaturation and Triple Phase Boundary Dynamics in Germanium Nanowire Growth.* The Journal of Physical Chemistry C, 2011. **115**(11): p. 4413-4417.

31. Wen, C.Y., et al., *Periodically Changing Morphology of the Growth Interface in Si, Ge, and GaP Nanowires.* Physical Review Letters, 2011. **107**(2).

32. Smart, L. and Moore, E., *Solid state chemistry : an introduction.* 3rd ed. 2005, CRC Press: Boca Raton. 407 p.

33. Williams, D. and Carter, C.B., *Transmission Electron Microscope.* 1996, Springer US.

34. Dubrovskii, V.G. and Sibirev, N.V., *Growth thermodynamics of nanowires and its application to polytypism of zinc blende III-V nanowires.* Physical Review B, 2008. **77**(3): p. 035414.

35. Moll, N., et al., *GaAs equilibrium crystal shape from first principles.* Physical Review B, 1996. **54**(12): p. 8844-8855.

36. Smith, D.L., *Thin-film deposition : principles and practice.* 1995, McGraw-Hill: New York. xxiii, 616 p.

37. DeHoff, R.T., *Thermodynamics in materials science.* 2nd ed. 2006, CRC/Taylor & Francis: Boca Raton. 605 p.

38. Hull, D. and Bacon, D.J., *Introduction to dislocations.* 5th ed. 2011, Butterworth-Heinemann.

39.   Hirth, J.P. and Lothe, J., *Theory of dislocations*. McGraw-Hill series in materials science and engineering. 1967, McGraw-Hill: New York,. xi, 780 p.

40.   Jindal, V. and Shahedipour-Sandvik, F., *Density functional theoretical study of surface structure and adatom kinetics for wurtzite AlN.* Journal of Applied Physics, 2009. **105**(8): p. 084902-084902-6.

41.   Stringfellow, G.B., *4 - Source Molecules*, in *Organometallic Vapor-Phase Epitaxy (Second Edition)*, G.B. Stringfellow, Editor. 1999, Academic Press: San Diego. p. 151-209.

42.   Stringfellow, G.B., *5 - Kinetics*, in *Organometallic Vapor-Phase Epitaxy (Second Edition)*, G.B. Stringfellow, Editor. 1999, Academic Press: San Diego. p. 211-295.

43.   Larsen, C.A., et al., *Decomposition Mechanisms of Trimethylgallium.* Journal of Crystal Growth, 1990. **102**(1-2): p. 103-116.

44.   Yu, M.L., Memmert, U., and Kuech, T.F., *Reaction of trimethylgallium in the atomic layer epitaxy of GaAs (100).* Applied Physics Letters, 1989. **55**(10): p. 1011-1013.

45.   Larsen, C.A., Buchan, N.I., and Stringfellow, G.B., *Reaction-Mechanisms in the Organometallic Vapor-Phase Epitaxial-Growth of Gaas.* Applied Physics Letters, 1988. **52**(6): p. 480-482.

46.   Tamaru, K., *The Decomposition of Arsine.* Journal of Physical Chemistry, 1955. **59**(8): p. 777-780.

47.   Larsen, C.A., et al., *Kinetics of the Reaction between Trimethylgallium and Arsine.* Journal of Crystal Growth, 1990. **102**(1-2): p. 126-136.

48.   Bowen, D.K. and Tanner, B.K., *X-ray metrology in semiconductor manufacturing*. 2006, CRC/Taylor & Francis: Boca Raton. 279 p.

49.   Bragg, W.H. and Bragg, W.L., *The reflection of X-rays by crystals.* Proceedings of the Royal Society of London Series a-Containing Papers of a Mathematical and Physical Character, 1913. **88**(604): p. 428-428.

50.   Borg, B.M., et al., *Enhanced Sb incorporation in InAsSb nanowires grown by metalorganic vapor phase epitaxy.* Applied Physics Letters, 2011. **98**(11).

51.   Hawkes, P.W. and Kasper, E., *41 - Aberration Correction*, in *Principles of Electron Optics*, P.W.H. Kasper, Editor. 1996, Academic Press: San Diego. p. 857-878.

52.   Hawkes, P.W., *Aberration correction past and present.* Vol. 367. 2009. 3637-3664.

53.   Haider, M., et al., *Electron microscopy image enhanced.* Nature, 1998. **392**(6678): p. 768-769.

54.   Marton, L., *Electron microscopy of biological objects.* Nature, 1934. **133**: p. 911-911.

55.   Xin, H.L., et al., *In Situ TEM Study of Catalytic Nanoparticle Reactions in Atmospheric Pressure Gas Environment.* Microscopy and Microanalysis, 2013. **19**(06): p. 1558-1568.

56.   Lenrick, F., et al., *Straight and kinked InAs nanowire growth observed in situ by transmission electron microscopy.* Nano Research, 2014. **7**(8): p. 1188-1194.

57.   Schneider, N.M., et al., *Electron–Water Interactions and Implications for Liquid Cell Electron Microscopy.* The Journal of Physical Chemistry C, 2014. **118**(38): p. 22373-22382.

58.   Hammar, M., et al., *In situ ultrahigh vacuum transmission electron microscopy studies of hetero-epitaxial growth I. Si(001)Ge.* Surface Science, 1996. **349**(2): p. 129-144.

59.   Frances, M.R., *Controlling nanowire structures through real time growth studies.* Reports on Progress in Physics, 2010. **73**(11): p. 114501.

60.   Burstein, E., *Anomalous Optical Absorption Limit in InSb.* Physical Review, 1954. **93**(3): p. 632-633.

61.   Moss, T.S., *The Interpretation of the Properties of Indium Antimonide.* Proceedings of the Physical Society. Section B, 1954. **67**(10): p. 775.

62.   Treuting, R.G. and Arnold, S.M., *Orientation habits of metal whiskers.* Acta Metallurgica, 1957. **5**(10): p. 598.

63.   Compton, K.G., Mendizza, A., and Arnold, S.M., *Filamentary Growths On Metal Surfaces – "Whiskers".* Corrosion, 1951. **7**(10): p. 327-334.

64.   Wagner, R.S. and Ellis, W.C., *VAPOR-LIQUID-SOLID MECHANISM OF SINGLE CRYSTAL GROWTH.* Applied Physics Letters, 1964. **4**(5): p. 89-90.

65.   Barns, R.L. and Ellis, W.C., *Whisker Crystals of Gallium Arsenide and Gallium Phosphide Grown by the Vapor—Liquid—Solid Mechanism.* Journal of Applied Physics, 1965. **36**(7): p. 2296-2301.

66.   Dick, K.A., *A review of nanowire growth promoted by alloys and non-alloying elements with emphasis on Au-assisted III–V nanowires.* Progress in Crystal Growth and Characterization of Materials, 2008. **54**(3–4): p. 138-173.

67.   Regolin, I., et al., *GaAs whiskers grown by metal-organic vapor-phase epitaxy using Fe nanoparticles.* Journal of Applied Physics, 2007. **101**(5): p. 054318.

68.   Hillerich, K., et al., *Epitaxial InP nanowire growth from Cu seed particles.* Journal of Crystal Growth, 2011. **315**(1): p. 134-137.

69.   Xu, H., et al., *Defect-Free <110> Zinc-Blende Structured InAs Nanowires Catalyzed by Palladium.* Nano Letters, 2012. **12**(11): p. 5744-5749.

70.   Novotny, C.J. and Yu, P.K.L., *Vertically aligned, catalyst-free InP nanowires grown by metalorganic chemical vapor deposition.* Applied Physics Letters, 2005. **87**(20): p. 203111.

71.   Premila, M., et al., *Mechanism of self-assembled growth of ordered GaAs nanowire arrays by metalorganic vapor phase epitaxy on GaAs vicinal substrates.* Nanotechnology, 2012. **23**(2): p. 025601.

72.   Motohisa, J., et al., *Growth of GaAs/AlGaAs hexagonal pillars on GaAs (111)B surfaces by selective-area MOVPE.* Physica E: Low-dimensional Systems and Nanostructures, 2004. **23**(3–4): p. 298-304.

73.   Wacaser, B.A., et al., *Preferential Interface Nucleation: An Expansion of the VLS Growth Mechanism for Nanowires.* Advanced Materials, 2009. **21**(2): p. 153-165.

74.   Richard, P.S., *Nucleation: theory and applications to protein solutions and colloidal suspensions.* Journal of Physics: Condensed Matter, 2007. **19**(3): p. 033101.

75.   Sibirev, N.V., et al., *Surface energy and crystal structure of nanowhiskers of III–V semiconductor compounds.* Physics of the Solid State, 2010. **52**(7): p. 1531-1538.

76.   Mills, K.C. and Su, Y.C., *Review of surface tension data for metallic elements and alloys: Part 1 – Pure metals.* International Materials Reviews, 2006. **51**(6): p. 329-351.

77.   de Gennes, P.G., *Wetting: statics and dynamics.* Reviews of Modern Physics, 1985. **57**(3): p. 827-863.

78.   Nebol'sin, V.A. and Shchetinin, A.A., *Role of Surface Energy in the Vapor–Liquid– Solid Growth of Silicon.* Inorganic Materials, 2003. **39**(9): p. 899-903.

79.   Dubrovskii, V.G., *Physical consequences of the equivalence of conditions for the steady-state growth of nanowires and the nucleation on triple phase line.* Technical Physics Letters, 2011. **37**(1): p. 53-57.

80.	Wallentin, J., et al., *Changes in Contact Angle of Seed Particle Correlated with Increased Zincblende Formation in Doped InP Nanowires.* Nano Letters, 2010. **10**(12): p. 4807-4812.

81.	Glas, F., *Chemical potentials for Au-assisted vapor-liquid-solid growth of III-V nanowires.* Journal of Applied Physics, 2010. **108**(7): p. 073506.

82.	Algra, R.E., et al., *Twinning superlattices in indium phosphide nanowires.* Nature, 2008. **456**(7220): p. 369-372.

83.	Wallentin, J., et al., *Probing the Wurtzite Conduction Band Structure Using State Filling in Highly Doped InP Nanowires.* Nano Letters, 2011. **11**(6): p. 2286-2290.

84.	Breuer, S., Feiner, L.-F., and Geelhaar, L., *Droplet Bulge Effect on the Formation of Nanowire Side Facets.* Crystal Growth & Design, 2013. **13**(7): p. 2749-2755.

85.	Joyce, H.J., et al., *Unexpected Benefits of Rapid Growth Rate for III–V Nanowires.* Nano Letters, 2008. **9**(2): p. 695-701.

86.	Yeh, C.Y., et al., *Zinc-Blende-Wurtzite Polytypism in Semiconductors.* Physical Review B, 1992. **46**(16): p. 10086-10097.

87.	Peter, K., et al., *Advances in the theory of III–V nanowire growth dynamics.* Journal of Physics D: Applied Physics, 2013. **46**(31): p. 313001.

88.	Joyce, H.J., et al., *Twin-Free Uniform Epitaxial GaAs Nanowires Grown by a Two-Temperature Process.* Nano Letters, 2007. **7**(4): p. 921-926.

89.	Shtrikman, H., et al., *Stacking-Faults-Free Zinc Blende GaAs Nanowires.* Nano Letters, 2008. **9**(1): p. 215-219.

90.	Dubrovskii, V.G., et al., *Role of nonlinear effects in nanowire growth and crystal phase.* Physical Review B, 2009. **80**(20): p. 205305.

91.	Krogstrup, P., et al., *In-situ x-ray characterization of wurtzite formation in GaAs nanowires.* Applied Physics Letters, 2012. **100**(9): p. 093103.

92.	Dubrovskii, V.G., *Influence of the group V element on the chemical potential and crystal structure of Au-catalyzed III-V nanowires.* Applied Physics Letters, 2014. **104**(5): p. 053110.

93.	Chou, Y.-C., et al., *Atomic-Scale Variability and Control of III-V Nanowire Growth Kinetics.* Science, 2014. **343**(6168): p. 281-284.

94.	Liu, J., et al., *Thermodynamic assessment of the Au–Ga system.* Journal of Alloys and Compounds, 2010. **508**(1): p. 62-70.

95.	Glas, F., Harmand, J.-C., and Patriarche, G., *Nucleation Antibunching in Catalyst-Assisted Nanowire Growth.* Physical Review Letters, 2010. **104**(13): p. 135501.

96.	Dubrovskii, V.G., *Self-regulated pulsed nucleation in catalyzed nanowire growth.* Physical Review B, 2013. **87**(19): p. 195426.

97.	Dubrovskii, V.G., et al., *Growth kinetics and crystal structure of semiconductor nanowires.* Physical Review B, 2008. **78**(23): p. 235301.

98.	Johansson, J., et al., *Effects of Supersaturation on the Crystal Structure of Gold Seeded III–V Nanowires.* Crystal Growth & Design, 2008. **9**(2): p. 766-773.

99.	Wen, C.Y., et al., *Step-Flow Kinetics in Nanowire Growth.* Physical Review Letters, 2010. **105**(19): p. 195502.

100.	Carter, W.C., et al., *Shape evolution by surface diffusion and surface attachment limited kinetics on completely faceted surfaces.* Acta Metallurgica et Materialia, 1995. **43**(12): p. 4309-4323.

101.	Hofmann, S., et al., *Ledge-flow-controlled catalyst interface dynamics during Si nanowire growth.* Nature Materials, 2008. **7**(5): p. 372-375.

102. Wen, C.Y., et al., *Structure, Growth Kinetics, and Ledge Flow during Vapor-Solid-Solid Growth of Copper-Catalyzed Silicon Nanowires.* Nano Letters, 2010. **10**(2): p. 514-519.

103. Sudo, S., et al., *In-situ As-P exchange monitoring in metal-organic vapor phase epitaxy of InGaAs/InP heterostructure by spectroscopic and kinetic ellipsometry.* Thin Solid Films, 1998. **313**: p. 604-608.

104. Borgström, M.T., et al., *Interface study on heterostructured GaP–GaAs nanowires.* Nanotechnology, 2006. **17**(16): p. 4010.

105. Bjork, M.T., et al., *Nanowire resonant tunneling diodes.* Applied Physics Letters, 2002. **81**(23): p. 4458-4460.

106. Ek, M., et al., *Formation of the Axial Heterojunction in GaSb/InAs(Sb) Nanowires with High Crystal Quality.* Crystal Growth & Design, 2011. **11**(10): p. 4588-4593.

107. Paladugu, M., et al., *Nature of heterointerfaces in GaAs/InAs and InAs/GaAs axial nanowire heterostructures.* Applied Physics Letters, 2008. **93**(10): p. 101911-101911-3.

108. Krogstrup, P., et al., *Junctions in Axial III–V Heterostructure Nanowires Obtained via an Interchange of Group III Elements.* Nano Letters, 2009. **9**(11): p. 3689-3693.

109. Ghalamestani, S.G., Ek, M., and Dick, K.A., *Realization of single and double axial InSb–GaSb heterostructure nanowires.* physica status solidi (RRL) – Rapid Research Letters, 2014. **8**(3): p. 269-273.

110. Dick, K.A., et al., *Controlling the Abruptness of Axial Heterojunctions in III–V Nanowires: Beyond the Reservoir Effect.* Nano Letters, 2012. **12**(6): p. 3200-3206.

111. Jiang, N., et al., *Understanding the True Shape of Au-Catalyzed GaAs Nanowires.* Nano Letters, 2014. **14**(10): p. 5865-5872.

112. Borgstrom, M.T., et al., *Size- and shape-controlled GaAs nano-whiskers grown by MOVPE: a growth study.* Journal of Crystal Growth, 2004. **260**(1-2): p. 18-22.

113. Verheijen, M.A., et al., *Growth Kinetics of Heterostructured GaP–GaAs Nanowires.* Journal of the American Chemical Society, 2006. **128**(4): p. 1353-1359.

114. Borgström, M.T., et al., *In situ etching for total control over axial and radial nanowire growth.* Nano Research, 2010. **3**(4): p. 264-270.

115. Assali, S., et al., *Direct Band Gap Wurtzite Gallium Phosphide Nanowires.* Nano Letters, 2013. **13**(4): p. 1559-1563.

116. Berg, A., et al., *Growth and characterization of wurtzite GaP nanowires with control over axial and radial growth by use of HCl in-situ etching.* Journal of Crystal Growth, 2014. **386**: p. 47-51.

117. Berg, A., et al., *In situ etching for control over axial and radial III-V nanowire growth rates using HBr.* Nanotechnology, 2014. **25**(50): p. 505601.

118. Lauhon, L.J., et al., *Epitaxial core-shell and core-multishell nanowire heterostructures.* Nature, 2002. **420**(6911): p. 57-61.

119. Qian, F., et al., *Core/multishell nanowire heterostructures as multicolor, high-efficiency light-emitting diodes.* Nano Letters, 2005. **5**(11): p. 2287-2291.

120. Xiang, J., et al., *Ge/Si nanowire heterostructures as high-performance field-effect transistors.* Nature, 2006. **441**(7092): p. 489-493.

121. Dey, A.W., et al., *Combining Axial and Radial Nanowire Heterostructures: Radial Esaki Diodes and Tunnel Field-Effect Transistors.* Nano Letters, 2013. **13**(12): p. 5919-5924.

122. Krogstrup, P., et al., *Single-nanowire solar cells beyond the Shockley-Queisser limit.* Nature Photonics, 2013. **7**(4): p. 306-310.

123. Mariani, G., et al., *Direct-Bandgap Epitaxial Core–Multishell Nanopillar Photovoltaics Featuring Subwavelength Optical Concentrators.* Nano Letters, 2013. **13**(4): p. 1632-1637.

124. Pan, L., et al., *Stranski–Krastanow Growth of Germanium on Silicon Nanowires.* Nano Letters, 2005. **5**(6): p. 1081-1085.

125. Yan, X., et al., *Realization of Stranski-Krastanow InAs quantum dots on nanowire-based InGaAs nanoshells.* Journal of Materials Chemistry C, 2013. **1**(47): p. 7914-7919.

126. Bi, Z., et al., *InN quantum dots on GaN nanowires grown by MOVPE.* physica status solidi (c), 2014. **11**(3-4): p. 421-424.

127. Kawaguchi, K., et al., *InAs quantum dots and quantum wells grown on stacking-fault controlled InP nanowires with wurtzite crystal structure.* Applied Physics Letters, 2011. **99**(13): p. 131915.

128. Wallentin, J., et al., *Growth of doped InAsyP1-y nanowires with InP shells.* Journal of Crystal Growth, 2011. **331**(1): p. 8-14.

129. Sepideh Gorji, G., et al., *Growth of InAs/InP core–shell nanowires with various pure crystal structures.* Nanotechnology, 2012. **23**(28): p. 285601.

130. Gibart, P., *Metal organic vapour phase epitaxy of GaN and lateral overgrowth.* Reports on Progress in Physics, 2004. **67**(5): p. 667-715.

131. Patriarche, G., et al., *Wurtzite to zinc blende phase transition in GaAs nanowires induced by epitaxial burying.* Nano Letters, 2008. **8**(6): p. 1638-1643.

132. Signorello, G., et al., *Inducing a direct-to-pseudodirect bandgap transition in wurtzite GaAs nanowires with uniaxial stress.* Nature Communications, 2014. **5**: p. 3655.

133. Zou, J., et al., *Growth Mechanism of Truncated Triangular III–V Nanowires.* Small, 2007. **3**(3): p. 389-393.

134. Verheijen, M.A., et al., *Three-Dimensional Morphology of GaP–GaAs Nanowires Revealed by Transmission Electron Microscopy Tomography.* Nano Letters, 2007. **7**(10): p. 3051-3055.

135. Johansson, J., et al., *Structural properties of [111]B -oriented III-V nanowires.* Nature Materials, 2006. **5**(7): p. 574-580.

136. Caroff, P., et al., *Controlled polytypic and twin-plane superlattices in III-V nanowires.* Nature Nanotechnology, 2009. **4**(1): p. 50-55.

137. Burgess, T., et al., *Twinning Superlattice Formation in GaAs Nanowires.* ACS Nano, 2013. **7**(9): p. 8105-8114.

138. Joyce, H.J., et al., *III–V semiconductor nanowires for optoelectronic device applications.* Progress in Quantum Electronics, 2011. **35**(2–3): p. 23-75.

139. Käckell, P., Wenzien, B., and Bechstedt, F., *Influence of atomic relaxations on the structural properties of SiC polytypes from ab initio calculations.* Physical Review B, 1994. **50**(23): p. 17037-17046.

140. Kriegner, D., et al., *Unit cell parameters of wurtzite InP nanowires determined by x-ray diffraction.* Nanotechnology, 2011. **22**(42).

141. Kriegner, D., et al., *Unit Cell Structure of Crystal Polytypes in InAs and InSb Nanowires.* Nano Letters, 2011. **11**(4): p. 1483-1489.

142. Kriegner, D., et al., *Unit cell structure of the wurtzite phase of GaP nanowires: X-ray diffraction studies and density functional theory calculations.* Physical Review B, 2013. **88**(11).

143.   Kiyoshi, T. and Toyosaka, M., *Growth of InAs Whiskers in Wurtzite Structure.* Japanese Journal of Applied Physics, 1966. **5**(8): p. 657.

144.   Mandl, B., et al., *Au-Free Epitaxial Growth of InAs Nanowires.* Nano Letters, 2006. **6**(8): p. 1817-1821.

145.   Lawaetz, P., *Stability of Wurtzite Structure.* Physical Review B, 1972. **5**(10): p. 4039.

146.   Mariager, S.O., et al., *Stages in molecular beam epitaxy growth of GaAs nanowires studied by x-ray diffraction.* Nanotechnology, 2010. **21**(11).

147.   Tchernycheva, M., et al., *Temperature conditions for GaAs nanowire formation by Au-assisted molecular beam epitaxy.* Nanotechnology, 2006. **17**(16): p. 4025-4030.

148.   McMahon, M.I. and Nelmes, R.J., *Observation of a wurtzite form of gallium arsenide.* Physical Review Letters, 2005. **95**(21).

149.   Dheeraj, D.L., et al., *Growth and Characterization of Wurtzite GaAs Nanowires with Defect-Free Zinc Blende GaAsSb Inserts.* Nano Letters, 2008. **8**(12): p. 4459-4463.

150.   Hillerich, K., et al., *Cu particle seeded InP InAs axial nanowire heterostructures.* Physica Status Solidi-Rapid Research Letters, 2013. **7**(10): p. 850-854.

151.   Panse, C., Kriegner, D., and Bechstedt, F., *Polytypism of GaAs, InP, InAs, and InSb: An ab initio study.* Physical Review B, 2011. **84**(7).

152.   Mujica, A., Needs, R.J., and Munoz, A., *First-Principles Pseudopotential Study of the Phase-Stability of the III-V Semiconductors GaAs and AlAs.* Physical Review B, 1995. **52**(12): p. 8881-8892.

153.   Belabbes, A., Furthmüller, J., and Bechstedt, F., *Relation between spontaneous polarization and crystal field from first principles.* Physical Review B, 2013. **87**(3): p. 035305.

154.   Bechstedt, F., Grossner, U., and Furthmüller, J., *Dynamics and polarization of group-III nitride lattices: A first-principles study.* Physical Review B, 2000. **62**(12): p. 8003-8011.

155.   Lähnemann, J., et al., *Direct experimental determination of the spontaneous polarization of GaN.* Physical Review B, 2012. **86**(8): p. 081302.

156.   Jain, S.C., et al., *III–nitrides: Growth, characterization, and properties.* Journal of Applied Physics, 2000. **87**(3): p. 965-1006.

157.   Miller, D.A.B., et al., *Band-Edge Electroabsorption in Quantum Well Structures: The Quantum-Confined Stark Effect.* Physical Review Letters, 1984. **53**(22): p. 2173-2176.

158.   Bauer, B., et al., *Direct detection of spontaneous polarization in wurtzite GaAs nanowires.* Applied Physics Letters, 2014. **104**(21): p. 211902.

159.   Zanolli, Z., et al., *Model GW band structure of InAs and GaAs in the wurtzite phase.* Physical Review B, 2007. **75**(24): p. 245121.

160.   Murayama, M. and Nakayama, T., *Chemical trend of band offsets at wurtzite/zinc-blende heterocrystalline semiconductor interfaces.* Physical Review B, 1994. **49**(7): p. 4710-4724.

161.   Kim, D.C., et al., *Polarization dependent photocurrent spectroscopy of single wurtzite GaAs/AlGaAs core-shell nanowires.* Applied Physics Letters, 2013. **102**(14): p. 142107.

162.   Hu, J., et al., *Type II photoluminescence and conduction band offsets of GaAsSb/InGaAs and GaAsSb/InP heterostructures grown by metalorganic vapor phase epitaxy.* Applied Physics Letters, 1998. **73**(19): p. 2799-2801.

163. Joglekar, Y.N., Balatsky, A.V., and Das Sarma, S., *Wigner supersolid of excitons in electron-hole bilayers.* Physical Review B, 2006. **74**(23): p. 233302.
164. Hartmann, P., Donkó, Z., and Kalman, G.J., *Structure and phase diagram of strongly-coupled bipolar charged-particle bilayers.* EPL (Europhysics Letters), 2005. **72**(3): p. 396.